Search for Neutrino-Induced Cascade Events in the IceCube Detector

D I S S E R T A T I O N

zur Erlangung des akademischen Grades

doctor rerum naturalium
(Dr. rer. nat.)
im Fach Physik

eingereicht an der
Mathematisch-Naturwissenschaftliche Fakultät I
Humboldt-Universität zu Berlin

von
Herrn Dipl.-Phys. Sebastian Panknin

Präsident der Humboldt-Universität zu Berlin:
Herr Prof. Dr. Jan-Hendrik Olbertz

Dekan der Mathematisch-Naturwissenschaftliche Fakultät I:
Herr Prof. Dr. Andreas Herrmann

Gutachter:
1. Herr Prof. Dr. Alexander Kappes
2. Herr Prof. Dr. Hermann Kolanoski
3. Herr Prof. Dr. Marek Kowalski

eingereicht am: 2011-07-18
Tag der mündlichen Prüfung: 2011-09-15

Wenn nicht mehr Zahlen und Figuren
Sind Schlüssel aller Kreaturen
Wenn die so singen, oder küssen,
Mehr als die Tiefgelehrten wissen,
Wenn sich die Welt ins freye Leben
Und in die Welt wird zurück begeben,
Wenn dann sich wieder Licht und Schatten
Zu ächter Klarheit wieder gatten,
Und man in Mährchen und Gedichten
Erkennt die wahren Weltgeschichten,
Dann fliegt vor Einem geheimen Wort
Das ganze verkehrte Wesen fort.

Novalis

Abstract

This thesis presents results of a search for a diffuse flux of high energetic neutrinos from extra-terrestrial origin. Such a flux is predicted by several models of sources of cosmic ray particles. In a neutrino detector, such as IceCube, there are mainly two signatures available for detection of neutrinos: The track-like light signal of a neutrino induced muon and the spherical light pattern of a neutrino induced particle shower, called cascades in this context. The search is based on the measurement of neutrino induced cascades within the IceCube neutrino detector. The data were taken in 2008/2009 with a total uptime of 367 days. At that time the detector was still under construction and had just reached half of its final size. A search for a neutrino flux using cascades is sensitive to all neutrino flavors. A cascade develops within few meters, in contrast to the muon track of several kilometers length. Therefore a good energy reconstruction is possible. With such a reconstruction the astrophysical neutrino flux can be statistically distinguished from the background of atmospheric neutrinos. In the simulation of cascades so far it was not included, that in hadronic cascades muons are produced. This can influence the shape of the cascade, to a less spherical one. Therefore the effect was parameterized in this thesis and included in the simulation. Further cuts on the event topology and reconstructed energy were developed, in order to reduce the background of atmospheric muons and atmospheric neutrinos. Four events from the measured data pass these cuts. Taking the high systematic uncertainties into account, this result is in agreement with the expected background of $0.72 \pm 0.28 \pm^{1.54}_{0.49}$ events. For an assumed flavor ratio of $\nu_e : \nu_\mu : \nu_\tau = 1 : 1 : 1$ the upper limit for the all flavor neutrino flux is $9.5 \cdot 10^{-8}\, E^{-2}\, \mathrm{GeV\, s^{-1}\, sr^{-1}\, cm^{-2}}$.

Zusammenfassung

Diese Arbeit präsentiert Ergebnisse einer Suche nach einem diffusen Fluss hochenergetischer, extraterrestrischer Neutrinos. Solch ein Fluss wird von verschiedenen Modellen zur Entstehung kosmischer Strahlung vorhergesagt. In einem Neutrinodetektor wie IceCube stehen im wesentlichen zwei Signaturen zum Nachweis der Neutrinos zur Verfügung: Das spurartige Lichtsignal eines neutrinoinduzierten Myons und das sphärische Lichtmuster eines neutrinoinduzierten Teilchenschauers, hier Kaskade genannt. Gesucht wurden neutrinoinduzierte Kaskaden mit Hilfe des IceCube-Neutrinodetektors. Die Daten stammen aus der Zeit von 2008/2009 und umfassen 367 Tage Messzeit. In dieser Zeit befand sich der Detektor noch im Aufbau und hatte etwa die Hälfte seiner vollständigen Größe erreicht. Eine Neutrinoflusssuche mittels Kaskaden ist sensitiv auf alle Neutrinoflavors. Da sich die Kaskaden nur über wenige Meter ausdehnen, ist anders als bei den kilometerlangen Myonspuren, eine gute Energierekonstruktion möglich. Dadurch kann der astrophysikalische Neutrinofluss vom atmosphärischen Neutrinountergrund statistisch unterschieden werden. In der Simulation von neutrinoinduzierten Kaskaden wurde bisher nicht berücksichtigt, dass innerhalb einer hadronischen Kaskade auch Myonen erzeugt werden. Dieses kann die Form der Kaskade dahingehend beeiflussen, dass die sphärische Symmetrie abnimmt. Daher wurde der Effekt in dieser Arbeit parametrisiert und der Simulation hinzugefügt. Weiter wurden Schnitte auf die Ereignistopologie und rekonstruierte Energie entwickelt, welche den Untergrund aus atmosphärischen Myonen und atmosphärischen Neutrinos reduzieren. Vier der gemessenen Ereignisse passieren diese Schnitte. Aufgrund der hohen systematischen Fehler ist dieses Ergebnis mit einer Untergrunderwartung von $0.72 \pm 0.28 \pm^{1.54}_{0.49}$ Ereignissen verträglich. Unter der Annahme eines Flavorverhältnisses von $\nu_e : \nu_\mu : \nu_\tau = 1 : 1 : 1$ bestimmt sich daraus die obere Grenze für den Neutrinofluss zu $9.5 \cdot 10^{-8}\, E^{-2}\, \mathrm{GeV\, s^{-1}\, sr^{-1}\, cm^{-2}}$.

Contents

1 Introduction

In 1939 Wolfgang Pauli postulated the neutrino as a particle carrying missing momentum in the β-decay. It is by design a hard to detect particle, because it only interacts over the weak force. Therefore it took until 1953, when it was first measured in the "Poltergeist" experiment.[CRH+56]

The discovery of a new kind of radiation often leads to several new applications. An example is the discovery of X-rays by Wilhelm Conrad Röntgen. He immediately used them to study different objects. So the famous pictures of the hand of Röntgen's wife was created. X-rays nowadays have several important applications in material studies and medicine. Neutrinos seem to have less impact on the daily live. They are so much harder to detect, that no far-spread applications could yet develop. However, new methods for nuclear test detection has been discussed and astrophysicists have started to look for neutrino signals. As first extra-terrestrial sources the sun and supernova SN 1987 A[PVCI09] were found. Here the neutrinos as only weakly interacting particles have a big advantage: they propagate directly from the emitter to the detector, unscattered by magnetic fields, unabsorbed by dust clouds. A hope is to use them to detect the sources of cosmic rays. The cosmic ray particles flux consists of charged nuclei with energies up to $10^{20}\,e$V. A common model to explain this flux, assumes that astrophysical objects have the ability to accelerate hadrons. In such a scenario hadron collisions would generate neutrinos through the decay of intermediately produced mesons. Thus an unobserved neutrino flux is predicted and the directions of the neutrinos could reveal the cosmic accelerators. Experiments are trying to observe this flux at energies above one TeV. One background to such a search is also linked to the cosmic ray flux: Neutrinos are created when the charged particles interact with the atmosphere. This atmospheric neutrinos could already be detected. However, the neutrinos from the cosmic ray sources are expect to have higher energies. The detection idea is hence to measure the products of a neutrino interaction. In such an interaction charged, relativistic particles are induced. In an optical transparent medium such as water or ice these highly relativistic particles radiate Cherenkov light that can be detected with common light detectors such as photo-multiplier tubes. The required detector volume is in the order of a cubic-kilometer and water or ice is used as optical medium.

From the interaction products created in a neutrino interaction the muon plays a special role. A high energetic muon can propagate over several kilometers in ice. If the muon reaches the detector, interactions rather far from the detector can still be measured. Further its track-like light pattern allows the reconstruction of the flight direction of the neutrino, as the muon will basically propagate in the same direction. However, atmospheric muons coming from above, can only be separated on a statistical basis due to their different energy spectrum compared to that of signal muons. Therefore it is difficult for an analysis to search for a neutrino signal in that region of the sky. So it is a common technique to search for

up-going muons, using the Earth as a filter for the atmospheric muon background. The remaining background consists then of atmospheric neutrinos, that can only be distinguished by their steeper energy spectrum compared to the expected signal spectrum. This requires a reconstructed energy for the neutrino, in order to either measure the spectrum or apply an energy cut. Energy losses over the long track, partly outside the detector, make the energy reconstruction a challenging problem. However, neutrino detectors can also detect neutrino induced particle showers – so called cascades, which can be found in the charged current interaction of electron and tau neutrinos and the neutral current interaction of all flavors. Such a cascade develops within few meters in ice. If a cascade is contained in the detector, all its energy is deposited in the detector, in contrast to a long muon-track, which will always lose energy outside the detector. This makes an energy reconstruction more reliable. The spherical event topology of cascades makes it, at sufficient high energies, also possible to distinguish them from the background of atmospheric muons, which have a track-like topology. Neutrino searches utilizing cascades are thus sensitive for the full sky.

If the neutrino sources are very weak, it may be difficult to detect them directly as point sources. But possible extra-galactic sources are expected to be distributed over the sky. Therefore a diffuse analysis, summing neutrino signal from all directions, is helpful method to even detect a weak astrophysical neutrino flux. For a diffuse search the lack of directional resolution is no disadvantage, but a good energy reconstruction is very important. Therefore neutrino induced cascades provide a very helpful signature for such an analysis. However, cascades require that the neutrino interacts close to the detector, while a neutrino induced muon can propagate over a long distance. So a diffuse search utilizing track-like signals is expected to be more powerful in a small detector. However, the diffuse search using cascades is a valuable cross-check to diffuse searches with neutrino induced muons: The full sky is accessible for all energies, the analysis is sensitive to all flavors and the different methods used help to verify the data taking and the used simulation and reconstruction algorithms.

This work presents a search for an extra-terrestrial neutrino flux sensitive to all flavors using neutrino induced cascades within the IceCube detector. IceCube is located at the geographical South Pole and instruments one cubic-kilometer of glacial ice in a depth between about 1 500 m and 2 500 m. Deployment was completed in December 2010, but data was already taken during the deployment. The data used is from the years 2008 and 2009. At that time the detector had half of its final size. That is about twice the size of the detector configuration from the years 2007 and 2008, which was used for a similar analysis.[IAA+11] Other, related studies using the same data sample are a search for the atmospheric neutrinos flux with cascades[Mid11] and search for an extra-terrestrial neutrino flux at lower[A+11d] and higher[Joh11] energies.

In the Chapter 2 an overview about the cosmic rays and their possible sources is given. The mechanisms of neutrino generation, propagation and interaction are discussed. Here the expected signal and background are theoretically motivated. In Chapter 3 the IceCube detector is introduced in detail. Especially the detector component for photon detection and the optical properties of the deep glacial ice are discussed. Because the analysis was done under a blindness policy[KR05], in order to avoid biases, all cuts were developed using Monte Carlo simulation data. Only 10 % of measured data were taken to verify the simulation

results. The algorithms used for simulation and reconstruction are explained in Chapter 4. Here also a digression is made, explaining the generation of muons inside hadronic cascades in detail. This is of interest as it may change the signature of the signal to some extend. The used data and the different analysis steps are presented in Chapter 5. The final results from the remaining 90 % of the data as well the systematic uncertainties are presented in Chapter 6. Finally Chapter 7 provides a summary and an outlook.

2 Theoretical Motivation and Concepts of Neutrino Astronomy

In the standard model (see e.g. Halzen and Martin[HM84]) neutrinos are the neutral leptons belonging to the charged leptons electron, muon and tau. Many properties of neutrinos are not fully determined: for example their absolute mass is still undetermined and the question remains, if they are Majorana particles[KAT01]. However, neutrinos are already a helpful tool for astrophysics. As only weakly interacting particles they propagate along a light path directly from the source to the detectors. They are only rarely scattered or absorbed by any matter on their path. So far extra-terrestrial neutrinos from the sun and the supernova SN 1987A were detected.[PVCI09] A hope is that neutrinos can point to the still unknown origin of the cosmic rays: It is expected, that cosmic particle accelerators responsible for the cosmic ray flux also generate high energetic neutrinos.[Bec08] In the following section the cosmic ray flux and the derived neutrino flux are described. Finally the propagation and the interaction of neutrinos with matter and the detection mechanism relevant for this thesis are explained.

2.1 Cosmic Rays as Motivation for Neutrino Astronomy

This section describes the cosmic ray flux. It is a particle flux from unknown, extra-terrestrial source. The spectrum of the cosmic rays is described in the following section. Then a possible scheme for particle acceleration is described and possible source candidates are discussed.

2.1.1 The Cosmic Ray Flux

In 1912 an unexpected flux of charged particles was first measured by Victor Hess[FH12]. Today this flux is well described:[Hör03,Bec08] As shown in Fig. 2.1, it follows a broken power law over a wide energy range of $1\,\mathrm{G}e\mathrm{V} < E_{\mathrm{cr}} < 100\,\mathrm{E}e\mathrm{V}$. At the so-called "knee", an energy of $E_{\mathrm{knee}} \approx 4\,\mathrm{P}e\mathrm{V}$, the spectral index changes from -2.7 to 3.1. The so-called "ankle" at $E_{\mathrm{ankle}} \approx 10\,\mathrm{E}e\mathrm{V}$ is the softening of the spectrum back to -2.8. In between another, smaller steepening at $E^{\mathrm{2nd}}_{\mathrm{knee}} \approx 400\,\mathrm{P}e\mathrm{V}$ is called the second knee. At energy of $E_{\mathrm{GZK}} \approx 60\,\mathrm{E}e\mathrm{V}$ an indication of a cutoff is observed.

In the low energy region up to $E_{\mathrm{cr}} < 100\,\mathrm{T}e\mathrm{V}$ the cross section and the high flux allows satellite measurements directly detecting the primary particle and so determining its charge and weight.[HRR03] From this region is known, that the cosmic rays of that energy regime consists of nuclei with an element distribution consistent with the element distribution in the solar system. For measurements, which not directly measure the primary particle but instead detect Cherenkov light, that is created by the reaction of cosmic ray particles with the

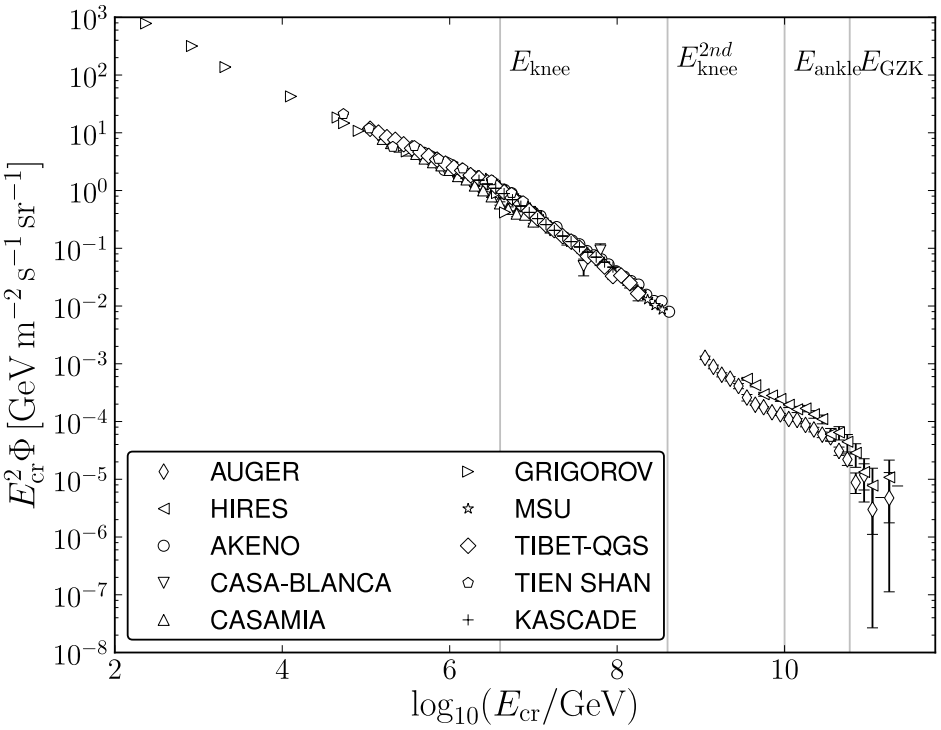

Figure 2.1: The cosmic ray flux follows a power law over a wide energy range. Shown is data from different experiments (taken from Hörandel[Hör03]). The vertical lines indicate regions where the spectral index changes. The may be connected to different sources of cosmic rays. So cosmic rays below E_{knee} are believed to be from within the Milky Way, while particles with energies above are supposed to be from extra-galactic origin. At energies above E_{GZK} a cut-off due to the GZK effect is indicated.

atmosphere, it is more complicated to determine the composition. However, these methods can be used to probe the higher energy region of the cosmic ray flux.

It is a frequent assumption that the low energetic cosmic rays are generated by supernova remnants and are thus (at least partially) from galactic origin.[Bec08] Then E_{knee} may be associated with the upper limit of the acceleration power of supernovae. The ankle could then be the energy at which powerful extra-galactic accelerators start to dominate.[BEH09] The cutoff at E_{GZK} is commonly explained with the interaction of cosmic rays with the cosmic microwave background. The proton generates Δ^+ baryons at resonance and thus loses most of its energy. This was described by Greisen[Gre66], Zatsepin and Kuzmin[ZK66].

2.1.2 Generation of High-Energetic Charged Particles

Two explanations for the highest energy particles of the cosmic ray flux are possible: Either the particles are accelerated, the so called "bottom-up" schema, or they are explained as the decay products of very heavy, exotic particles. The later theories are called "top-down" models. As Abraham et al. [A+08] shows, the model predictions are in contradiction to measurements of the cosmic ray photon flux and are thus not further considered in this thesis.

For the acceleration of charged particles Fermi[Fer49] suggested the following mechanism: The charged particle enters a region of moving, interstellar plasma with an initial energy E_0 and scatters collision-less at magnetic field inhomogeneities inside the plasma cloud and finally escapes with a probability of P_{esc}. At the point it has the energy $(1 + \delta)E_0$ as it gains energy from the moving plasma. Several iterations n may be required, in order to observe a net gain $(1 + \delta)^n E_0$.

For a general cloud of moving plasma, which can be entered and left from the particle at any side, the average energy increase δ is proportional to the square of the cloud's velocity v[Fer49]:

$$\delta \propto \left(\frac{v}{c}\right)^2 \tag{2.1}$$

where c is the velocity of light. This is called second order Fermi acceleration. In the first order Fermi acceleration the energy gain is linear to the velocity. This process works at shock fronts, which have a large extension compared to the gyro-radius of the charged particle in the magnetic field, the typical unit for the cycle length of the particle.[Gai90] So one can describe the shock front as a plane. The velocity of the front is denoted by v_{f}, the velocity of the shocked gas is v and the difference is $v_{\text{d}} := v_{\text{f}} - v$. The configuration is sketched in Fig. 2.2. In this situation the particle can only escape at the other side of the front, the downstream region, with a probability of $P_{\text{esc}} = \frac{4v_{\text{d}}}{c}$. The energy gain averaged over all incoming and outgoing angles per encounter is proportional to the velocity:

$$\delta = \frac{4v}{3c}. \tag{2.2}$$

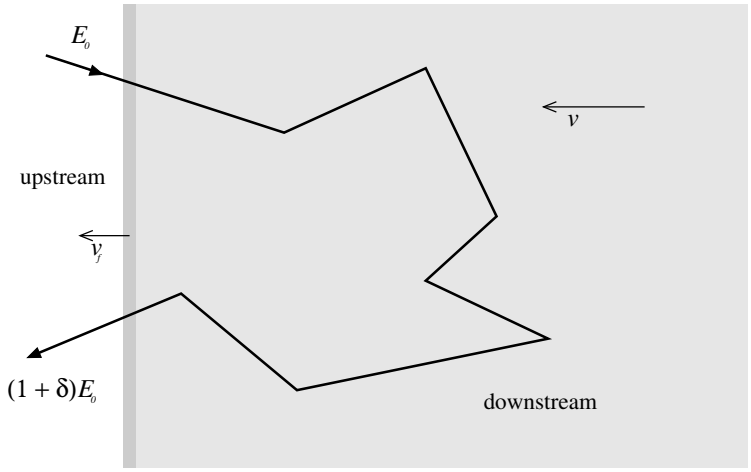

Figure 2.2: In Fermi acceleration a charged particle is accelerated due to collision-less scattering at the magnetic field of a moving plasma cloud and gains an energy δE. In the first order acceleration shown here the shock front is large and flat compared to the gyro-radius of the particle. So if it ends upstream it suffers another acceleration cycle until it finally escaped downstream. The shock front velocity is v_f, the velocity of the plasma is v.

It can be shown that Fermi acceleration results in an energy spectrum following a power law.[Gai90,Fer49] The number of particles per energy is given by this proportionality:

$$\frac{\mathrm{d}N}{\mathrm{d}E}(E) = \frac{1}{P_\mathrm{esc}}\left(\frac{E}{E_0}\right)^{-1-\kappa} \qquad \text{with } \kappa \approx \frac{P_\mathrm{esc}}{\delta}. \tag{2.3}$$

In the case of first order Fermi acceleration this results in

$$\kappa = \frac{3}{\frac{v_\mathrm{f}}{v_\mathrm{d}} - 1} \approx 1 + 4\frac{c_\mathrm{s}}{v_\mathrm{f}} \tag{2.4}$$

where the approximation due to the kinetic gas theory holds for velocities of the front v_f that are several times larger than the speed of sound c_s in the plasma. If it is even large enough to neglect the last fraction the spectral index of the particle spectrum at the source is -2. The observed -2.7 index for the region below the knee is than in agreement to this, because the observed spectrum will appear softer due to a leakage of high energy particles from the galaxy.

2.1.3 Source Candidates

Sources candidates of cosmic rays can be classified by the possible energy they can reach. As presented by Hillas[Hil84], particles escape from the sources if their gyro-radius is no longer small compared to the size of the source. This implies that the maximal energy is

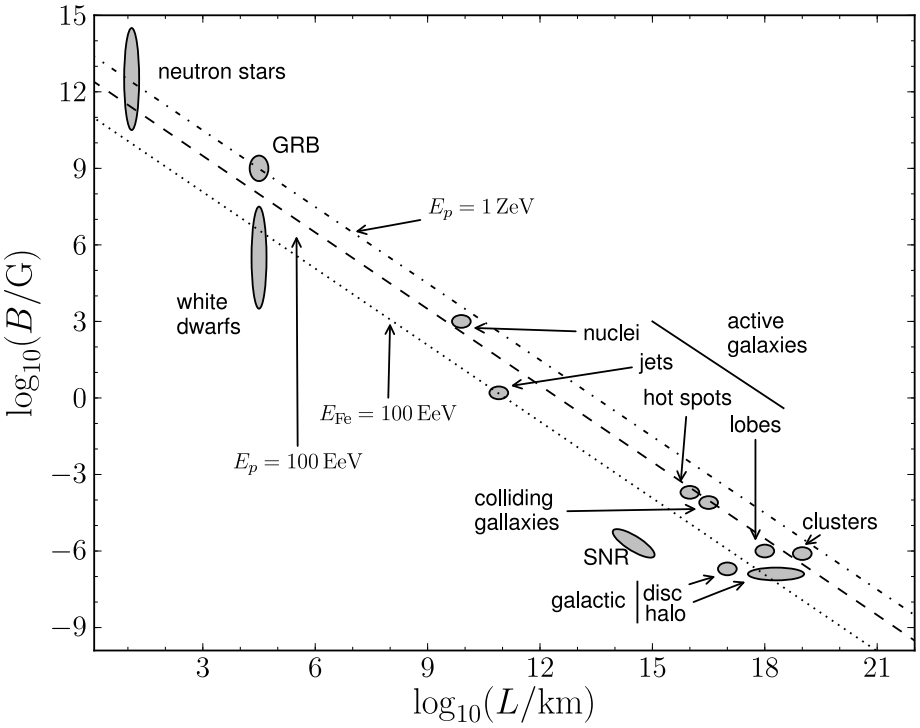

Figure 2.3: The Hillas plot shows the magnetic field strength and the size of different source candidates. The maximal energy an accelerator can reach is proportional to the product of the magnetic field, its size and the particle's charge, as given in Eq. (2.5). The diagonal lines indicate the needed magnetic field and source size for the maximal energy of 1 Z*e*V and 100 E*e*V for protons and 100 E*e*V for an iron nuclei. Accordingly, only GRBs and neutron stars could generate Z*e*V protons. Data taken from Blümer et al. [BEH09].

proportional to the inherent magnetic fields B, the charge number Z of the particle and the extension of the source L:

$$E_{\max} = \frac{10^{18} e\mathrm{V}}{\mu\mathrm{G}\,\mathrm{kpc}} \beta Z B L, \tag{2.5}$$

where $\beta = \frac{v}{c}$ is the shock velocity in units of speed of light. The typical sizes and magnetic field strengths of different astrophysical objects, which are candidates for the sources of the cosmic ray flux, are shown in Fig. 2.3. This illustrates, that candidates for sources of the highest energies are outside the Milky Way. For lower energies sources in our galaxy, such as supernova remnants, are prime candidates. The energy output of supernovae fits well with the required energy to replenish losses from particles escaping the galaxy as pointed out in Ginzburg and Syrovatskii[GS64]: A relatively small efficiency for the particle acceleration in the order of few percent would be required. The maximal energy, to which particles can be accelerated in supernova shock fronts, is calculated as $5Z \cdot 10^5\,\mathrm{G}e\mathrm{V}$[Ber96]. Other candidates (see Becker[Bec08]) for sources of cosmic rays of lower energies are pulsars, i.e rotating neutron stars, featuring extremely high magnetic field strengths. Further binary systems with a black hole or a neutron star, especially those with observed jets, the micro quasars, are promising candidates.

Only few astrophysical objects as AGN, GRBs and neutron stars are capable of accelerating particles to very high energies. Here neutron stars are the only galactic object. Especially energies above the ankle can not be explained with sources within our galaxy, because the observed flux is rather isotropic and galactic magnetic fields are too weak to explain this loss of directional information for nearby sources.[Bec08] For extra-galactic sources active galactic nuclei (AGN) and gamma ray bursts (GRB) are most promising.

AGN are Galaxy centers with very massive black holes, which capture matter from their host galaxies and erupting high energetic jets. Depending on the direction of the jets and other properties (visible in the radio frequencies, energy distribution of the observed spectrum), AGNs are differentiated into classes of objects.[A+06a] AGNs are also observed as sources of high energetic gamma rays, for which different models are discussed:[Bec08] Leptonic models would require only charged leptons, while hadronic models would, beside gamma rays and cosmic ray particles also predict the generation of neutrinos (see Sec. 2.2.1). Hence, a detection of neutrinos from such a source could help to decide between those.

GRB are short (in the order of seconds up to minutes), high intense gamma ray flashes with an afterglow in all wavelengths. They are observed from all directions and red shifts were measured in the after-glow so that they are identified to be from extra-galactic origin.[Bec08] An possible explanation can be provided, by models describing collapsing stars, which eject matter. These ejecta are hit by subsequent ejections to form shock fronts.[Sed58] The shock fronts lead to an acceleration of charged particles (see Sec. 2.1.2). The charged electrons will lose their energy due to synchrotron radiation, that escapes from the medium as soon as it is optically thin enough and is observed as the gamma ray flash. Shock fronts from the star in the surrounding, external medium will later be responsible for the afterglow.

Most of the candidates listed here have shock fronts and large magnetic fields. This makes the acceleration of charged particles with the Fermi mechanism possible. In the following it will be discussed, how the accelerators of cosmic rays can also produce a neutrino flux.

2.2 Neutrino Generation and Propagation

In this section the possible generation of an E^{-2} neutrino flux at the sources of the cosmic rays will be discussed, followed by a description of the atmospheric neutrino background. The influence of neutrino oscillations during the propagation from the sources to the observer is discussed.

2.2.1 Cosmic Neutrino Flux

The cosmic ray flux motivates the existence of particle accelerators, in particular proton acceleration. In the so called beam dump scenario these protons interact with the surrounding matter and generate pions and kaons:[1]

$$p + p \rightarrow \begin{cases} \pi^0 + 2p, \\ \pi^+ + n + p, \end{cases} \tag{2.6}$$

$$p + n \rightarrow \begin{cases} \pi^0 + n + p, \\ \pi^- + p + p, \end{cases} \tag{2.7}$$

$$p + \gamma \rightarrow \Delta^+ \rightarrow \begin{cases} \pi^0 + p, \\ \pi^+ + n, \end{cases} \tag{2.8}$$

$$n + \gamma \rightarrow \Delta^0 \rightarrow \begin{cases} \pi^0 + n, \\ \pi^- + p. \end{cases} \tag{2.9}$$

Here Eq. (2.6) and (2.7) describe the interaction with surrounding protons and neutrons, Eq. (2.8) and (2.9) describes the interaction with photons. The generated neutral pions decay to photons. The charged pions generate neutrinos in their decay:

$$\pi^\pm \rightarrow \mu^\pm + \nu_\mu(\overline{\nu}_\mu) \tag{2.10}$$

$$\mu^\pm \rightarrow e^\pm + \overline{\nu}_\mu(\nu_\mu) + \nu_e(\overline{\nu}_e) \tag{2.11}$$

It can be shown that the energies between the generated neutrinos is evenly distributed under the assumption, that the energy is not lost due to interaction of the muon, i. e. assuming that the interaction length in the source medium is much longer than the decay length.[Gai90] This also implies, that the neutrino flux spectrum follows the parent flux, that is an E^{-2} flux in the source regions (see Sec. 2.1.2). The ratio of produced neutrinos over anti-neutrinos depends on the conditions in the source. If the hadron-hadron interactions is dominant for pion generation, π^+ and π^- are created at the same amount. However, in a source where

[1] As the reactions for kaons are very similar, the following formulas are only given for pions.

the photon interaction dominates and that is also optically thin for neutrons, i. e. the process from Eq. (2.9) can be neglected, only π^+ are produced according to Eq. (2.8). So the neutrino/anti-neutrino ratio for muon neutrinos is still $\nu_\mu : \overline{\nu}_\mu = 1 : 1$, but there is no $\overline{\nu}_e$ production.[HMWY10] In this situation, the flavor ratio for neutrinos and anti-neutrinos is different at the source. Though both will change due to neutrino oscillations (see Sec. 2.2.3), a possible measurable difference may remain. In a general situation, where all processes from Eq. (2.6) to (2.9) are working, the ratio between the neutrino[2] flavors at the source is

$$\nu_e : \nu_\mu : \nu_\tau = 1 : 2 : 0 \qquad \text{(source)}. \tag{2.12}$$

That this is true independent from the energy, is caused by the previous assumption of a longer interaction length than decay length for the muons. In the case that the muons lose most of their energy in a dense source, the neutrino flavor ratio would no longer be energy independent and take the form $0 : 1 : 0$ for neutrinos of higher energies.

An upper limit for the expected neutrino flux is given by the Waxman-Bahcall bound[WB99] (III)[3]: It assumes an E^{-2} proton flux in the accelerators of the cosmic rays. The flux is estimated by the energy measured in cosmic ray experiments, i. e. the flux above the ankle generally associated to extra-galactic sources. For the upper limit one assumes, that all protons from the cosmic ray flux generate charged pions. The pion will decay in neutrinos one arrives at a flux limit for all flavors of

$$E^2\Phi = 6.8 \cdot 10^{-8} \, \frac{\mathrm{GeV}}{\mathrm{cm}^2 \, \mathrm{sr} \, \mathrm{s}}. \tag{2.13}$$

An estimate for the neutrino flux from GRBs is provided in Razzaque et al.[RMW03]. It correlates the gamma ray emission to the measured flux of high energetic cosmic rays and thus makes a prediction for the prompt phase (II) and the precursor (I). A model from Stecker[Ste05] (IV) predicts the neutrino flux produced in blazar cores. Here it was assumed that such optically thick sources produce gamma rays. Measurements of these were used for the normalization. Another model from Mücke et al.[MPE+03] assumes a special source candidate of cosmic rays to be optically thin for neutron-photon interaction, so that neutrons escape. Neutrinos will be emitted in their decay (V). A different mechanism for neutrino generation is expected for higher energies: Due to the GZK cutoff (see Sec. 2.1.1) Δ^+ baryons are generated. They decay into pions and neutrinos as given in Eq. (2.8). This is described by the model (VI)[ESS01]. The predicted all flavor flux for these different models is shown in Fig. 2.4.

2.2.2 Atmospheric Neutrino Flux

In a similar situation as at the astrophysical sources of cosmic rays neutrinos are created in our atmosphere as it is hit by cosmic ray particles. Again proton-nucleon interaction generates charged pions and kaons (see Eq. (2.6) and (2.7)). In contrast to most cosmic

[2] As for most statements the distinction between neutrinos and anti-neutrinos is of little relevance, the word "neutrinos" refers to both unless stated otherwise.

[3] Latin numbers refer to the numbers of the models shown in Fig. 2.4.

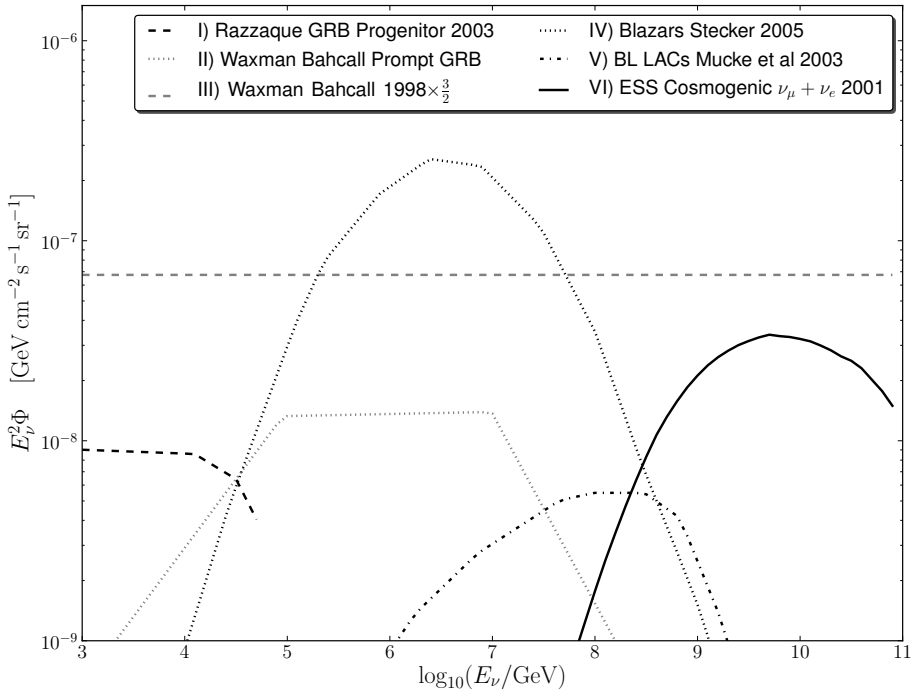

Figure 2.4: The all flavor neutrino flux prediction measurable at Earth from different models of astrophysical sources: The Waxman Bahcall line III[RMW03] gives an upper limit of neutrinos produced in cosmic ray sources (here scaled by $3/2$ as it predicts the muon neutrino flux at the sources). The models I and II, both describe neutrinos produced in different phases of GRBs.[RMW03] The flux from other source candidates (Blazars, BL-LAC objects) are given in IV[Ste05] and V[MPE+03]. A high energetic flux is predicted due too the GZK cutoff and shown as VI[ESS01].

situations the atmosphere is comparatively dense, so that the charged mesons lose energy by interaction before the decay. This steepens the spectrum from $E^{-2.7}$ for the incoming cosmic rays (see Sec. 2.1.2) to about $E^{-3.7}$ for the generated neutrinos. Also the assumption of a long interaction length for muons, as used for most cosmic neutrino sources, does not hold in the Earth's atmosphere, as muons with energies above several GeV will reach the ground before decaying. This suppresses the high energetic electron neutrino flux compared to the muon neutrino flux (see Fig. 2.5). Therefore the decay of K^0_{L} is the main contribution for the high energetic electron neutrino flux [Gai90]:

$$K^0_{\mathrm{L}} \to \pi^{\pm} + e^{\mp} + \nu_e(\overline{\nu}_e). \tag{2.14}$$

So the atmospheric neutrinos follow basically an $E^{-3.7}$ flux, with electron neutrinos highly suppressed compared to muon neutrinos. An interesting feature is expected for high energies: in the particle shower induced by the cosmic particle heavy hadrons containing charm can be created. They have live times of $O\left(10^{-12}\,\mathrm{s}\right)$ in their rest-frame, so they decay before any interaction. Neutrinos from these decays are hence called "prompt neutrinos" in contrast to the "conventional neutrinos". As no energy is lost during the propagation of the hadron, the resulting spectrum is flatter compared to the conventional flux.

A model considering composition of the cosmic rays and angular dependency for the conventional atmospheric neutrino flux is given by the Bartol group [BGL+04], a model for the prompt flux is given by Enberg et. al. [ERS08], both shown in Fig. 2.5. Together with the atmospheric muons the atmospheric neutrinos are the background for this analysis. However, the atmospheric flux is of some interest by itself: The conventional flux may serve as a calibration source and the prompt flux, which is still unobserved, could give important input to our understanding of high energetic hadron interactions. Especially the electron neutrino flux looks promising for an analysis of the prompt component, because of the suppression of the conventional electron neutrinos. Therefore the energy at which the prompt flux is of the same size as the conventional flux, is about an order of magnitude lower for electron neutrinos than for muon neutrinos.

2.2.3 Neutrino Oscillations and Flavor Ratios

As this thesis describes an analysis sensitive to all flavors, it is of interest which neutrino flavor ratio can be expected at the detector. In Sec. 2.2.1 the flavor ratios of cosmic neutrinos at the source were given. However, due to the neutrino oscillation the ratio measured at the observer is different. In the following we derive the transfer matrix, that calculates the ratio at the observer for a given source ratio.

The neutrino eigenstates $|\nu_\ell\rangle$ of the flavors $a \in \{e, \mu, \tau\}$ are linked to the mass eigenstates $|\nu_i\rangle$ with $i \in \{1, 2, 3\}$ by

$$|\nu_a\rangle = \sum_{i=1}^{3} U^*_{ai} \, |\nu_i\rangle \,, \tag{2.15}$$

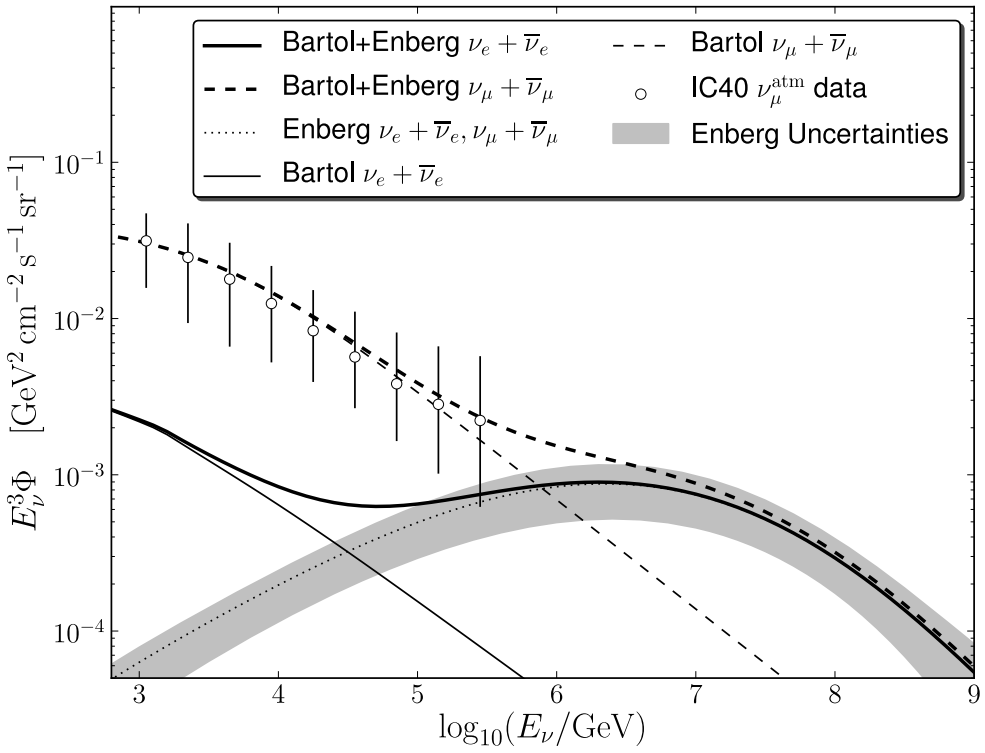

Figure 2.5: Atmospheric neutrino flux predicted by the Bartol group[BGL+04] for the conventional component and Enberg et. al.[ERS08] for the prompt component. The muon neutrino flux was measured with IC40.[A+11c] The electron neutrino flux is strongly suppressed and the intersection with the prompt component takes place at lower energies.

where (U_{ai}) is the leptonic mixing matrix. As approximation of this matrix

$$(U_{ai}) = \begin{pmatrix} \frac{\sqrt{3}}{2} & \frac{1}{2} & 0 \\ -\frac{1}{2\sqrt{2}} & \frac{\sqrt{3}}{2\sqrt{2}} & \frac{1}{\sqrt{2}} \\ \frac{1}{2\sqrt{2}} & -\frac{\sqrt{3}}{2\sqrt{2}} & \frac{1}{\sqrt{2}} \end{pmatrix} \tag{2.16}$$

will be used.[Bec08]

The next step is to express the probability of measuring a neutrino of flavor b. It is assumed that a neutrino of flavor a and energy E propagates over a distance ℓ. As derived in[AS09], the probability of measuring the flavor b is

$$P(\nu_a \to \nu_b; \ell) = \left\| \sum_{i=1}^{3} U_{bi} \exp\left(-\mathrm{i}\frac{\Delta m_{1i}^2 \ell}{2E}\right) U_{ai}^* \right\|^2 . \tag{2.17}$$

Here $\Delta m_{jk}^2 := m_j^2 - m_k^2$ denotes difference of the squared neutrino mass eigenstates.

The period between two maxima of the oscillation can then be determined as

$$L_{ij}(E) = \frac{4\pi E}{\Delta m_{ij}^2} = 2.48\,\mu eV\,\mathrm{m}\,\frac{E}{\Delta m_{ij}^2}. \tag{2.18}$$

The mass differences are $\Delta m_{21}^2 \approx 8.0 \cdot 10^{-5}\,eV^2$ and $\Delta m_{32}^2 \approx 2 \cdot 10^{-3}\,eV^2$.[Par06] Compared to astrophysical distances, this gives a short oscillation period length, so that for a diffuse flux from several sources or extended sources the oscillating term averages out[AJY00]. This simplifies the probability to

$$P_{ab} := P(\nu_a \to \nu_b) = \sum_{i=1}^{3} \|U_{ai}\|^2 \|U_{bi}\|^2 . \tag{2.19}$$

Using our approximation of the mixing matrix, Eq. (2.16), we can explicitly calculate the probability matrix:

$$(P_{ab}) = \frac{1}{32}\begin{pmatrix} 20 & 6 & 6 \\ 6 & 13 & 13 \\ 6 & 13 & 13 \end{pmatrix}. \tag{2.20}$$

The likely neutrino ratio in the sources is $\nu_e : \nu_\mu : \nu_\tau = 1 : 2 : 0$ (see Eq. (2.12)). Using the matrix from Eq. (2.20), this leads to a flavor ratio at the detector of

$$\nu_e : \nu_\mu : \nu_\tau = 1 : 1 : 1 \qquad \text{(observer)}. \tag{2.21}$$

It was also discussed, that in the case of short interaction length, compared to the decay length for the muon the source ratio could be $0 : 1 : 0$. This would then lead to an observable ratio of $\sim 1 : 2 : 2$.

Other possible scenarios, changing the observed neutrino ratios are discussed:[BBH+03] In non-standard model physics the heaviest neutrino can be unstable and thus decay, while

propagating to the observer. Depending on the mass hierarchies this can result in an extreme ratio of 6 : 1 : 1 for the normal hierarchy or 0 : 1 : 1 for the inverted. Although the 1 : 1 : 1 flavor ratio and an equal amount of neutrino and anti neutrinos is a well established assumption, the other possibilities stress the need of measurement techniques sensitive to different neutrino flavors.

2.3 Neutrino Detection

In the following it is described how neutrinos interacting with matter generate charged particles. It will be described, how charged particles propagate through matter and especially how they create light by the Cherenkov process. This leads to two different event signatures, a basically spherical, so called cascade-like light pattern as a signature created by all neutrino flavors and a track-like pattern linked to muon neutrinos.

2.3.1 Neutrino Interactions

In the standard model the neutrino only interacts over the weak force (see e. g. Halzen and Martin[HM84]). This force is mediated by the $W^{\pm}$ and the Z^0 bosons. In an interaction with a nucleon $N \in \{p, n\}$ a lepton is created and a hadronic particle shower (a hadronic cascade, X) is triggered. In the case that the force is mediated by the Z^0 boson, the created lepton is just a neutrino of the same flavor as the incoming neutrino – this interaction is called neutral current interaction (NC):

$$\nu_\ell + N \xrightarrow{Z^0} \nu_\ell + X \qquad \text{(NC)}. \tag{2.22}$$

If the $W^{\pm}$ is involved, charge is transferred to the lepton, that is then the corresponding charged lepton of the same flavor as the incoming neutrino. This process is called charged current interaction:

$$\nu_\ell\,(\overline{\nu}_\ell) + N \xrightarrow{W^{\pm}} \ell^{\mp} + X \qquad \text{(CC)}. \tag{2.23}$$

The cross sections for the interaction of a neutrino with a nucleon N is given by[GQRS96]

$$\begin{aligned}\frac{\mathrm{d}^2\sigma_{\mathrm{NC,\,CC}}}{\mathrm{d}x\,\mathrm{d}y} =& \frac{2G_{\mathrm{F}}^2}{\pi} M_N E_\nu \left(\frac{M^2_{Z^0,W^{\pm}}}{Q^2 + M^2_{Z^0,W^{\pm}}}\right)^2 \\ &\cdot \left(x q_{Z^0,W^{\pm}}(x, Q^2) + x\overline{q}_{Z^0,W^{\pm}}(x, Q^2)(1-y)^2\right).\end{aligned} \tag{2.24}$$

Here $-Q^2$ is the invariant momentum transfer, M_{N} and $M_{Z^0,W^{\pm}}$ are the masses of the nucleon and the Z^0 and $W^{\pm}$ bosons, G_{F} is the Fermi constant, $q_{Z\cdot W^{\pm}}$ and $\overline{q}_{Z\cdot W^{\pm}}$ are linear combinations of the quark and anti-quark parton density functions of the nucleon. The Bjorken

variables x and y are given by

$$x = \frac{Q^2}{2M_N\,(E_\nu - E_{\nu',\ell})} \quad \text{and} \tag{2.25}$$

$$y = 1 - \frac{E_{\nu',\ell}}{E_\nu}, \tag{2.26}$$

where $E_{\nu',\ell}$ is the energy of the neutrino or charged lepton after the interaction.

In a regime, where the momentum transfer is small compared to the boson mass ($Q^2 \ll M^2_{Z,W^\pm}$), the cross section scales linearly with energy, at about $E_\nu > 10^4$ GeV the momentum transfer reaches the same order as the boson mass. As given in[GQRS96] the cross section roughly scales with $\sigma_{NC,CC} \approx E_\nu^{0.4}$ for higher energies. A detailed model for the cross sections using collider data and extrapolating to the higher energies[L+00] is shown in Fig. 2.6. The cross section for the NC interaction is smaller than for CC interaction. Also the cross section of anti-neutrinos is smaller than the neutrino cross section. The difference becomes smaller at energies $E_\nu > 10^6$ GeV, where the contribution of the sea quarks dominates over the contribution of the valence quarks.[GQRS96] As the cross section (see Eq. (2.24)), scales with the mass of the interaction partner, the interaction of neutrinos with electrons can be neglected in most cases for these high energies. Only the generation of W^- in resonance has a very high cross section:

$$\overline{\nu}_e + e^- \rightarrow W^- \qquad \text{(Glashow)} \tag{2.27}$$

This process has a peak in the cross section at $E_{\overline{\nu}_e} = M^2_{W^-}/2M_e \approx 6.3\,\mathrm{P}e\mathrm{V}$. Notice that only anti-electron neutrinos are involved[4], so that this process could in principle be used for measuring the neutrino to anti-neutrino ratio.[HMWY10] The W^- decays into hadronic particle showers with a branching ratio of 67.6 % and into $\ell^- + \overline{\nu}_\ell$ with a branching ratio of 10.8 % for each of $\ell \in \{e, \mu, \tau\}$.[Par06]

2.3.2 Propagation of Charged Particles

In a neutrino interaction charged particles are created in the CC interaction (e. g. $\nu \rightarrow e$) or inside the hadronic cascades form all interaction types. For high energetic interactions the velocities v of these particles are close to the vacuum velocity of light c, i. e. $\beta = v/c \approx 1$. In a medium with refractive index n the particle is faster than the speed of light in the medium if $\beta n > 1$ holds. In that case light due to the Cherenkov process[Jac75] is emitted. As Fig. 2.7 illustrates, a light cone forms with the Cherenkov angle

$$\cos\theta_{\mathrm{Ch}} = \frac{1}{\beta n}. \tag{2.28}$$

The detector used for this work (see Sec. 3) detects light in ice with $n = 1.31$ (for light of $\lambda = 589\,\mathrm{nm}$ wavelength). So the Cherenkov angle is approximately $\theta_{Ch} \approx 40°$.

[4] The detector medium contains electrons but no positrons.

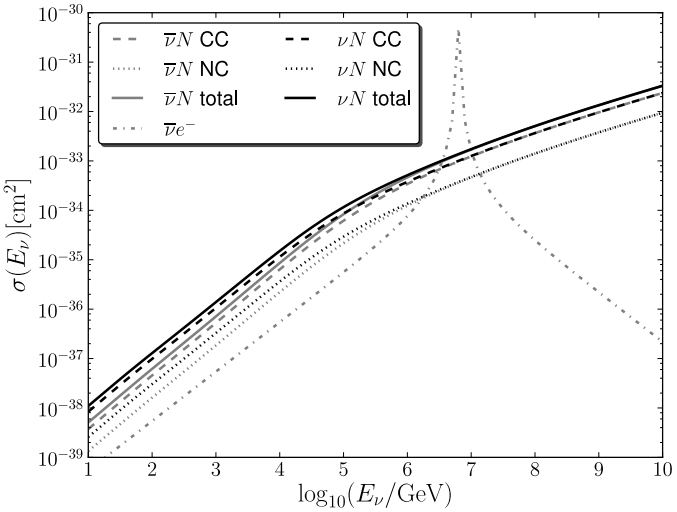

Figure 2.6: Neutrino cross sections for neutral current (NC) and charged current (CC) interaction for neutrinos and anti-neutrinos and for the resonant W^- generation. This Glashow resonance strongly peaks at 6.3 P*e*V. The cross sections for interaction with nucleons is linear with energy up to $O(10\,\mathrm{T}e\mathrm{V})$ and follows a flatter power law afterwards. The cross section for anti-neutrinos is smaller up to energies, where the contribution from the valence quarks is negligible.

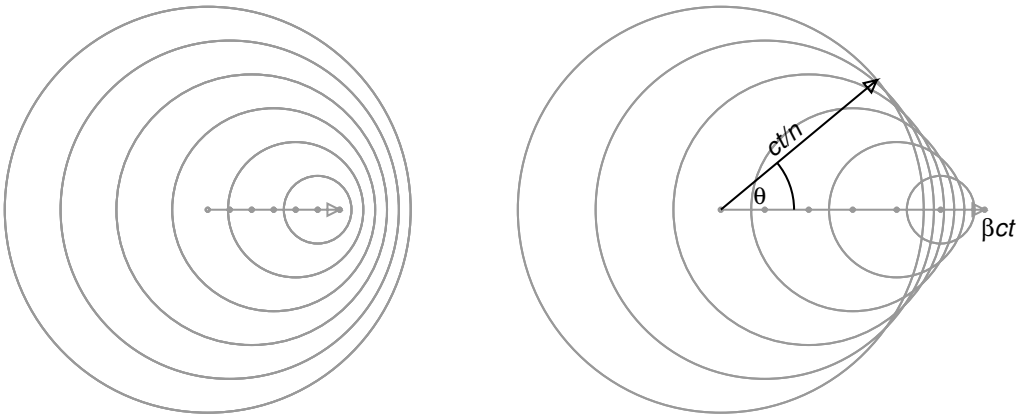

Figure 2.7: Geometry of the Cherenkov process following Huygens construction principle. Circles are lines of equal phase. If the velocity $v = \beta c$ of the charged particle in the medium with refraction index n holds $n\beta > 1$, the circles intersect at a cone with the angle θ.

The number of photons emitted by a particle with the charge of an electron along a infinitesimal distance dx is given by the Frank-Tamm formula:[Jac75]

$$\frac{\mathrm{d}^2N}{\mathrm{d}x\mathrm{d}\lambda} = \frac{2\pi\alpha}{\lambda^2}\left(1 - \frac{1}{\beta^2 n^2}\right), \tag{2.29}$$

where α is the fine structure constant. For ice and a wavelength range of $300\,\mathrm{nm} < \lambda < 600\,\mathrm{nm}$ this results in $\sim 300\,\mathrm{photons/cm}$.

In a transparent optical medium, as ice, the Cherenkov light can be used to observe high energetic, charged particles. It is now of interest, how the charged particles propagate through the detector. Charged particles, propagating through matter, lose energy due to ionization, bremsstrahlung, photo-nuclear interaction and e^+e^--pair production and δ-electrons.

For muons ionization processes dominate the energy loss for energy up to GeVs. Above those energies on the other processes surpass the ionization losses. Compared to the electron, where the bremsstrahlung process dominates, this interaction is much weaker for the muon, as the energy loss is proportional to the square of the particle mass[Gai90] and thus suppressed by a factor of $\sim 40\,000$. For muons the energy loss due to pair production is of the same order of magnitude and photo nuclear interaction about a factor three less important than bremsstrahlung. Although the interaction processes are stochastic, one can on average describe the energy loss dE per path length[5] dx as

$$\frac{\mathrm{d}E}{\mathrm{d}x} = -a - bE_\mu, \tag{2.30}$$

where $a \approx 2.7\,\frac{\mathrm{MeV\,cm^2}}{\mathrm{g}}$ describes the loss due to ionization and $b \approx 4 \cdot 10^{-6}\,\frac{\mathrm{cm^2}}{\mathrm{g}}$ the other processes.[CR04]

From this one calculates that an average 1 TeV muon propagates about two kilometer distance in ice and a 100 TeV muon has already a track length above 10 km. Even a detector located deep in the ice is reached by muons produced by cosmic rays interacting with the atmosphere.

For an electron, in contrast to the muon, the energy loss due to bremsstrahlung strongly dominates over other losses at energies above some tens of MeV. The loss can be parametrized as

$$\frac{\mathrm{d}E}{\mathrm{d}x} \approx -\frac{E}{X_0}, \tag{2.31}$$

where X_0 is the radiation length, after that the energy of the particle is in average reduced to $\frac{1}{\mathrm{e}}$ of its initial value. For ice it has a value of $X_0 = 36.08\,\mathrm{g/cm^2}$[Tsa74]. The pair production process from a high energetic photon can be approximated with the same cross sections as for the bremsstrahlung for electrons. This leads to the simple Heitler model[Hei54]: It considers electrons and photons above a critical energy[6] E_c, at which the energy loss for an electron over a radiation length due to ionization is the same as due to bremsstrahlung,

[5] It is common to define $x := \rho\ell$, i. e. length times medium density and use corresponding units.
[6] The value for ice is $E_\mathrm{c} = 78.99\,\mathrm{M}e\mathrm{V}$.

i. e. electrons with lower energies will be mostly stopped by ionization and not create much bremsstrahlung. In the model a photon creates an electron-positron pair and an electron creates a bremsstrahlung photon after one radiation length. The energies are distributed equally to the secondaries. From this immediately follows, that the shower length scales logarithmic with primary energy ($L \propto \log E_0$) and that the number of generated particles is proportional to the energy ($N \propto E_0$). As the charged particles generate light along the track, the second statement claims together with Eq. (2.29) that the generated light is proportional to the energy of the primary particle.

This simple picture of the radiation length being energy independent holds up to energies $\sim 100\,\mathrm{T}e\mathrm{V}$. For higher energies the finite length of the interaction need to be taken into account: The longitudinal momentum $q_\parallel$ transferred to the nucleus can be described as

$$q_\parallel \propto \frac{m_e^2 E_\gamma}{E_e(E_e - E_\gamma)}, \tag{2.32}$$

where E_e, E_γ is the energy of the incoming electron and the created photon, respectively, and m_e the electron mass.[Kle99] From the uncertainty principle follows, that the position of the interaction vertex is located within the so called formation length

$$\ell_\mathrm{f}^0 = \frac{\hbar}{q_\parallel}. \tag{2.33}$$

If this length is larger than the inter-atomic distance in the medium multiple scattering at different nuclei needs to be taken into account. This effect is called after Landau, Pomeranchuk and Migdal (LPM). So the momentum transfer will be larger and the real formation length shorter:

$$\ell_\mathrm{f} = \ell_\mathrm{f}^0 \sqrt{\frac{E_\gamma E_\mathrm{LPM}}{E_e(E_e - E_\gamma)}} \tag{2.34}$$

As the cross section scales with the formation length, the interaction is suppressed by $\sqrt{E_\gamma E_\mathrm{LPM}/\left(E_e\left(E_e - E_\gamma\right)\right)}$, where $E_\mathrm{LPM} = 303\,\mathrm{T}e\mathrm{V}$ for ice.[GK10]

So far cascades from electrons, so-called electromagnetic cascades were described. Hadron induced particle showers, hadronic cascades, need a more sophisticated description, as more different processes need to be considered. Such a cascade can be separated into a hadronic component and an electromagnetic component. The electromagnetic component is generated by neutral pions, that decay into photons. As the fraction of produced π^0 increases with energy, the electromagnetic component becomes dominant for high energies. However, the hadronic part will generate less light than an electromagnetic cascade for the following reasons: The needed binding energy of the hadrons reduces the available kinetic energy. Further the charged hadrons are heavier than electrons and thus need more energy to fulfill the Cherenkov condition of $\beta n > 1$. And as a third also a large amount of neutrons is generated in a hadronic cascade, which remain invisible.

A simple model for hadronic cascades will be given in Sec. 4.3. In that section the main focus is to describe the muon production, that takes also place in a hadronic cascade. The section also compares the analytic model to simulation data.

In this section it was shown, how neutrinos create muons and cascades, which are both generating Cherenkov light. The signature of a muon will be a light cone moving along a track, while the signature of a cascade will be a more localized light pattern. Depending on the optical properties of the surrounding medium, the signal from a cascade can be smeared out, so that it in principle can be seen as a spherical light pattern starting from one point. In the following chapter the IceCube neutrino detector will be discussed. It uses the clear ice as a optical medium to observe the described neutrino signatures.

3 The IceCube Detector

3.1 Design of the Detector

The neutrino detector IceCube is based on the Cherenkov detection principle (compare Sec. 2.3.2) and thus uses the clear ice of the geographic South Pole as an optically transparent medium.[A+01,A+06b] The deployment was finished at the end of 2010.[W+07a]

3.1.1 Detector Components

The main component of the detector is the in-ice part, instrumenting a volume of about one cubic-kilometer of ice in a depth from 1.5 km to 2.5 km. 4 800 digital optical modules (DOMs) are placed on 80 strings (60 DOMs per string) in a hexagonal grid with a x-y[1]-spacing of 125 m and a z-spacing of 17 m.[A+01,IA+06] The DOM is a glass sphere housing a photo-multiplier and digitization electronics (see Sec. 3.1.2). The in-ice detector will be complemented by a low-energy extension called Deep Core (DC), consisting of 360 DOMs equipped with higher quantum-efficiency PMTs on 6 strings with a spacing of 72 m in x-y, 7 m in the z-direction.[R+09,A+10] The first Deep Core string was deployed in 2009.[W+07a]

The data analyzed in this work is taken with the 40-string configuration ready in 2008 (IC40, see Fig. 3.1). At this time IceCube's predecessor AMANDA[A+00] was still in operation. This detector had a smaller spacing with x-y-distances of 30 m to 60 m and a z-spacing of about 20 m and is thus of interest for low energy events. Unlike Deep Core, it was located in shallower, less clean ice (see Sec. 3.2), closer to the border of the IceCube detector and the optical modules were of different designs and not all digital, so that their analog output requires special treatment.[Tep09] For this work AMANDA was not used, but a similar analysis[Rut10] searching for the atmospheric neutrino flux was applied on the combined data of 2008.

Another complement to IceCube is the air shower detector array IceTop[NN03]. It consists of 81[W+10a] (40 in 2008[K+08]) stations. A station consists of two ice-filled tanks, each housing two DOMs. Already of scientific interest as a standalone experiment, the combination of in-ice detector and air shower detector enables the study of the muon component in air showers[A+01,F+09] or vetoing for air showers for an in-ice analysis.[A+01,Ber10] Using IceTop as an effective veto, however, requires a readout configuration[2] that was not available in IC40,[Ber10] so this vetoing technique was not applied. However, it is worth studying it for later configurations.

[1] IceCube uses a right handed Cartesian coordination system with the origin at 46 500 ft eastings, 52 200 ft northings, in the survey coordinate system for the South Pole station comoving with the glacier, at an elevation of 2900 ft, z pointing towards the surface and y pointing towards Greenwich (UK).[W+10b]

[2] Soft local coincidence (SLC) readout as described below.

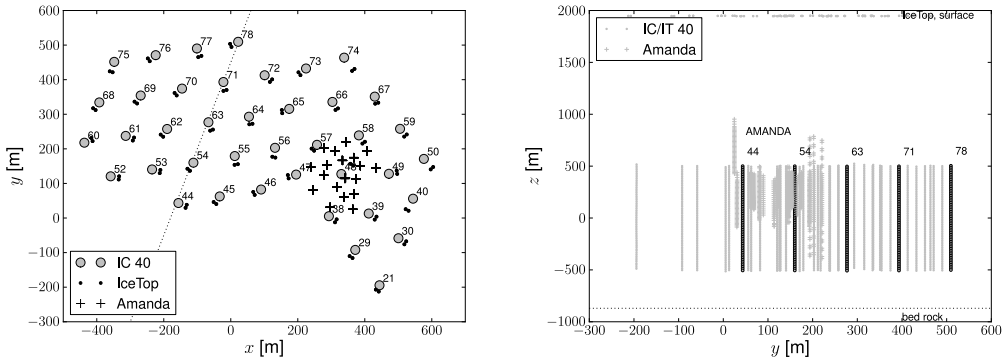

Figure 3.1: IceCube Detector in 2008 (IC40). The positions of the IC40 IceCube strings are shown as circles, Amanda strings as crosses, IceTop tanks as small dots. Left, projection in the *x*-*y*-plane. Right, projection in *y*-*z*-plane. Strings in on the dotted line in the left plot are highlighted.

3.1.2 Digital Optical Module

The basic component of the IceCube detector is the digital optical module[3] (DOM).[4] A DOM is a 13 inch glass vacuum vessel[A+01] housing a photo-multiplier tube (PMT) and the electronics for recording, digitizing and calibrating its output together with LEDs that are used to calibrate the full detector and measure the optical properties of the ice (see Sec. 3.2 and Sec. 6.1).

For the photon detection a 10 inch diameter R7081-02 photo-multiplier tube (PMT) made by Hamamatsu Photonics was chosen. It has a spectral response from 300 nm to 650 nm and a quantum efficiency of 25 % at 390 nm and a transit time spread of 3.2 ns.

It is glued with a flexible, transparent gel to the glass in order to give mechanical stability and optical coupling. The glass of the sphere is a borosilicate glass with a low potassium content, being a compromise between good mechanical properties, broad transparency window up to 350 nm and a low potassium content, reducing the background radioactivity from ^{40}K.[A+01]

The signal from the PMT is split to a 75 ns delay line and a discriminator with a threshold in nominal settings[H+07] corresponding to 0.25 photo electrons (PE). If the discriminator triggers, the delayed signal will be sampled by one of two Analog Transient Waveform Digitizers (ATWD)[5] and a flash analog-to-digital converter (fADC). The ATWD is a special device providing a sampling rate of about 300 MHz over a time window of 450 ns. It has 4 channels, each capable to store 128 samples at a 10 bit resolution. One of them is used for special proposes (measuring the LED voltage during flasher runs and for calibration); the others digitize the PMT output, each at a different gain (×0.25, ×2 and ×16) for maximum dynamic range. The fADC has a much coarser sampling rate of 40 MHz but can

[3] This is in contrast to Amanda's optical modules (OMs, see Andres et al.[A+00]).

[4] Unless cited otherwise, the statements of this section are based on Abrasi et al.[A+09].

[5] The ATWD are set to alternate with each other in order to reduce dead time

record the PMT output for 6.4 µs. The recorded waveformes are calibrated, combined, and characterized later in software (see Sec. 4.4.1).

The bundle of digitized waveforms recorded by the DOM when its discriminator fires is called a "launch." This bundle is only send to the surface, if the discriminator of at least one of the nearest or next-to-nearest neighbor DOMs on the string triggers as well (hard local coincidence, HLC[V+09a]). This reduces traffic due to hits caused by background radioactivity. Starting in 2009, a coarse charge stamp is send to the surface if the HLC condition is not fulfilled; this is called a soft local coincidence (SLC) launch. The local coincident logic is implemented on the main-board of the DOM using a Field-Programmable Gate Array (FPGA) and controlled by a CPU. This allows flexible settings and the control of calibration electronics like the flashers.

The data recorded by the DOMs on one string is read out by a controlling computer, the DOMHub. It time-orders and buffers the launches and sends them to the Event Builder. Here, trigger criteria are applied to the launches from all strings. For this work the simple majority trigger SMT8 was used: It is fulfilled if eight or more launches occur within 5 µs of each other.[H+07]. This cluster of launches is extended by 4 µs before the first launch and 6 µs after the last launch. Other triggers generate similar time windows. All launches in overlapping time windows are combined to form an event. The stream of events is then send to a cluster of filter computers in order to extract interesting events to be send to the North by satellite (see Sec. 4.4).

3.2 Ice Properties

Detailed knowledge of the material properties in the detector is needed in order to correctly simulate and understand the detector response. For IceCube this involves understanding how the varying optical properties of the glacial ice influence the propagation of Cherenkov photons from their sources to the DOMs. The ice can be characterized by its group and phase index of refraction, absorption coefficient $a(x, y, z, \lambda)$ and scattering coefficient $b(x, y, z, \lambda)$ as function of position x, y, z and wavelength λ of the light. The absorption coefficient is defined as the reciprocal of absorption length ℓ_a, the length after which the survival probability of a photon has decreased down to $\frac{1}{\mathrm{e}}$. Similarly the scattering coefficient is defined as the reciprocal of the scattering length ℓ_s, the average length between two scattering events. Scattering in ice is not isotropic and so the anisotropy $\langle \cos\theta \rangle$, the average cosine of the scattering angle is needed. The anisotropy can be calculated using Mie theory and an assumption about the size and shape of the dust particles in the ice.[A+06b] Instead of directly measuring the scattering length, one measures the effective scattering length ℓ_e, after which the scattering is isotropic. The effective scattering coefficient is defined as the reciprocal of the effective scattering length $b_e = \frac{1}{\ell_e}$. The effective scattering length is connected to anisotropy and scattering length by the formula

$$\ell_e = \frac{\ell_s}{1 - \langle \cos\theta \rangle}. \tag{3.1}$$

These properties need to be determined as a function of depth between 1 000 m and 3 000 m. Since the holes for the Amanda/IceCube strings where drilled using hot water[A+01], no drill cores are available for direct measurements.[6] The most direct measurement of the dust concentration in the detector volume comes from the "dust logger"[B+10], that was deployed in some of the IceCube holes[W+07b]. The main method for measuring the optical properties is to record the signal of artificial light sources like flashers and lasers in AMANDA and IceCube with the DOMs/OMs.

The basic finding is very clear ice in a region below 2 100 m. At depths between 1 500 m and 2 000 m dust peaks related to climatic changes in the past and volcanic eruptions[A+06b] significantly decrease scattering and absorption lengths. Above 1 300 m the scattering length decreases strongly due to bubbles in the ice, that are not stable at the high pressures present at greater depths.[A+06b] In this last region scattering increases drastically, while absorption is similar to the dust peak below 2 000 m depth.

The model of ice properties used for most of the thesis (AHA[W+08]) is based on the light measurement with AMANDA[A+06b], with the derived properties shown in Fig. 3.2 and data from a core drill[B+10] from sites about 1 000 km away for the deep regions below 2 100 m. The newer model (SPICE 1[C+10a]) is based on IceCube flasher data and shown in Fig. 3.3 in comparison with AHA. More advanced versions of this model incorporate dust logger and drill core data.[Chi10] While both AHA and SPICE 1 only have a layer structure in z-direction and are flat in x-y, newer models[C+10b] have a tilted layer structure, which removes symmetries necessary for tabulating the light propagation through ice as it is done by Photonics[L+07]. These models require direct light simulation as done by PPC[V+09b] and are hard to utilize for reconstruction due to the time requirement of directly simulating the light propagation. The detailed description of the simulation process is given in Sec. 4.1.3, the use of the ice properties for reconstruction is discussed in Sec. 4.4.6.

[6] Ice cores from other regions[A+06b,B+10] can, however, be used for rough comparisons.

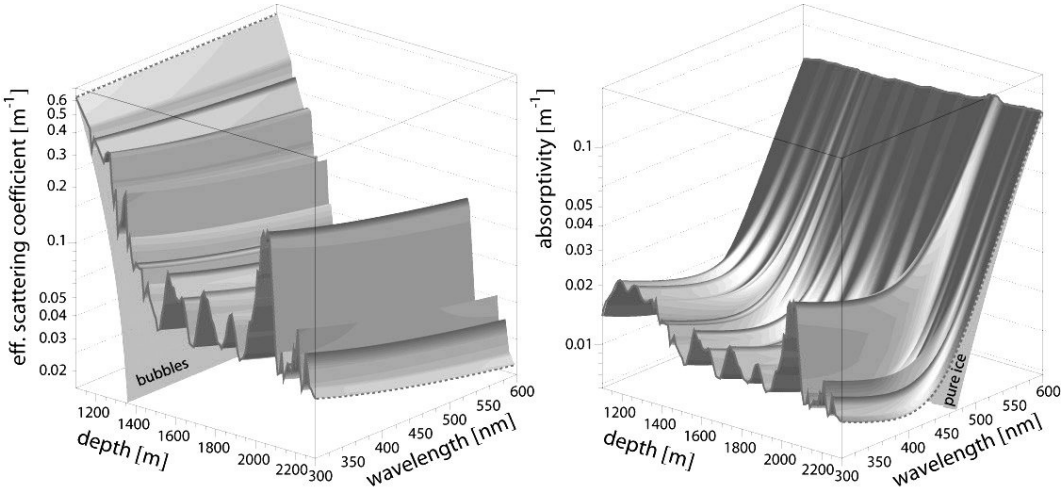

Figure 3.2: Scattering and absorption coefficients measured with AMANDA: Both coefficients shows peaks due to dust in the 1 500 m to 2 000 m, in the upper region scattering is dominated by bubbles in the ice, for larger wavelength the ice becomes more opaque. Regions below the dust peaks have very clear ice. (Plot taken from Ackermann et al.[A+06b].)

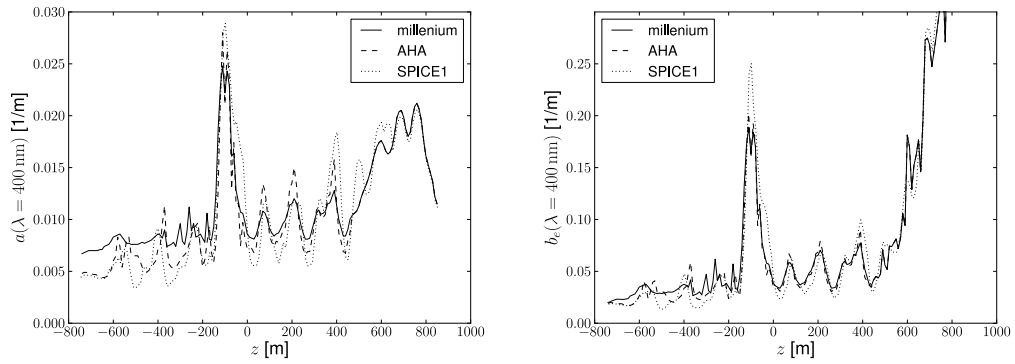

Figure 3.3: Different Ice Models: The absorption coefficient a (left) and the effective scattering coefficient b_e (right) at a wavelength $\lambda = 400\,\mathrm{nm}$. All models show the layer structure due to dust in the ice. The scattering in regions above $z = 600\,\mathrm{m}$ is high due to bubbles. The millennium model is based on the measurements from AMANDA (compare Fig. 3.2) and known for being inaccurate in regions below $z = -200\,\mathrm{m}$. This was improved by the AHA model, which uses drill core data in this region and stretches the peak structure above. The new SPICE model is a fit to IceCube flasher data, and seems to better describe the deep region and show some differences in the form of the peak.

4 Simulation and Reconstruction

The analysis described in this thesis (see Chapter 5) searches for a weak signal on a large background. This requires powerful algorithms to separate signal from background. In order to avoid biases the analysis is performed in a blind manner, i. e. it is optimized without using the measured data. Therefore the cut optimization is based entirely on Monte Carlo simulations (MC).

The algorithms used in the simulation will be discussed in the following section, followed by a description, how MC data can be use for different proposes by differently weighting the events. Looking at the description of hadronic cascades in detail, a digression on muon production in hadronic cascades is made. Finally algorithms used for the reconstruction of data and MC are described.

4.1 Simulation Steps

MC data for cosmic ray muons (also referred to as CORSIKA MC) and atmospheric neutrinos are needed for the background prediction, while neutrino events of all flavors following a E^{-2} flux are used for the signal estimation. It can happen, that while the detector is measuring a (background) event, a muon from another air shower crosses the detector and is recorded. In the simulation these coincident events are simulated separately. Furthermore, several data sets with modified simulation schemes such as assuming different DOM efficiencies or ice models are required for studies of the systematic errors (see Sec. 6.2). Detailed information about the used simulation data set are provided in Sec. 5.1.

The simulation begins with an event generator: CORSIKA for cosmic ray muons, neutrino generator for the neutrinos. These primaries are propagated toward the detector and interactions are simulated. Then the light yield in the detector is calculated using photonics[L+07] (or the alternative PPC[V+09b], compare Sec. 3.2). Finally, the response of the detector electronics is simulated.

4.1.1 Generators: Cosmic Ray Muon Generator CORSIKA and neutrino generator

A modified version[Chi03,Chi04] of CORSIKA 6.735[HP09] is used for the simulation of cosmic particle air showers. Here the full shower development is simulated, were unlike in the default version, different primary particle types can be simulated in the same run. This allows to use models with complex flux composition. For this thesis the polygonato model from Hörandel[Hör03] was used. In order to describe the hadronic interactions taking place during the shower development the models Gheisha and Sibyll were used. The simulation spectrum can be the cosmic ray flux given by the used model or such a spectrum multiplied

by the primary energy in order to over-sample higher energy particles (compare Sec. 4.2). After the air shower simulation, muons reaching the ground are propagated by the Muon Monte Carlo module[CR04] described in the next section. The further information from the shower is not used for this work. It should be mentioned, that the simulation settings needed for a fast simulation of the muon component are not sufficient for simulating the IceTop response to the air shower, so that this aspect was not included in the simulation.

The neutrino generator is based on Anis[GK05]. It simulates a given neutrino flux, normally E^{-1} or E^{-2}, which is reweighted later during the analysis (see Sec. 4.2). The neutrinos, isotropic distributed over the surface, are propagated through the Earth including neutral and charged current interactions and the resonant W boson generation for $\bar{\nu}_e$ (compare Sec. 2.3.1). For the neutrino cross section the CTEQ 5 model[L+00] was used; for systematic studies the newer model CSS[CS08] was applied. The neutrinos were forced to interact within a cylinder parallel to the neutrino direction with a radius of 1 000 m and a length of 2 000 m centered at the detector origin. The resulting hadronic cascade and/or lepton is handed over to the corresponding propagator described below.

4.1.2 Simulation of Muon Interaction and Propagation and Cascades

The MMC module[CR04] propagates muons and taus in a similar way. The muon (or tau) loses energy due to ionization losses, bremsstrahlung, pair production and photo-nuclear interactions (see Sec. 2.3.2). All these effects are stochastic, however, it is a necessary simplification to handle these effects for smaller energies than $E_c = vE_\mu$ (with the muon energy E_μ) as continues losses. To propagate the lepton towards the detector relatively fast calculation with $v = 0.05$ is done. If it reaches a cylinder with a height of 1 700 m and a radius of 2 000 m around the detector the threshold for stochastic losses is lowered to $E_c = 500\mathrm{M}e\mathrm{V}$. When it leaves the volume again the expected length of the full track is simulated in a single step ($v = 1$).

Various charged particles will create a particle shower in ice. The shower is not simulated in detail. The particle is rather handled as a static, point-like, generic light source. However, the longitudinal energy profile and also the generation of muons inside hadronic cascades may change the form of this light-source dramatically and are thus considered for cascades belonging to a neutrino interaction. Cascades from bremsstrahlung processes on muon tracks or from a tau decay are at the moment still considered point-like and their longitudinal profile is not taken into account.[1] However, no big effect is expected from this simplification, as the event shape is largely determined by the track in cases when the cascades are simulated point-like.

To correctly simulate the longitudinal elongation of a cascade the "Cascade Monte Carlo" (CMC) module[V+07,Voi08] is used. In order to handle hadronic and electromagnetic cascades in the same way, the energy of the hadronic cascade is scaled to the energy of an electromagnetic cascade with the same average light yield following the parameterization from M. Kowalski[Kow02]. Electromagnetic cascades below an energy limit of $E_{\mathrm{cscd}} < 1\,\mathrm{T}e\mathrm{V}$ are

[1] The technical reason: Two modules are involved: MMC calculating bremsstrahlung processes and the track length and CMC calculating the muon generation in hadronic cascades and the length of the cascade. At the moment this modules need to be called after each other, the order CMC, then MMC was chosen.

not modified and are handled in the simulation as anisotropic point-like light sources and are directly handed over to the light propagator. For higher energies the extension of the cascade is handled by splitting the original cascade into several lower energy cascades in steps of three radiation lengths along the cascade direction. For energies below a threshold $E_{\mathrm{LPM}} = 1\,\mathrm{P}e\mathrm{V}$ the energy distribution is parameterized with a gamma distribution:

$$\frac{\mathrm{d}E}{\mathrm{d}x} = E_0 b \frac{(bx)^{a-1}\exp(bx)}{\Gamma(a)}, \tag{4.1}$$

where x is the shower depth in radiation lengths and the parameters a and b were determined by C. Wiebusch [Wie95]. Above this threshold the radiation length can no longer be assumed to be constant. The shower profile becomes dominated by stochastic losses and the Landau-Pomeranchuk-Midgal (LPM) effect [LP53], as described in detail in Sec. 2.3.2, leads to the extension of the shower. So in this energy region a one dimensional Monte Carlo simulation using the formulas of Klein [Kle99] is performed. For hadronic cascades the generation of muons with energies above $1\,\mathrm{G}e\mathrm{V}$ is simulated (see Sec. 4.3) if the cascade energy is sufficient.

4.1.3 Light Propagation and Detector Simulation

The light from the propagated particles has to be simulated and propagated to the DOMs. For the simulation, scattering and absorption of light – following the coefficients given by the used ice model, see Sec. 3.2 – has to be taken into account. Though a simulation of these processes event by event is possible in an efficient way using GPUs with the PPC [V+09b] module, for most of the simulation used in this work the light propagation was done separately and tabulated by photonics [L+07]. This is possible by assuming that the ice has a horizontally flat, layered structure (as in the AHA [W+08] and SPICE1 [C+10a] model) and that the light output scales with energy and so reducing the number of needed parameters from nine down to five:

- z-position of the source
- z-position of the DOM
- distance between source and DOM
- zenith of the source direction
- angle between source direction and DOM

The tables were generated in the following way: For every source position and direction a large number of photons were created and propagated through the ice. During the propagation the photon can scatter in each step. Absorption is taken into account by weighting the photons with the surviving probability. The photons are recorded, whenever they enter a bin for the DOM position. Two topologies of the light source used for the generation of photons are available. One describes the light generated from a cascade, the other describes the light of a short muon track. [Wie95] A row of such short muon tracks is summed up, in

order to calculate the light generated by a starting track with a given starting point. By subtraction of the table contents for two tracks with the same direction but different starting points, the table value for all tracks of finite length can be calculated.

These tables can be directly used for the simulation. In the reconstruction the light simulation is needed for formulating a likelihood function (see Sec. 4.4.6). As this likelihood function needs to be minimized, it is desired, that it is continuous and smooth. Therefore the tables are smoothed before used in the event reconstruction. However, J. van Santen [vS10] showed that this solution brings several problems, as the maximum of the likelihood being far away from the simulated point and still problems with kinks at bin corners remain. It was proposed J. van Santen and N. Whitehorn [vSW10] using B-splines for interpolation to solve these problem. This would guarantee a smooth likelihood with higher accuracy, even with the advantage to be analytically differentiable.[2] However, this was not yet available for this work.

In the simulation process these tables are read and used by the module hitmaker to simulate the measured charge. For each DOM and given particle (i. e. tracks and cascades) a number of hits following a Poisson distribution and the arrival time for each of the hits are simulated. Then the module Domsimulator calculates the electronic response and simulates discriminator settings and local coincidences (see Sec. 3.1.2). After this the trigger conditions (see Sec. 3.1.2) are applied. From this point on simulated data are handled in the same way as measured data.

4.2 Simulation Weights

Instead of simulating the events according to the cosmic ray spectrum as an unweighted MC sample it is useful to over-sample higher energies and apply weights to take the over-sampling into account. For neutrino simulation a weight needs to be applied because the interaction was forced, as an unweighted simulation with such low interaction cross sections would not be feasible. Here a reweighting also gives the possibility to use one simulated neutrino data set to describe different flux models, e. g. an atmospheric neutrino flux and an extra-terrestrial E^{-2} flux.

4.2.1 Weights in different kinds of MC

For each CORSIKA event i in a file j there is a flux weight W_i^{flux} such that the number of expected events in a file specific time T_j is the sum of weights.[3] In the unweighted case with the cosmic ray flux $\Phi(E)$ all weights are one and the time for which the events were generated is

$$T_j = \frac{N^{\text{gen}}}{A^{\text{sum}} F^{\text{sum}}}, \tag{4.2}$$

[2] The gradient of the likelihood can be used in the minimization process and the Hessian yields information of the fit quality.

[3] This section is based on P. Desiati and J. C. Díaz Vélez [DV09].

where N^{gen} is the number of generated events, A^{sum} the simulation area integrated over the simulated solid angle and F^{sum} the energy integrated flux:

$$F^{\text{sum}} = \int_{E_1}^{E_2} \mathrm{d}E\, \Phi(E) \tag{4.3}$$

In order to over-sample higher energies, weighted CORSIKA data sets are produced. Instead of simulating the cosmic ray flux, a modified flux Φ' is sampled:

$$\Phi'(E) := \Phi(E)\frac{E}{E_0} \tag{4.4}$$

To compensate this, the weights are defined in an energy dependent way:

$$W_i^{\text{flux}}(E_i) := \frac{E_0}{E_i} \tag{4.5}$$

Also the time scale Eq. (4.2) has to be modified by replacing the integrated flux F^{sum} of the cosmic ray flux with the integrated flux for the modified flux. That means Φ has to be replaced by Φ' in Eq. (4.3).

There are different CORSIKA data sets for single, double and triple coincident events. To simulate coincident events two or three simulated events which hit at least one DOM in the detector are combined. If the rate of such events before combination is f the probability of having n events in a time window τ is given by Poisson probability

$$P(n, f\tau) = \frac{(f\tau)^n \mathrm{e}^{f\tau}}{n!}. \tag{4.6}$$

This probability needs to be applied in the weighting scheme and is called the "diplopia weight" $W_i^{\text{dipl}} = P(n, f\tau)$. So the expected rate for one event i while combining J files is given by the weight

$$w_i = \frac{W_i^{\text{flux}} W^{\text{dipl}}}{\sum_{j=0}^{J} T_j}. \tag{4.7}$$

In the neutrino generator an interaction of the neutrino is forced in the detector volume (see Sec. 4.1.1 and A. Ishihara and S. Yoshida[IY06]). To correct for this, weights w_i^1 incorporating the interaction probability are assigned to each event i to normalize them to one event per GeV cm^2 sec sr.[D+07] Reweighting to a given flux Φ is done by calculating the weight

$$w_i = \frac{w_i^1}{N^{\text{gen}}} \Phi(E_i, \alpha_i). \tag{4.8}$$

Here N^{gen} is the number of generated events, E_i is the energy of the simulated event and α_i stands for further parameters of the flux, like particle type and direction. To calculate the atmospheric flux, the module neutrinoflux[MDV+] is used (see Sec. 5.1 for the used models).

4.2.2 Errors and Life Time of Weighted MC

In the unweighted case the measurement error of a Poisson process with expectation value N_{exp} is the square root of the value, so the error of a measured rate $f_{\text{exp}} = \frac{N_{\text{exp}}}{T_{\text{exp}}}$ with measuring time T_{exp} is:[BSMM01]

$$\sigma = \frac{\sqrt{N_{\text{exp}}}}{T_{\text{exp}}}. \tag{4.9}$$

In the case of weighted data, calculating error propagation one finds for N data points i with weights w_i and so a predicted rate of $f_{\text{MC}} = \sum_{i=0}^{N} w_i$ that the error is given by

$$\sigma = \sqrt{\sum_{i=0}^{N} w_i^2}. \tag{4.10}$$

The weights as defined above agree with the experimental rate $f_{\text{MC}} = f_{\text{exp}}$, i. e. the following equation is fulfilled:

$$\sum_{i=0}^{N} w_i = \frac{N_{\text{exp}}}{T_{\text{exp}}} = f_{\text{exp}}. \tag{4.11}$$

It is helpful for comparison to know the time T_{eff} in which the experimental error, is the same as the MC error.[D'A09a,KH07] This time is called effective life time and follows from combining Eq. (4.9), (4.10) and (4.11) as

$$T_{\text{eff}} = \frac{\sum_{i=0}^{N} w_i}{\sum_{i=0}^{N} w_i^2}. \tag{4.12}$$

4.3 Muon Production in Hadronic Cascades

In Sec. 4.1.2 the modeling of cascades for the simulation was briefly described. One part of that is the production of muons in hadronic cascades. This effect was studied and implemented in this work and will be described in the following section. A simple analytic model is used, to motivate the parameterization and provide some understanding of the influence of different model parameters. Afterwards data from a detailed shower simulation in water is analyzed and a parameterization of the process is given.

4.3.1 Analytic Model for the Muon Flux

The basic properties of electromagnetic showers can be understood through the Heitler model[Hei54]. After one interaction length a photon creates an electron-positron pair, which radiates bremsstrahlung photons. This repeats every interaction length while the energy is distributed over the generated particles, so that more and more particles with lower and lower energies are created until the energy is not sufficient for another pair creation. Hadronic showers are more complicated, since in each interaction a wide range of hadronic particles can be created, which in their interaction or decay increase the complexity further.

However, expanding the simple Heitler model helps to get a basic understanding of muon generation in hadronic cascades.

This work follows the extended Heitler model presented in the thesis of S. Zimmer[Zim08] and in the paper of S. Panknin et al. [PBKZ09] and based on a work from J. Matthews[Mat05]. We consider a hadronic shower generated by a particle of primary energy E_0. In each interaction $N_{\mathrm{mul}} \approx 10$ hadrons are produced. About one third of them will be neutral mesons like π^0, which will lead to an electromagnetic sub-shower.

In generation n we have $N_{\mathrm{H}}(n)$ hadrons with average energy E_{H}:

$$N_{\mathrm{H}}(n) = \left(\frac{2}{3} N_{\mathrm{mul}}\right)^n, \tag{4.13}$$

$$E_{\mathrm{H}}(n) = \frac{E_0}{N_{\mathrm{mul}}^n} \tag{4.14}$$

Combining these leads to the energy dependent number of hadrons per generation

$$\frac{\Delta N_{\mathrm{H}}}{\Delta \log_{N_{\mathrm{mul}}}(E_0/E_{\mathrm{H}})}(E_{\mathrm{H}}) = \left(\frac{E_{\mathrm{H}}}{E_0}\right)^{-\kappa} \quad \text{with } \kappa := 1 + \log_{N_{\mathrm{mul}}} \frac{2}{3} \tag{4.15}$$

and to the hadronic spectrum

$$\frac{\mathrm{d}N_{\mathrm{H}}}{\mathrm{d}E_{\mathrm{H}}}(E_{\mathrm{H}}) = -\frac{\ln N_{\mathrm{mul}}}{E_0} \left(\frac{E_{\mathrm{H}}}{E_0}\right)^{-(\kappa+1)}. \tag{4.16}$$

Next we consider different types of hadrons h. In the following, we will keep using H if a variable is meant for all hadrons. We neglect the different reaction channels for different hadrons and assume a constant branching ratio B_{h} for production of a hadron type h, independent of the incident type, mainly focusing on pions and kaons.

The muon flux can now be derived by multiplying the hadron flux by the decay probability $P_{\mathrm{h}\to\mu}$ and folding it with the energy distribution of the generated muon $\frac{\mathrm{d}n_{\mathrm{h}}}{\mathrm{d}E_\mu}(E_\mu, E_{\mathrm{h}})$:

$$\frac{\mathrm{d}N_\mu}{\mathrm{d}E_\mu}(E_\mu) = \sum_{\mathrm{h}} B_{\mathrm{h}} \int_0^\infty \frac{\mathrm{d}n_{\mathrm{h}}}{\mathrm{d}E_\mu}(E_\mu, E_{\mathrm{h}})\, P_{\mathrm{h}\to\mu} \frac{\mathrm{d}N_{\mathrm{H}}}{\mathrm{d}E_{\mathrm{H}}}(E_{\mathrm{h}})\, \mathrm{d}E_{\mathrm{h}} \tag{4.17}$$

The probability of a decay into muons is the fraction of generated muons N_μ over the number of hadron N_h:

$$P_{\mathrm{h}\to\mu} := \frac{N_\mu}{N_{\mathrm{h}}} \tag{4.18}$$

The number of muons is given by

$$N_\mu = -\int_0^\infty \frac{b_{\mathrm{h}\to\mu}}{\lambda_{\mathrm{D}}} N_{\mathrm{h}}(x)\mathrm{d}x, \tag{4.19}$$

where $N_{\mathrm{h}}(x)$ is the number of hadrons at the propagation length x, that did not yet interact

or decay, $b_{\mathrm{h}\to\mu}$ is the branching ration for the decay into muons and $\lambda_{\mathrm{D}} = \frac{E_{\mathrm{h}}\tau_{\mathrm{h}}}{m_{\mathrm{h}}}$ is the decay length, assuming that the hadron energy E_{h} is large compared to its mass m_{h}. The lifetime of the hadrons is denoted by τ.

The number of hadrons $\mathrm{d}N_{\mathrm{h}}$ decaying or interacting per infinitesimal path-length $\mathrm{d}x$ is given by

$$\begin{aligned} \frac{\mathrm{d}N_{\mathrm{h}}}{\mathrm{d}x} &= -\left(\frac{1}{\lambda_{\mathrm{I}}} + \frac{1}{\lambda_{\mathrm{D}}}\right) N_{\mathrm{h}} = -\frac{1}{\Lambda} N_{\mathrm{h}} \\ &\text{with } \Lambda := \frac{1}{\lambda_{\mathrm{I}}} + \frac{1}{\lambda_{\mathrm{D}}}. \end{aligned} \tag{4.20}$$

Here λ_{I} is the interaction length of the hadron.

Combining Eq. (4.18), (4.19) and (4.20) yields the decay probability for decay into muons:

$$\begin{aligned} P_{\mathrm{h}\to\mu} = b_{\mathrm{h}\to\mu}\frac{\Lambda}{\lambda_{\mathrm{D}}} &= \frac{b_{\mathrm{h}\to\mu}}{1+\alpha_{\mathrm{h}}E_{\mathrm{h}}} \approx \frac{b_{\mathrm{h}\to\mu}}{\alpha_{\mathrm{h}}E_{\mathrm{h}}} \\ &\text{with } \alpha_{\mathrm{h}} := \frac{\tau_{\mathrm{h}}}{m_{\mathrm{h}}\lambda_{\mathrm{I}}}. \end{aligned} \tag{4.21}$$

This approximation holds for $\alpha_{\mathrm{h}}E_{\mathrm{h}} \gg 1$. The probability to create a muon of energy E_μ from the decay of a hadron with energy E_{h} is given by the energy distribution $\frac{\mathrm{d}n_{\mathrm{h}}}{\mathrm{d}E_\mu}(E_\mu, E_{\mathrm{h}})$. Unpolarized mesons undergoing a two-body decay generate mono-energetic muons isotropic distributed in their rest-frame (see T. Gaiser[Gai90]). In the laboratory system this corresponds to a flat distribution between the minimum energy $r_{\mathrm{h}}E_{\mathrm{h}}$ with $r_{\mathrm{h}} = \frac{m_\mu^2}{m_{\mathrm{h}}^2}$ and the maximum energy E_{h}:

$$\frac{\mathrm{d}n_{\mathrm{h}}}{\mathrm{d}E_\mu}(E_\mu, E_{\mathrm{h}}) = \begin{cases} \frac{1}{(1-r_{\mathrm{h}})E_{\mathrm{h}}} & r_{\mathrm{h}}E_{\mathrm{h}} \le E_\mu \le E_{\mathrm{h}} \\ 0 & \text{otherwise} \end{cases} \tag{4.22}$$

Applying Eqs. (4.16), (4.21) and (4.22) on Eq. (4.17) one obtains the muon flux

$$\begin{aligned} \frac{\mathrm{d}N_\mu}{\mathrm{d}E_\mu}(E_\mu) &= A\left(\frac{E_0}{\mathrm{GeV}}\right)^{\kappa}\left(\frac{E_\mu}{\mathrm{GeV}}\right)^{-(\kappa+2)} \\ \text{with } A &= \frac{\ln N_{\mathrm{mul}}}{\kappa+2}\left(\sum_{\mathrm{h}} B_{\mathrm{h}}\frac{b_{\mathrm{h}\to\mu}}{\alpha_{\mathrm{h}}}\frac{1-r_{\mathrm{h}}^{\kappa+2}}{1-r_{\mathrm{h}}}\right)\frac{1}{\mathrm{GeV}^2}. \end{aligned} \tag{4.23}$$

This results in the numerical values for the amplitude $A = 26.3 \cdot 10^{-3}\,\mathrm{GeV}^{-1}$ and for the exponent, according to Eq. (4.15), $\kappa = 0.824$. The values used for pions and kaons are summarized in Tab. 4.1. The values from this simple model will now be compared to the results of a detailed simulation.

4.3.2 Detailed Simulations

For simulation we used a modified version of CORSIKA based on the official version 6.2040 which enables shower simulation in salt water (see Acorne Collaboration[TDP+07]). Interac-

Table 4.1: Used numerical values for pions and kaons. Their contribution A to the amplitude as well as the full amplitude are provided.

h	B_h	$b_{h\to\mu}$	α	r_h	A_h [GeV^{-1}]
π	0.9	1.00	67.1	$5.73 \cdot 10^{-1}$	$20.03 \cdot 10^{-3}$
K	0.1	0.64	9.03	$4.58 \cdot 10^{-2}$	$6.00 \cdot 10^{-3}$
			$A = \sum_h A_h$:		$26.30 \cdot 10^{-3}$

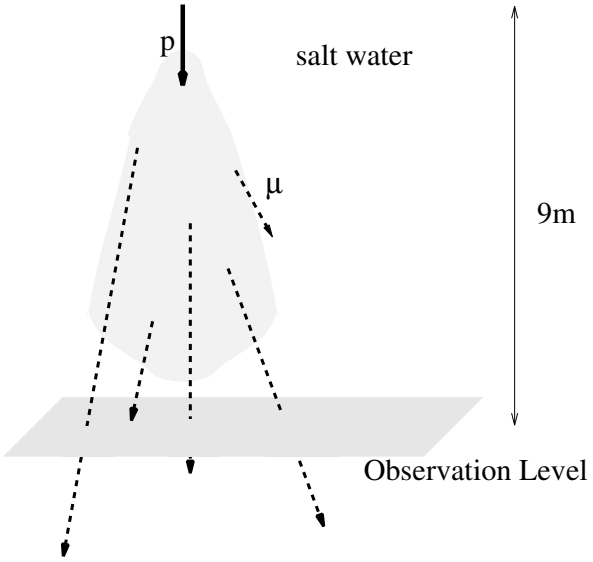

Figure 4.1: CORSIKA configuration: the incoming proton p interacts 9 m above the observation level. The produced muon μ will have roughly the same direction as the incoming particle and is recorded as it passes through the observation level.

tion models used are Gheisha for energies below 80 GeV in the laboratory system and and QGSJet 01 for higher energies. We simulated 1000 showers at primary energy $E_0 = 1$ TeV, 1000 at 10 TeV, 100 at 100 TeV and ten at 1 PeV with protons as primary particles.

The configuration used (Fig. 4.1) is a CORSIKA observation level 9 m behind the interaction point. Here the shower is expected to be fully developed, while only the very low energy muons will already have decayed.

4.3.3 Derived Muon Flux

The simulation measures the muon flux at the observation level. Most muons will be created before this. They lose some of their energy during the propagation. This energy loss can be approximated by

$$\frac{1}{\varrho}\frac{\mathrm{d}E_\mu}{\mathrm{d}x} = -a - bE_\mu, \tag{4.24}$$

where the medium density is $\varrho = 1.02\,\mathrm{g\,cm^{-3}}$ and the interaction constants are $a = 2.68\,\mathrm{MeV cm^2\,g^{-1}}$ and $b = 4.7 \cdot 10^{-6}\,\mathrm{cm^2\,g^{-1}}$ (see Particle Data Booklet[Par06]).

For further use the energy spectrum of muons at generation is of interest. Therefore we use the simplification that all muons are generated about five interaction lengths after the first interaction point. This corresponds to a distance of $x = 7\,\mathrm{m}$ that the muons propagate from generation point to the observation level. With this assumption the muon energy at generation can be estimated as

$$E_\mu = \left(E_\mu^{\mathrm{obs}} + \frac{a}{b}\right) \mathrm{e}^{\varrho b x} - \frac{a}{b}, \tag{4.25}$$

where E_μ^{obs} is the energy at the observation level. However, this is a small correction, important only for low energetic muons (in the hundred MeV region). Muons that are most interesting for us are those with track lengths above about 10 m, namely those with a range bigger than the typical shower size. These muons have energies above $\sim 2\,\mathrm{GeV}$, which is high enough to reduce systematic errors due to the energy correction.

Fig. 4.2 shows the normalized flux $\frac{E_\mu^2}{E_0}\frac{\mathrm{d}N_\mu}{\mathrm{d}E_\mu}(E_\mu)$ which follows a power law with small primary energy dependence in agreement with Eq. (4.23). We chose an energy range $0.6 \leq \log_{10}\frac{E_\mu}{\mathrm{GeV}} < 1.6$, for the region with good statistics. Here we perform a fit in the double logarithmic space, incorporating the primary energy dependency, on all data points simultaneously. As free parameters we use A and κ. The resulting parameterization is then:

$$\begin{aligned} \frac{\mathrm{d}N_\mu}{\mathrm{d}E_\mu} &= A \left(\frac{E_0}{\mathrm{GeV}}\right)^{\kappa} \left(\frac{E_\mu}{\mathrm{GeV}}\right)^{-(2+\kappa)} \\ A &= (10.0 \pm 1.0\,(\mathrm{stat}) \pm {}^{1.2}_{0.8}\,(\mathrm{sys})) \cdot 10^{-3}\,\frac{1}{\mathrm{GeV}} \\ \kappa &= 0.865 \pm 0.011\,(\mathrm{stat}) \pm 0.013\,(\mathrm{sys}). \end{aligned} \tag{4.26}$$

The systematic uncertainties were estimated by using different propagation distances for the energy correction as well as different energy ranges. In the analytic model describing the muon production in hadronic cascades, the amplitude scales linearly with the medium density ϱ and the primary energy E_o^κ. This is an effect of approximately 10 % in amplitude for changing from salt water to ice.

Using the integral representation (Fig. 4.3), we can see that on average a hadronic cascade of 100 TeV produces about one muon with an energy above 10 GeV. Solving Eq. (4.24), one estimates an average track length of about 36 m for such a muon.

CORSIKA provides the information if a muon was generated from a pion. Using this information, Fig. 4.4 shows the fraction of pion-produced muons over all muons as a function of the energy. As expected, other production mechanisms (e. g. kaons) become more important with higher energy. However, the constant hadron fractions B_h are a reasonable approximation. Our simple model with only pions and kaons ($B_K = 0.1$) predicts a constant ratio $\frac{N_\mu^\pi}{N_\mu} = 77\,\%$. The muon production following the parameterization described here is incorporated in the CMC module modeling cascades in the simulation process.

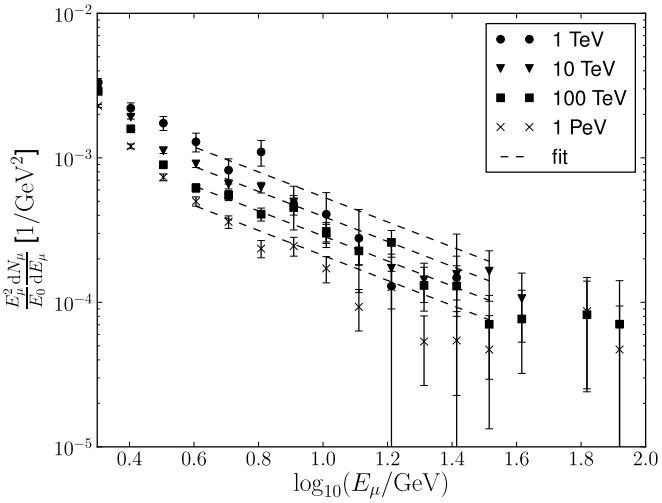

Figure 4.2: The muon flux $\mathrm{d}N_\mu/\mathrm{d}E_\mu$ as a function of muon energy E_μ for different cascade energies. It is multiplied by E_μ^2/E_0 to remove the primary energy dependence somewhat and to improve readability. The results of the simultaneous fit are given in Eq. (4.26).

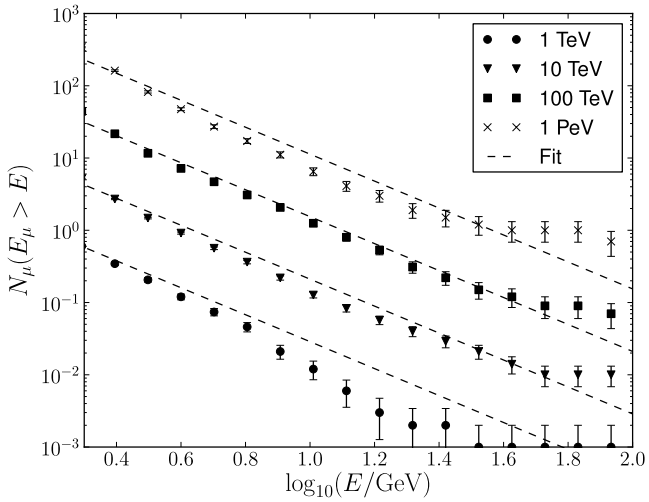

Figure 4.3: Integral muon flux $N_\mu(E_\mu > E)$. The fit is taken from the differential muon flux (see Fig. 4.2).

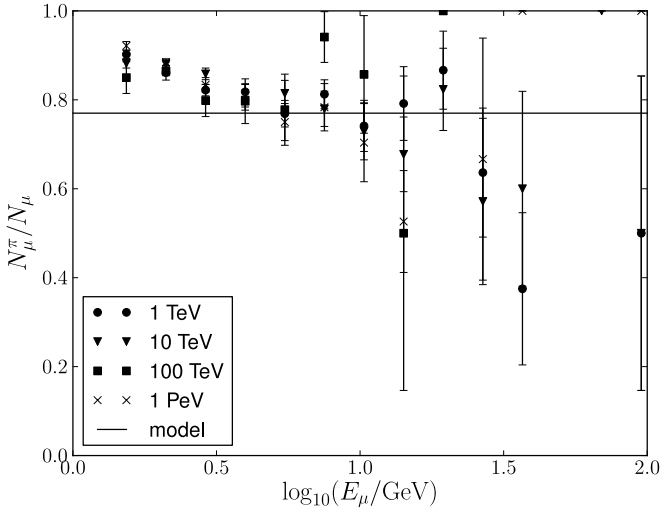

Figure 4.4: Muon parent: the ratio of number of muons produced by pions N_μ^π over all muons N_μ against muon energy E_μ is shown. A slight increase with energy of muons produced by other parent hadrons can be observed. However, comparison to the analytic model shows that the constant fraction (straight line) is a reasonable approximation.

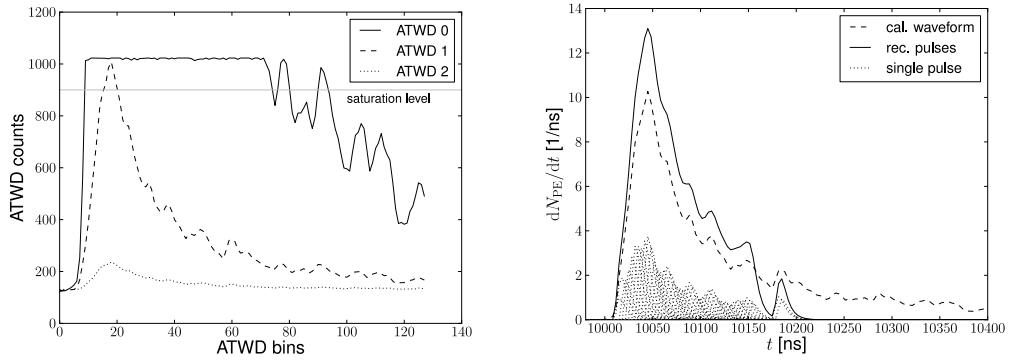

Figure 4.5: Feature extraction from recorded ATWD waveforms: The ATWD channels have different gains and as such saturates at different incoming signal (left). In the first step the records are combined and baseline and electronic effects are corrected. The ATWD counts are converted to charges (right, dashed line). With Bayesian unfolding pulses are extracted (dotted lines), that summed up (solid line) have the same charge as the raw waveform.

4.4 Reconstruction Algorithms

This section describes the different reconstruction algorithms used for this thesis. It starts with a description of the feature extraction, i. e. the reconstruction of the measured photons from the recorded charge. Then simple reconstruction algorithms, so called first guess algorithms are described. In Sec. 4.4.6 the likelihood method and the used likelihood reconstructions are explained. From Sec. 4.4.7 to Sec. 4.4.9 several variables based on a reconstructed cascades are described and finally this section is closed with a description of the BDT, the machine learning technique used for this thesis.

4.4.1 Feature Extraction

One of the first steps of the reconstruction is to evaluate the information from the recorded waveforms: to extract the times, charges and widths of PMT pulses. The DOM records three ATWD channels at different gains and one fADC channel with a coarser binning (compare Sec. 3.1.2). The first step is to combine the ATWD channels by taking in each bin the value from the ATWD channel with the highest gain, that is not saturated, i. e. has less than 900 ADC counts. Then ADC counts are converted into voltages.[Rou07] Corrections for known effects of the electronics as base-line and the transformer droop and the transit time are taken into account. Finally, a Bayesian unfolding with a standard pulse form is applied on the calibrated ATWD waveform.[Chi] Pulses in the fADC calibrated waveform are found when the recorded value is above a given threshold and pulses from ATWD and fADC are then combined. This was only used for the early analysis levels of this work, at higher levels only pulses from the ATWD were used. The steps of extracting pulses from the raw ATWD channels are shown in Fig. 4.5.

4.4.2 Line Fit

Line Fit[Lan] is a simple first guess algorithm for track reconstructions. Light is assumed to be emitted in a plane perpendicular to the track neglecting the Cherenkov geometry. The position of the plane at time t is given by the origin $\boldsymbol{r}$ and the velocity $\boldsymbol{v}$ as $\boldsymbol{r} + t\boldsymbol{v}$. One then calculates the χ^2 between data positions $\boldsymbol{r}_i$ at times t_i (i is the index of the measured pulse) and the plane position at t_i:

$$\chi^2 = \sum_i (\boldsymbol{r} + t_i\boldsymbol{v} - \boldsymbol{r}_i)^2 \,. \tag{4.27}$$

The minimum can be found analytically, resulting in

$$\boldsymbol{v} = \frac{\langle \boldsymbol{r}_i t_i \rangle_i - \langle \boldsymbol{r}_i \rangle_i \langle t_i \rangle_i}{\left\langle t_i^2 \right\rangle_i - \langle t_i \rangle_i^2}, \tag{4.28}$$

$$\boldsymbol{r} = \langle \boldsymbol{r}_i \rangle_i - \boldsymbol{v} \langle t_i \rangle_i \,. \tag{4.29}$$

Here $\langle \cdot \rangle_i$ denotes the average over i. It was shown by E. Middell and S. Panknin[MP09] that the algorithm has the best signal/background discrimination if the actual measured charge is not taken into account, however it could be simply included in the average as a weighting term. Although it is the simplest track reconstruction used here, it is also the only one that estimates a velocity for the particle, which proves as a helpful variable (see Sec. 5.2.1).

4.4.3 Dipole Fit

The Dipole Fit[LT] is a track reconstruction based on the idea of calculating a dipole moment to determine the direction. Let the position of hit DOM $\boldsymbol{r}_i$ with $i \in \{1 \ldots N\}$ be ordered by arrival time. Then the "dipole moment" is calculated as

$$\boldsymbol{M} = \frac{1}{N} \sum_{i=1}^{\frac{N}{2}} \frac{\boldsymbol{r}^{i+\frac{N}{2}} - \boldsymbol{r}^i}{\left\| \boldsymbol{r}^{i+\frac{N}{2}} - \boldsymbol{r}^i \right\|}. \tag{4.30}$$

The direction of this vector is used as the direction of the reconstructed track. For this work only the vector itself was used as the absolute of the dipole moment is a criterion how much directed a light pattern is. So values close to one are expected for tracks while the directions in the summation averages out for a cascade-like event.

4.4.4 Tensor of Inertia

In the Tensor of Inertia reconstruction[Gru] the measured pulses are regarded as point masses, in an analogy to classical mechanics. The amplitude A_i of the i-th pulse is used as the mass. The timing is neglected. This allows it to calculate the center of gravity (COG) as

$$\boldsymbol{r} = \sum_i A_i \boldsymbol{r_i} \tag{4.31}$$

where $\boldsymbol{r}_i$ is the position of the measured pulse. The tensor of inertia is then calculated as

$$I^{k,\ell} = \sum_i A_i \left(\delta^{k,\ell} \boldsymbol{r_i}^2 - r_i^k r_i^\ell \right) \tag{4.32}$$

where k, ℓ are the indices of the tensor and the position vectors and $\delta^{k,\ell}$ denotes the Kronecker symbol. The direction belonging to the smallest eigenvalue is used as the direction of the reconstructed track. The eigenvalue ratio, defined as the smallest eigenvalue over the sum of all eigenvalues,

$$q = \frac{I_1}{I_1 + I_2 + I_3} \quad \text{with eigenvalues } I_1 \leq I_2 \leq I_3, \tag{4.33}$$

provides a useful variable to distinguish spherical, i. e. cascade-like, events from more track-like ones: For a spherical hit pattern all eigenvalues have about the same value, while for a track-like pattern the smallest eigenvalue is close to zero.

4.4.5 CFirst

CFirst[Grea] is a seed for cascade likelihood reconstructions. Based on the center of gravity $\boldsymbol{r} = \langle r_i \rangle_i$ the starting time of the cascade is estimated: For a given pulse i at position $\boldsymbol{r}_i$ and time t_i and a guess of the starting time t the residual time τ_i is given by

$$\tau_i(t) = t_i - \left(t + \frac{d_i}{c_{\text{ice}}} \right) \quad \text{with } d_i = \|\boldsymbol{r}_i - \boldsymbol{r}\| . \tag{4.34}$$

A direct hit is then defined as a pulse with residual time $0 \leq \tau_i(t) \leq t_{\text{dir}} = 200\,\text{ns}$. The vertex time is then chosen as the smallest time with more than $N_{\text{req dir}} = 3$ direct hits in a sphere with a radius $R_{\text{dir}} = 100\,\text{m}$ around the COG. If no such time exists, the smallest hit time within a sphere of radius $R = 1\,000\,\text{m}$ around the COG is used.

4.4.6 Likelihood Reconstructions

The reconstruction of some physical process from the measured data can be done by optimizing some quality criterion. The criterion optimally using the information available in the measured data is the likelihood value.[Edw92] Let events to reconstruct be parameterized with $d \in \mathbb{N}$ parameters $\boldsymbol{c} \in \mathbb{R}^d$ and the measured points be $D \in \mathbb{N}$ variables $\boldsymbol{d} \in \mathbb{R}^D$. The probability $\text{p}(\boldsymbol{d}|\boldsymbol{c})$ of measuring $\boldsymbol{d}$, if the event has the parameters $\boldsymbol{c}$ is assumed to be known. The likelihood that the measured data $\boldsymbol{d}$ are caused by an event with parameters $\boldsymbol{c}$ is now defined as

$$L(\boldsymbol{c}|\boldsymbol{d}) := k\text{p}(\boldsymbol{d}|\boldsymbol{c}), \tag{4.35}$$

where $k \in \mathbb{R}^+$ is an arbitrary chosen value independent from $\boldsymbol{c}$.

We describe the measured light with Poisson statistics[BSMM01], i. e. the probability of measuring n events, when μ events are expected is

$$p(n|\mu) = \frac{\mu^n}{n!} \mathrm{e}^{-\mu}. \tag{4.36}$$

The data $\boldsymbol{d} = (n_{ot})_{\substack{o\in\text{DOMs},\\ t\in\text{bins}}}$ in this case is the measured number of photons n_{ot} in the DOM o and the time bin t. For an event with parameters $\boldsymbol{c}$ a prediction μ_{ot} is given. This leads to the likelihood

$$L(\boldsymbol{c}|\boldsymbol{d}) = \prod_{\substack{o\in\text{hit}\\ \text{DOMs}}} \prod_{t\in\text{bins}} \frac{\mu_{ot}^{n_{ot}}}{n_{ot}!} \mathrm{e}^{-\mu_{ot}} \prod_{\substack{o\in\text{unhit}\\ \text{DOMs}}} \mathrm{e}^{-\mu_o}, \tag{4.37}$$

where $\mu_o = \sum_{t\in\text{bins}} \mu_{ot}$.

To calculate the number of expected events, the light propagation has to be described. This can be done by a parameterization with a gamma distribution, the so called Pandel function[Pan96] for bulk ice. The delay time t_d is the time from the light emittance to its measurement t reduced by the time, the light would need on the shortest way between source and detector, t_dir:

$$t_\mathrm{d} := t - t_\mathrm{dir} \tag{4.38}$$

Then the delay time distribution for a distance r between source and detector is given by

$$\frac{\mathrm{d}P}{\mathrm{d}t}(t_\mathrm{d}, r) = \frac{a\,(at_\mathrm{d})^{b-1} \exp(at_\mathrm{d})}{\Gamma(b)} \tag{4.39}$$

$$a = \frac{1}{\tau} + \frac{c_\mathrm{ice}}{\ell_\mathrm{a}} \tag{4.40}$$

$$b = \frac{r}{\ell}. \tag{4.41}$$

Here the velocity of light in ice is denoted by c_ice, the constants $\tau = 450\,\mathrm{ns}$, $\ell = 47\,\mathrm{m}$ and $\ell_\mathrm{a} = 98\,\mathrm{m}$ are found in M. Kowalski[Kow03]. If the layered structure of the ice (see Sec. 3.2) is taken into account tabulated values obtained in a simulation of the propagation with the software photonics (comp. Sec. 4.1.3) can be used. For this work three implementations were used:

- Gulliver track likelihood[GBH08]: fit a track hypothesis to the data. Per DOM only the total charge and the time of the first hit is used. For estimation of the light propagation the Pandel function is used. Free parameters are position of one point of the track $\boldsymbol{r}$, the corresponding time t and direction (ϑ, φ).

- cascade likelihood[Greb]: As above but for a cascade hypothesis. The free parameters are vertex position $\boldsymbol{r}$ and the time t (energy and direction are not fitted).

- credo[Mid08]: uses the full pulse information to reconstruct a cascade hypothesis. Photonics tables are used so the ice properties are included. Vertex position $\boldsymbol{r}$ and time t but also direction (ϑ, φ) and energy E are fitted.

In these algorithms, the negative logarithm of the likelihood is minimized to find the optimal solution. A problem can be that a local minimum is found instead of the global one. To avoid this iterative minimization with different initial values can be used.

In addition, not only the reconstructed event is of interest but also the value of the likelihood function. In analogy to the χ^2 the reduced logarithmic likelihood is defined:

$$\text{RLLH} := -\frac{\log L}{f} \qquad \text{with } f = D - d \tag{4.42}$$

Small values are in best agreement with the hypothesis.

Another related algorithm, ACER[D'A09b], is used as a first energy reconstruction. It uses the time of the first hit and the amplitudes for each DOM and photonics to describe the light propagation. It gets vertex position and time by a previous reconstruction and only fits the energy. So finding the minimum is equivalent to finding the roots of the derivative of the likelihood function, what can be achieved numerically (in absence of noise an analytic solution is also possible).

4.4.7 Fill Ratio

The Fill Ratio module[Rutb] provides variables to estimate how spherical an event is in the detector. For a given vertex position $\boldsymbol{r}$ the mean $r^*_{\text{mean}} = \langle|\boldsymbol{r} - \boldsymbol{r}_i|\rangle_{i\in\text{hit OMs}}$ and the standard deviation[4] $r^*_{\text{RMS}} = \sigma_{i\in\text{hit OMs}}(\text{d}(\boldsymbol{r}, \boldsymbol{r}_i))$ of the distance between hit DOM and vertex is calculated. Each of these radii is scaled with a specific, constant factor[5] and a sphere of the radius $r_{\text{mean, RMS}} = k_{\text{mean, RMS}} r^*_{\text{mean,RMS}}$ around the vertex is considered. The fill ratio $q^{\text{fill}}_{\text{mean, RMS}}$ is then defined as the number of hit DOMs inside the sphere corresponding to the mean or the standard deviation over the number of all DOMs in the sphere. A spherical event, like a cascade, should thus result in fill ratios close to one, while track-like events, should only partially fill the sphere.

4.4.8 Reconstructions on Split Pulse Series

It is useful to do reconstruction on some of the pulses only to test the stability of the fit. For this two methods were applied: The time ordered pulses were split in two halves and cascade likelihood reconstructions (cscsd-llh and cfirst as seed) were performed on both of them.

Around the vertex $\boldsymbol{r}$ determined by credo with reconstructed energy E a sphere was placed and hits outside were removed.[Ruta] The radius r of the sphere was calculated by

$$r = kR_{\text{SPE}} = k \begin{cases} \ell_{\text{att}} \ln \frac{E}{\text{GeV}} + c & E > E_c \\ r_0 + a \ln^2 \frac{E}{\text{GeV}} & \text{otherwise,} \end{cases} \tag{4.43}$$

with the scaling parameter $k = 0.8$ and the parameterization for the distance R_{SPE} from the

[4] In the fill ratio documentation the standard deviation and the RMS are used synonymous, which is kept in the context of fill ratio.

[5] In this work $k_{\text{mean}} = 1.6$ and $k_{\text{RMS}} = 3.4$ were used, following a study on the best discrimination power[Rut09].

cascade, at which only one photo electron is expected. Here $E_c = 750\,\mathrm{GeV}$ denotes the critical energy, below which a second order approximation is done and a radius of at least $r_0 = 5\,\mathrm{m}$ is guaranteed. The attenuation length is $\ell_{\mathrm{att}} = 29\,\mathrm{m}$ and the other parameters are $a = \frac{\ell_{\mathrm{att}}}{2 \ln \frac{E_c}{\mathrm{GeV}}}$ and $c = r_0 - \frac{\ell_{\mathrm{att}}}{2} \ln \frac{E_c}{\mathrm{GeV}}$.

4.4.9 Containment

For this work, two containment variables were used: the depth of the highest hit $z_{\text{highest hit}}$ is the z-position of the highest hit DOM. The scale variable f_{scale} based on the vertex is the value by which the detector need to be scaled around its center, in order to have the vertex placed on the border. Values lower than one express that the event is contained, larger values correspond to events outside the detector. The algorithm for the calculation is based on Rawlins and Federova[RF,Raw]. The original implementation was done for tracks and was extended to be usable for cascades in this work.

4.4.10 Boosted Decision Trees

The boosted decision tree[HSS+07] is one technique to combine the value of several different variables into a single quality criterion. The BDT has to be "trained". For this background and signal data is used. The data is split with the variable, that has the best background to signal separation power, at the optimal cut position into two parts. The data in these parts is split again with the most powerful variable on this data region. This procedure is iterated on each part such that a decision tree forms. Each of the leaves contains either mostly signal or mostly background. So the event classification of a single tree i for an event $\boldsymbol{x}$ is then

$$h_i(\boldsymbol{x}) = \begin{cases} -1 & \text{ends up in a background leaf} \\ +1 & \text{ends up in a signal leaf} \end{cases} \tag{4.44}$$

The weights of the events that were misclassified by the decision tree are multiplied by a factor α_{i+1} (so-called boosted) and a new tree $i + 1$ is trained. This factor is calculated by the boosting algorithm (here AdaBoost was used, see Hoecker et al. [HSS+07] for details). With this procedure a "forest" of N decision trees is created.

To calculate the BDT score for an event one now counts, in how many trees the events ends up as signal and in how many it ends up as background. The trees are weighted by the same boosting factor α, with which the misidentified events were reweighted. The event classification is now given as

$$s_{\mathrm{BDT}}(\boldsymbol{x}) = \frac{1}{N} \sum_{i \in \text{forest}} \ln \alpha_i h_i(\boldsymbol{x}). \tag{4.45}$$

5 Cascade Analysis

The goal of the analysis is to find an extra-terrestrial neutrino utilizing neutrino induced cascades. Electron neutrinos generate cascades for both neutral and charged current interaction. Following the flux prediction discussed in Sec. 2.2 it is a natural choice, to optimize the analysis for an E^{-2} electron neutrino spectrum. Atmospheric muons and atmospheric neutrinos generated from pion and kaon decay are considered as background. A possible component of the atmospheric neutrino spectrum generated by mesons containing charm quarks is still undetected and as such considered as another interesting source of signal.

Due to the low number of expected signal events, it is crucial to avoid a bias from the experimenter. Therefore the analysis is performed in a blind manner (see Klein and Roodman[KR05]). The cut optimization of the analysis has been done on Monte Carlo simulations. Around 10 % of the measured data was used as "burn sample" to check and verify the simulation data and is not further used for the search.

In this chapter the data and analysis technique are described. The results, including the systematic uncertainty calculation, are discussed in Chapter 6.

5.1 Data Samples

The analysis uses data taken during 2008 and 2009 with the 40-string configuration of IceCube (see Sec. 3.1). Only data runs with all strings operational, the in-ice detector component running and having no known issues[1] are considered. These runs were selected from a data run summary[R+10] done by the collaboration. As a further quality criterion the rates after the off-line filtering (see Sec. 5.2.2) are used. It was found that the runs 111150, 113219 and 113241 had problems with the DAQ during data taking. Events were recorded multiple times, so that the runs were completely removed from the analysis. The rates of the remaining runs are consistent with each other and follow the seasonal variations (see Fig. 5.1). The runs 112764, 112763 and 111770 have already been lost at an early processing level[2] and were not included. It is observed, that there are gaps larger than half a minute between events. Such gaps made up less than 10 % of the run time in some few runs and in total less 0.05 % of the full time of data taking (see Fig. 5.2). However, this gaps were taken into account in the lifetime calculation. All runs with a run number ending with zero are used as a burn sample to compare background simulation to and are not further used in the later analysis. This has the advantage, that they are well distributed over the full measurement

[1] Common issues are e.g. very short runs (less than 10 min) and an artificial light source switched on in the detector, see[R+07]

[2] Likely some failed copying or writing step during a collaboration-wide processing. It was not found worth to recover this files.

time and thus include seasonal variations (see Sec. 6.2). This burn sample has a life time of 35 days, the remaining data has a life time of 332 days.

The Monte Carlo simulations used in this work are listed in Tab. 5.1. The "basic MC" is used for the cut optimization described in this chapter. As described in Sec. 4 single atmospheric muon events and double and triple coincident events were separately simulated. They are used together for the atmospheric muon prediction (μ^{atm}). As higher energetic events are a more important background for this analysis, the single muon simulation applies weights in order to over-sample higher energies (see Sec. 4.2). The neutrino data sets for electron, muon and tau neutrinos are generated with a E^{-1} flux. They were used for the signal estimation and the atmospheric neutrino prediction by reweighting. There is no well established flux normalization for the signal, however, it was desired to calculate event numbers, so that a comparison to background or between different stages of the analysis is possible. Therefore the E^{-2} signal flux was normalized with $\Phi_0 = 5 \cdot 10^{-7}\, E^{-2}\, \text{GeVs}^{-1}\,\text{sr}^{-1}\,\text{cm}^{-2}$, which corresponds to the limit for an all flavor neutrino flux found in a diffuse search in five years of AMANDA data.[3] [A+11e] For the conventional atmospheric neutrino flux ($\nu^{\text{atm}}_{e,\mu}$), i.e. the flux generated by pion and kaon decay, the Bartol model [BGL+04] was used for reweighting the electron and muon neutrino data sets. For a component of the neutrino flux generated by mesons containing charm quarks, the so called prompt flux ($\nu^{\text{prompt}}_{e,\mu}$) the model from Sarcevic [ERS08] was applied. Compare Sec. 2.2.2 for a description of the atmospheric neutrino fluxes. For neutrino cross sections CTEQ5 [L+00] was used for the main analysis. However, the only available tau neutrino data set uses CSS [CS08] neutrino cross sections (see Sec. 4.1.1 and 6.2). The standard ice model for all simulation data sets is AHA (see Sec. 3.2).

Separate single muon simulation and electron neutrino simulation was used for the BDT training (see Sec. 5.2.3). Systematic checks in Sec. 6.2 use MC with the SPICE1 ice model (see Sec. 3.2) instead of AHA, modified DOM efficiencies 10 % higher and lower than the nominal ones and CSS cross sections instead of CTEQ5.

The flusher runs 111739 and 111741 were used for a cross check of the analysis and are described in some detail in Sec. 6.1.

5.2 Event Selection

The detector measures data with an average trigger rate of 1 200 Hz. This results in $3 \cdot 10^{10}$ events collected in 332 days. Even with the optimistic flux normalization of $\Phi_0 = 5 \cdot 10^{-7}\, E^{-2}\, \text{GeVs}^{-1}\,\text{sr}^{-1}\,\text{cm}^{-2}$ only 2 800 events are expected to stem from signal. Three filter steps reduce the amount of data while keeping a high signal content:

- the pole filter, using fast algorithms for cut variables in order to reduce the data volume, such that the transfer over satellite is feasible,

- the offline filter, using fast cascade reconstruction and reduce the data volume such, that CPU intensive likelihood reconstruction can be applied on the remaining data

[3] Lower limits became lately available, see Sec. 6.3

Table 5.1: Used MC data sets: The data sets under "basic MC" are used for the optimization, two more data sets are taken for the BDT training and several more special MC data sets are used for the study of systematic uncertainties (see Sec. 6.2).

Type	Description	Data Sets	Files
μ_{single}	basic MC for analysis	2546, parts of 2712, 2907, 2975	140 000
μ_{double}		2110, 2483, 3813, 4497	20 000
μ_{triple}		2711, 4455, 4540	3 500
ν_e		3221	6 000
ν_μ		3311	8 000
ν_τ		5117	1 000
μ_{single}	used for BDT training	parts of 2712	20 000
ν_e		3170	10 000
μ_{single}	SPICE ice model	3404	3 000
ν_e	SPICE ice model	5044	800
ν_μ	90 % quantum efficiency	3264	1 000
ν_μ	110 % quantum efficiency	3265	1 000
ν_e	CSS neutrino cross section	5102	500

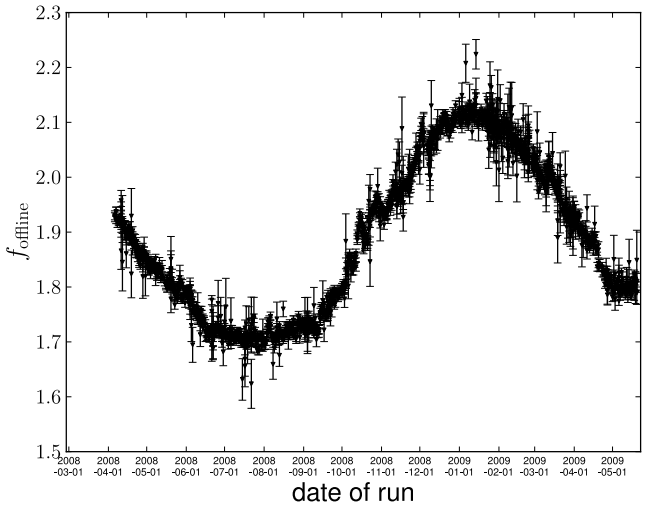

Figure 5.1: Rate after the first off-line filter: the rates of the selected runs are consistent with each other and follow the seasonal variation of the atmospheric muon rate (see Sec. 6.2.3).

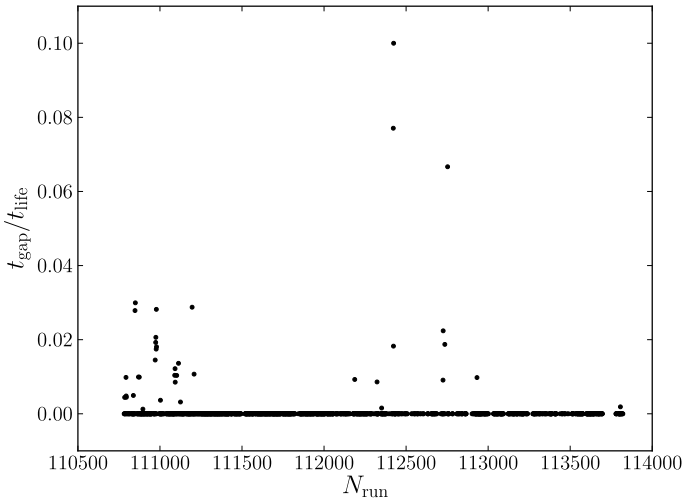

Figure 5.2: Time gaps: Only few runs show gaps larger than 30 s between events. This gaps are at maximum 10 % of the life time per run. The sum of the gaps is less than 0.05 % of the total life time of the used data.

- and the final level, in which the several variables are combined and together with a cut on the reconstructed energy are used to suppress the background down to the level needed for the analysis.

These steps are discussed in more detail in the following sections. An overview of the event numbers at the different filter levels is given in Tab. 5.2 and in Fig. 5.3 the numbers are compared to the corresponding analysis on the IC22 data sample[IAA+11].

5.2.1 Event Selection at the Pole

Data taking at the South Pole station is restricted by two important limitations: As kerosene is the only available power source and needs to be transported to the station by air plane the

Table 5.2: Signal and background event numbers for the different cut levels: The first reduction levels make the data stream manageable (transmission over satellite, calculation of time consuming reconstructions). The required reduction for the analysis is mainly done in the last level.

Level	$N_{\mu^{\mathrm{atm}}+\nu_{e,\mu}^{\mathrm{atm}}}$	$N_{\nu_e}^{\mathrm{astro}}$
Trigger Level	$3 \cdot 10^{10}$	2 800
Pole Filter	$4.6 \cdot 10^{8}$	1 900
Off-line Filter	$5.5 \cdot 10^{7}$	1 600
Final Level	0.72	55

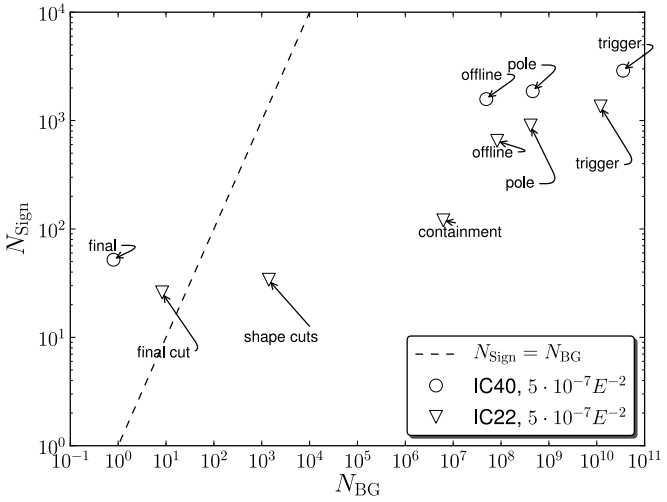

Figure 5.3: Signal and background event numbers for the different cut levels: The region left to the dashed line would contain more events of the hypothetical signal flux than background. The point indicate the signal and background expectation at different filter levels. The IC22 analysis[IAA+11] is shown as triangles, this work as dots.

available CPU power is limited. The second limitation is the restricted satellite band width needed for sending data to the north. So a first filter level using only simple reconstructions is needed to reduce the data volume.[4] For the cascade channel, one of several data taking channels, about 10 $\frac{\mathrm{GB}}{\mathrm{d}}$ satellite bandwidth were available in 2008. This corresponds roughly to 16 Hz data rate, about 1.3 % of the background. To achieve the data reduction direct cuts on the velocity of the Line Fit reconstruction (see Sec. 4.4.2 and Fig. 5.4) and the eigenvalue ratio of the tensor of inertia module (see Sec. 4.4.4 and Fig. 5.5) were performed. These variables use the spherical hit pattern generated by signal events in contrast to the hit pattern following a track caused by background events to separate the two classes: The Line Fit algorithm assigns velocity to the reconstructed track. For background, that is caused by a muon, the distribution peaks at the velocity of light, as expected. Lower and higher values are caused due to the fact, that the description used in the line fit algorithm does not take the Cherenkov geometry into account. Signal events have essentially no direction of motion, so that the velocity peaks at lower values. The eigenvalue ratio of the tensor of inertia for a massive sphere is $\frac{1}{3}$, while the value for an infinite thin pole is zero. Therefore spherical, cascade-like events have eigenvalue ratios close to one third, while track-like events have values close to zero.

However, one string events caused by a cascade have an eigenvalue ratio of zero and are thus removed. This allows us, to estimate the minimal energy of cascades passing this filter:

[4] This section is a summary of the study for the pole filter described in S. Panknin[Pan08].

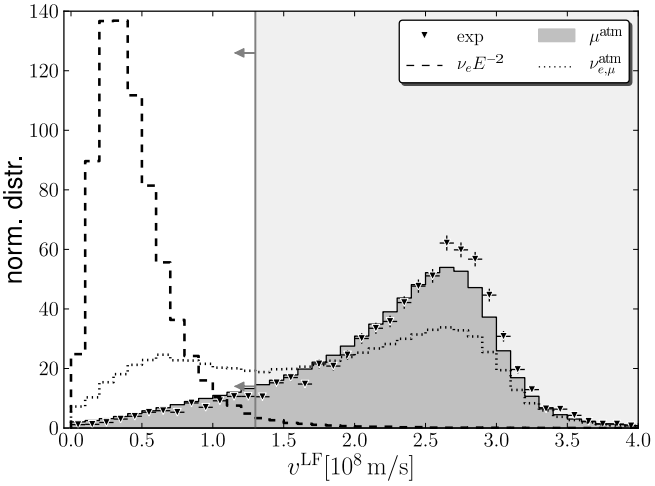

Figure 5.4: Line Fit velocity: Cascades are get a low velocity assigned, wile this value is high for muons. Note that the atmospheric neutrinos split into this two groups due to the charged current interaction of the muon neutrinos. To pass the online filter the velocity has to be below $1.3 \cdot 10^8\,\frac{\mathrm{m}}{\mathrm{s}}$.

The radius, at which a single photo electron is expected, can be estimated by

$$r = \ell_{\mathrm{att}} \ln \frac{E}{\mathrm{GeV}} + c, \tag{5.1}$$

where $\ell_{\mathrm{att}} \approx 29\,\mathrm{m}$ and $c \approx 93\,\mathrm{m}$.[Kow03] For a distance of 125 m, the string spacing, this requires an energy of 1 T*e*V.

The cut values used are

$$v^{\mathrm{LF}} > 1.3 \cdot 10^8\,\frac{\mathrm{m}}{\mathrm{s}} \quad \wedge \quad q^{\mathrm{ToI}} > 0.12 \tag{5.2}$$

This results in 70 % of the triggered signal at a background rate of 16 Hz.

A programming error was found in the feature extraction used at the pole. This error generated pulses without any correspondence in the measured data, but it did not affect simulation data, so that the influence on signal could not be estimated. As the cascade stream may have accidentally lost signal it was decided to include date from other streams into the analysis and reevaluate the pole filter with a corrected feature extraction. The streams used are:

- the cascade stream, reevaluated to remove undesirably taken background,
- the muon stream[HL08] as the largest data stream
- and the EHE stream[Ish08] designed for large energies and thus ensuring that possible high energetic signal events are included in the analysis.

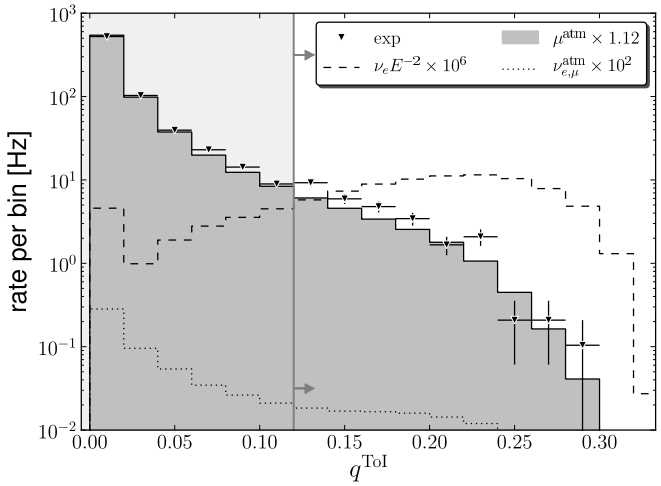

Figure 5.5: Eigenvalue ratio of tensor of inertia: Spherical cascades have higher values, than track-like events. The peak at zero for the signal spectrum is caused by low-energetic one string events. To pass the pole filter a value above 0.12 is required.

5.2.2 First Off-line Event Selection

In the next step the cscd-llh likelihood reconstruction together with the ACER energy reconstruction and a non-iterative track-fit (see Sec. 4.4.6) are applied to the data. As the background rate for high energetic events is sufficiently low (see Fig. 5.8), all events with a reconstructed energy above 10 TeV are kept for the next analysis level. For lower energies a further background reduction is needed: A cut on the reduced logarithmic likelihood value of the cascade reconstruction and on the zenith angle of the track reconstruction were used. The reduced negative logarithmic likelihood is small for values well in agreement with a cascade hypothesis (see. Fig. 5.6). The zenith reconstruction uses the fact, that most background events are reconstructed as downward-going tracks, while cascades are mostly reconstructed horizontally due to the denser z-spacing of the DOMs (see Fig. 5.7). The cuts used are

$$\left(-\frac{\log L^{\text{cscd-llh}}}{f^{\text{cscd-llh}}} < 10 \quad \wedge \quad \cos\theta_\mu < 0.174\right) \quad \vee \quad E^{\text{ACER}} > 10\,\text{T}e\text{V}. \tag{5.3}$$

This results in an average background rate of 1.9 Hz while 80 % of the E^{-2} signal from the previous cut level are still remaining. After this level an iterative muon reconstruction and the credo cascade reconstruction were applied to the data.

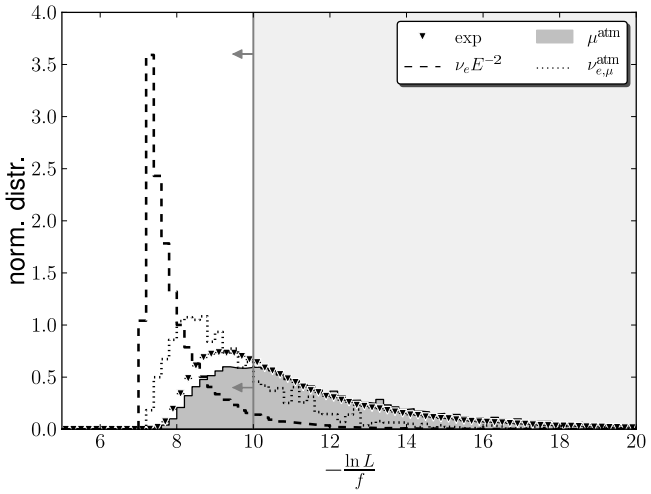

Figure 5.6: Reduced logarithmic likelihood of the cscd-llh reconstruction: Low values correspond to events well in agreement with a cascade hypothesis. So signal peaks at low values and pass the cut at 10, while half of the background achieves higher values.

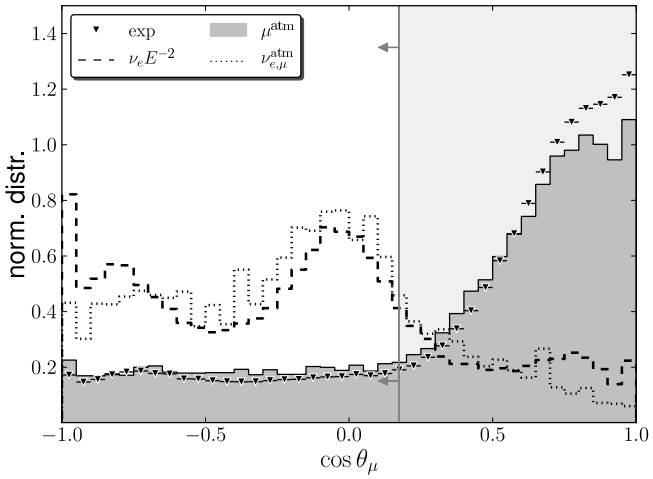

Figure 5.7: Zenith of the non-iterative track reconstruction: Cascades are reconstructed due to the higher spacing in z mostly as horizontal events, while tracks are mostly reconstructed as downward going.

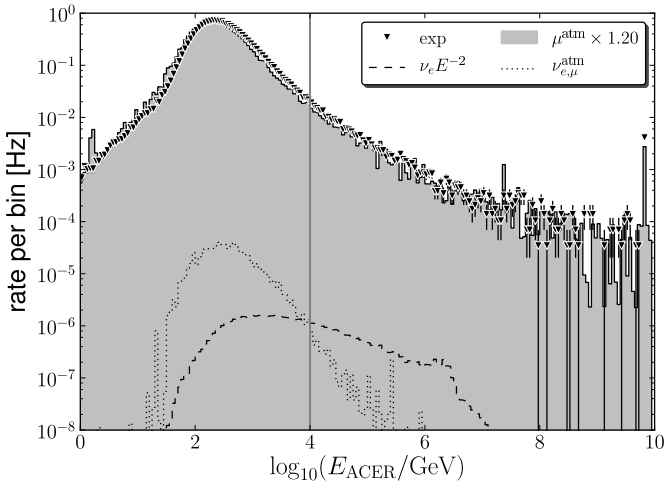

Figure 5.8: ACER Energy spectrum: Background peaks around 300 G*e*V and falls of steeply, while signal still has a reasonable contribution above 10 T*e*V. So all events above 10 T*e*V are passing the offline filter, while lower energetic events also need to pass the likelihood and the zenith cut.

5.2.3 Final Level

After the off-line filter the sample still contains 27 % coincident events. These can be efficiently rejected by a cut on the fill ratio variable based on the mean distance of the hit DOMs to the vertex (see Sec. 4.4.7 and Fig. 5.13). The cut is

$$q_{\mathrm{fill}}^{\mathrm{mean}} > 0.2. \tag{5.4}$$

This variable as well as the variables used before, shows some discrepancy in the measured distribution compared to the MC prediction. This is due to the systematic uncertainties, for example with the ice model, DOM efficiencies and cosmic ray composition. As no other MC with a better agreement is available, this analysis needs to overcome this problem. Cuts on variables suffering from data/MC mismatch are responsible for an increasing difference between measured rate and the predicted rate from MC. A full discussion of the rate mismatch including an estimate of the resulting systematic uncertainties is given in Sec. 6.2. After the cut on the fill ratio variable the rate from experimental data is found to be 1.73 times higher than the prediction from the simulation. The simulated rate was scaled with this factor. This was necessary, because the final optimization needed a reasonable rate prediction. Then ten variables, listed in Tab. 5.3, are used for training a BDT (see Sec. 4.4.10). The variables were chosen to have a weak energy dependency and low correlation between each other (see Tab. 5.4).

Table 5.3: Variables for BDT training in the final level: The used symbol is followed by a short explanation of the expected signal and background behavior and by the reference to the description of the algorithm and a figure showing the distribution of the variable. The first seven variables are sensitive to the signature of the event, the last three are quality of the fit and position variables.

Symbol	Explanation	Alg.	Fig.
$\cos\theta_{\mu,32}$	cosine of the zenith angle of the 32-fold track reconstruction; most background is reconstructed down-going, while due to the smaller z-spacing signal is reconstructed horizontal.	4.4.6	5.9
δt	time difference of the cascade reconstruction on the first and the second half of the time ordered pulses; this is close to zero for signal that will be reconstruct in both cases as a similar event, but larger for track-like background.	4.4.8	5.10
δz	as above but the z-distance, showing similar behavior, with smaller values for the down-going tracks of the background.	4.4.8	5.11
M	absolute of the dipole moment; small values for a spherical event and values closer to one for background.	4.4.3	5.12
$q_{\text{fill}}^{\text{mean}}$	fill ratio based on mean; close to one for signal but small for track-like background.	4.4.7	5.13
$q_{\text{fill}}^{\text{RMS}}$	fill ratio based on standard derivation; behaves as above	4.4.7	5.14
q^{TOI}	eigenvalue ratio of tensor of inertia; spherical signal results in values close to $\frac{1}{3}$ while track-like background has values close to zero; was already used for the pole filter (comp. Sec. 5.2.1)	4.4.4	5.15
δz^{core}	z-distance of cascade reconstruction on all pulses and on the inner core only; this is more a general fit stability criterion.	4.4.8	5.16
f_{scale}	scale factor; basically a position criterion, misidentified tracks are more common at the border of the detector	4.4.9	5.17
$z_{\text{highest hit}}$	highest hit z-position; position criterion, background coming from above can trigger the highest DOMs	4.4.9	5.18

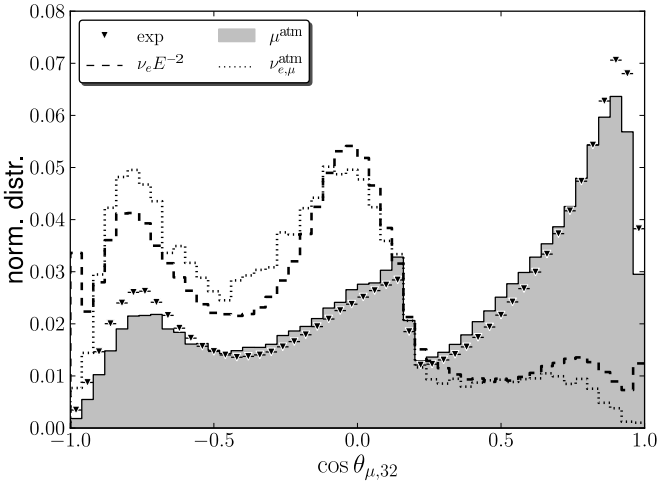

Figure 5.9: Zenith angle of the 32 iterative track reconstruction: Most of the background events reconstruct as upward going tracks, while signal is reconstructed horizontally or even upward going, due to the direction less signature and the denser z-spacing. (See also Sec. 4.4.6)

Similar to the previous level, the zenith angle of the muon reconstruction $\theta_{\mu,32}$ is used. Here the simple track reconstruction is replaced by an 32-fold iterative one (see Sec. 4.4.6). The previous cut remains clearly visible in Fig. 5.9. Events above the cut, pass the previous filter due to a high reconstructed energy or were differently reconstructed by the previous reconstruction. The muon background peaks at values close to one, while the signal is reconstructed at values close to zero or at ±0.7. Due to the denser DOM spacing along the z-axis horizontal muons fit best to the light pattern of a cascade. However, the muon fit does not take the dust layers into account. If the spherical pattern is deformed by such a layer, a zenith angle of ±0.7 is preferred, which corresponds well to the Cherenkov angle. A further, fainter peak for signal is directly upward or downward going. The atmospheric and the E^{-2} neutrino flux show very similar distributions, illustrating the low correlation between energy and this variable (11 % for signal). The agreement between data and background is reasonable for this variables. The worst region is a 20 % underestimation of the background in the region around 0.7.

As explained in Sec. 4.4.8 useful variables can be constructed, if the time ordered pulses are split in two halves. Here a cascade likelihood reconstruction is performed on both halves. For the reconstructed time and z-position the difference of first minus second reconstructed value, δt and δz is used as a variable for the BDT training. The distributions are provided in Fig. 5.10 and Fig. 5.11. The idea of the variable is, that the reconstructed values for a real cascade are only slightly effected by this split. So both distributions peak around zero for signal. For background muons coming from above, the reconstruction will likely result in an earlier cascade at shallower z-position and a later, deeper cascade. Therefore

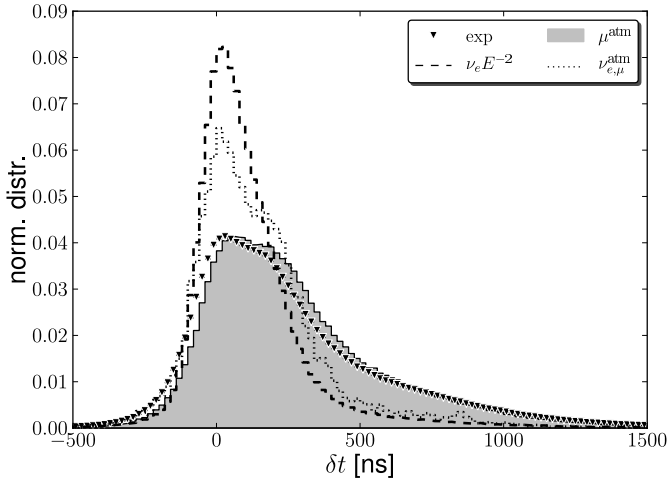

Figure 5.10: Difference in reconstructed interaction time performed on the first respectively second half of the time ordered pulses. For signal both reconstructions yield about the same interaction time, so that the distribution peaks at zero, while background events are reconstructed to earlier times in the first half of the pulses, so that a higher values of δt is found. (See also Sec. 4.4.8)

both background distributions are broader and the δt distribution is shifted towards higher values and the δz distribution towards lower. This effect is slightly stronger in MC than in measured data.

A variable using directly the properties of the spherical signature is the dipole moment (see Sec. 4.4.3). For a track lines through pairs of hit DOMs should be all aligned with the direction of the track, while there is no preferred direction for a cascade. So the absolute of the dipole moment peaks at lower values for cascades and at higher values for background (see Fig. 5.12). The measured data is slightly shifted to lower values, but shows reasonable agreement to the simulation. For atmospheric neutrinos the distribution is very similar to the distribution for atmospheric muons. This indicates, that the variable performs worse for lower energy events. However, no strong correlation with energy is observed (around 10 %).

As was discussed before, a variable especially useful for removing coincident events is the fill ratio. For that reason a cut of $q_{\mathrm{fill}}^{\mathrm{mean}} > 0.2$ was perform before the training. The distribution is given in Fig. 5.13. The fill ratio q_{fill} calculates the ratio of hit DOM over all DOMs in a sphere. The radius of the sphere can be calculated using the mean distance of hit DOMs to a reconstructed vertex or the standard derivation (compare Sec. 4.4.7). Track-like background events do not fill this sphere very well, in contrast to round cascades. Events from coincident muons peak at even lower values compared to the single muon background in at $q_{\mathrm{fill}}^{\mathrm{mean}} = 0.04$ and are thus removed by the cleaning cut. As the remaining distribution still shows discriminating power it was included into the BDT training. It has to be mentioned that the data/MC agreement in this variable is especially bad in the cut region:

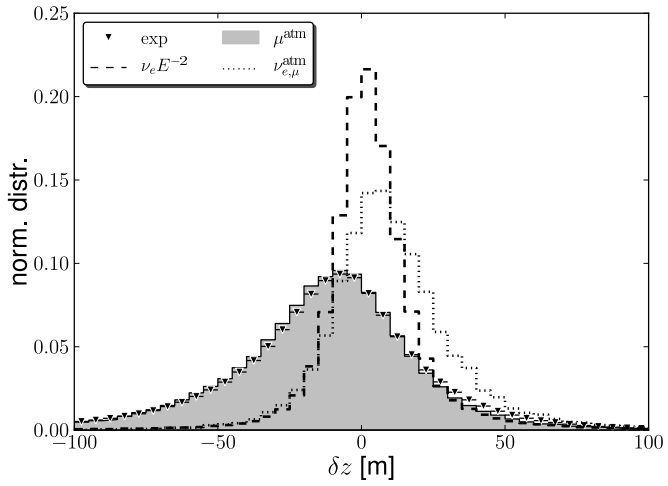

Figure 5.11: Differences in the reconstructed cascade z-position of the split pulse series: As for the time difference, the signal is stable and peaks around zero, while (down-going) tracks produce smaller values. (See also Sec. 4.4.8)

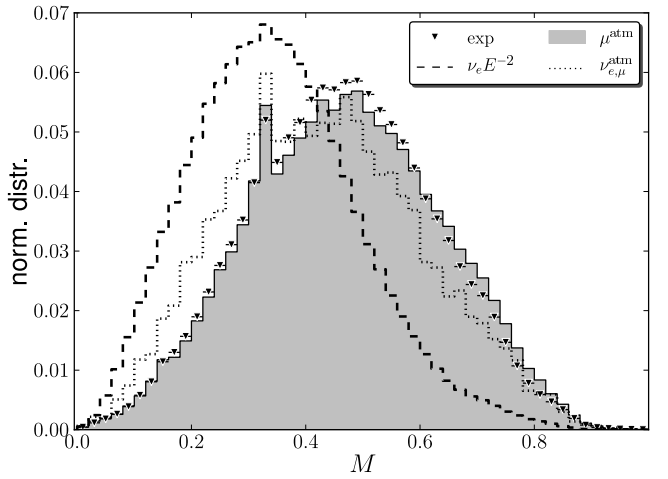

Figure 5.12: Dipole moment of the Dipole Fit: While spherical events show a value close to zero, track-like signal has values closer to one. The peak around 0.3 is a geometrical effect due to the detector geometry. (See also Sec. 4.4.8)

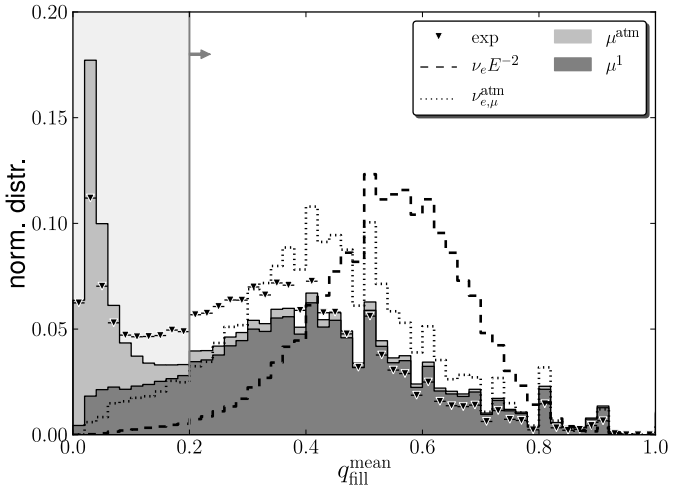

Figure 5.13: Fill ratio (based on the mean of the distance between hit DOMs and cascade position): Signal shows high values, because most DOMs close to the vertex are hit. This is not the case for track-like background. Here the single muons μ^1 are marked in darker gray, to show that especially coincident events are found in regions of low fill ratio and can thus be removed by a cut of $q_{\text{fill}}^{\text{mean}} > 0.2$. (See also Sec. 4.4.7)

the peak is overestimated in MC by about 50 % and the region between $0.1 < q_{\text{fill}}^{\text{mean}} < 0.4$ is underestimated by about 40 %. As this may indicate, that the fraction of coincident events in the simulations is not correct, an attempt was made, to modify this. The influence of the fraction of coincident events on data/MC agreement in several variables was studied, but no consistent picture was found. So the ansatz was not followed further.

The fill ratio calculated on RMS correlates only 20 % with the fill ratio calculated on the mean for the signal distribution. Therefore it was used as another BDT variable. The idea remains the same as for the previous fill ratio. The data/MC mismatch is about 20 % in the worst bins. The distribution is shown in Fig. 5.14. The peak for coincident events can no longer be observed in the distribution as most of these events were removed by the previous cut.

Another variable sensitive to the spherical signature of the signal is the eigenvalue ratio of tensor of inertia as it was already used for the pole filter (see Sec. 5.2.1). In the distribution, as shown in Fig. 5.15, there remains some cutting power, so that it is also used for the BDT training.

It was found useful, to provide the BDT with information, how much the reconstructed vertex depends on distant hits, though this variable shows no obvious separation power. The inner sphere around the vertex reconstructed with the credo algorithm (see Sec. 4.4.6) is taken and another vertex is reconstructed on the hits inside this sphere with the cascade log-likelihood algorithm (for detail see Sec. 4.4.8). The difference of z-position of the re-

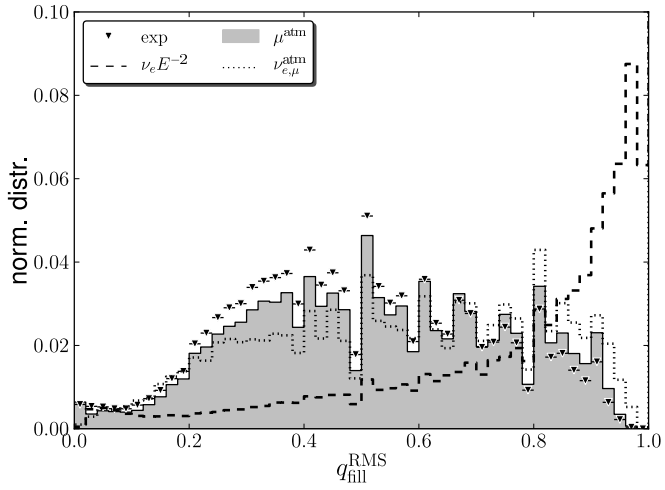

Figure 5.14: Fill ratio (based on standard deviation of the distance between hit DOMS and cascade position): as before signal shows values close to one, while background has lower values. Because the sphere radius is calculated differently, this variable is not strongly correlated with the previous fill ratio (compare Tab. 5.4, see also Sec. 4.4.7).

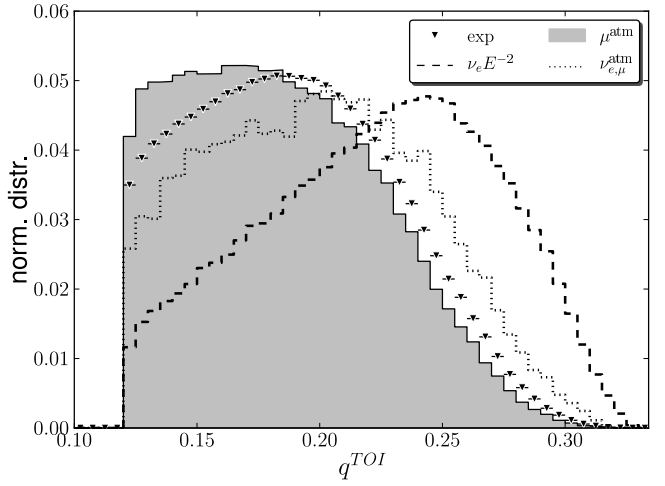

Figure 5.15: Eigenvalue ratio of tensor of inertia: Already used at the pole filter (see Sec. 5.2.1), the variable still shows some discrimination power. (See also Sec. 4.4.4)

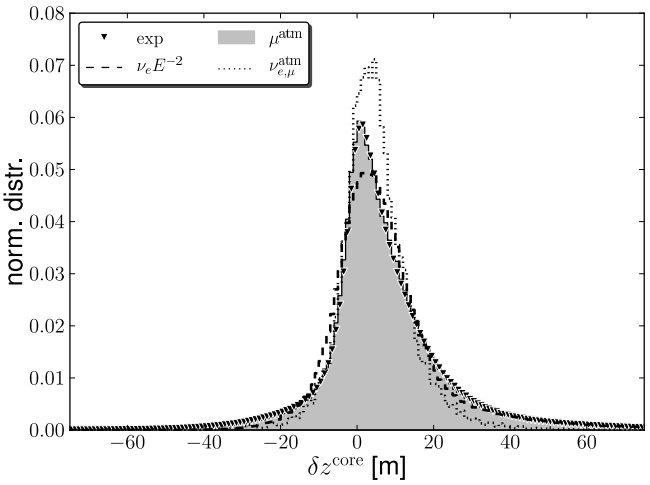

Figure 5.16: Difference of the z-position of the all pulse cascade reconstruction and one on the pulses close to the vertex: This is a quality criterion for the fit and has by itself less discrimination power. A value different from zero indicates an influence on the vertex reconstruction by distant hits. This is not expected for a (well contained) cascade. (See also Sec. 4.4.8)

construction on the core minus the z-position of the credo reconstruction was used. The distribution is given in Fig. 5.16 and shows a very good data to MC agreement.

The scaling variable f_{scale}, as described in Sec. 4.4.9, is used as information of the event position. The distribution of the cube of the scaling variable stays constant, if the events from which it was calculated, are placed with a constant volume density. This distribution is shown in Fig. 5.17. It is found that the signal events show indeed an almost constant distribution in the detector, i. e. for $f_{\mathrm{scale}}^3 < 1$, while background events peak at value close to one. This can be explained by the fact, that events at corners and edges of the detector have per se a more spherical structure compared to events directly passing the detector. It should be mentioned, that the reconstruction tends to overestimate the distance to the detector as described in E. Middell[Mid08]. It is found, that the peak in the background MC is more pronounced as in the experimental data, but the agreement is still in the order of 20 %.

The last variable used for the BDT training is also related to the event position. It is the height of the shallowest hit $z_{\mathrm{highest\,hit}}$ in the detector. The distribution, Fig. 5.18, follows basically the ice properties (compare Fig. 3.3), showing peaks in the clear regions. It shows a strong disagreement between MC and experimental data, at the top of the detector, where the background simulations peaks strongly and in the lower region of the detector around −300 m. This may be partially explained with the uncertainty of the ice properties.

For the training data samples containing 840 000 unweighted events of single muon simulation and 10^6 unweighted events of electron neutrino MC were used. The comparison between the training sample and a test sample shows (see Fig. 5.19), that the separation of

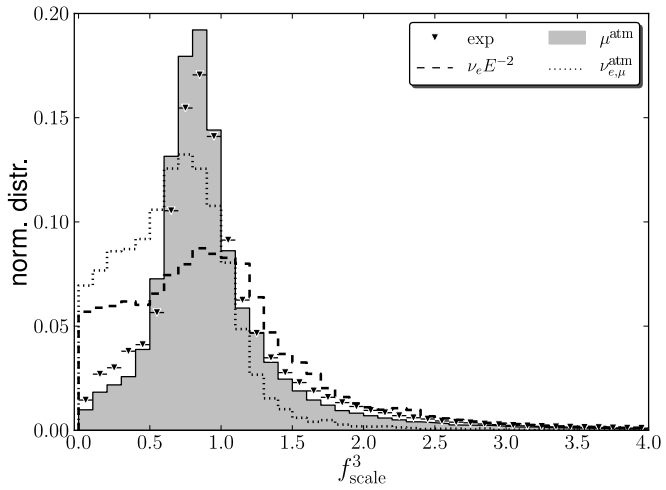

Figure 5.17: Cube of the scaling variable on the credo vertex reconstruction: The signal show an almost constant distribution up to a value of $f^3_{\mathrm{scale}} = 1.2$, indicating an evenly event distribution inside the detector. Background events peak at a value of one. The explanation is that events at edges and corners of the detector have per se a more cascade-like shape and can thus pass the earlier cuts. (See also Sec. 4.4.9)

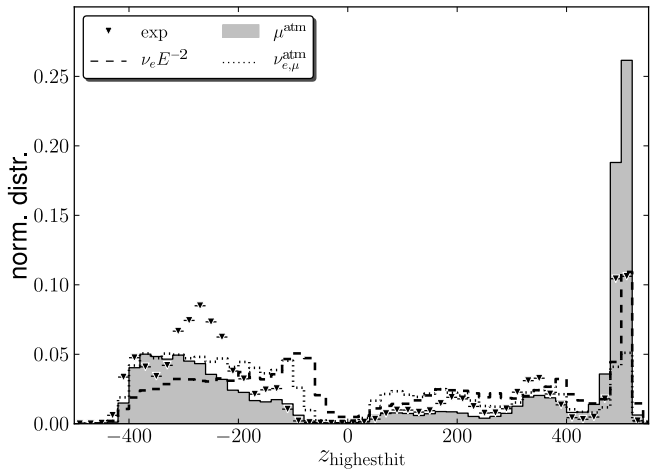

Figure 5.18: Position of the highest hit: Background shows especially hits at swallow and deep positions in the detector. Note also that this variable shows a strong disagreement between measured data and simulation at different positions in the ice. (See also Sec. 4.4.9)

Table 5.4: Correlation of BDT variables: The variables are selected such, that the correlation to each other and to energy is not higher than 35 %. Given are the correlation values between the variables for single muon background and $\nu_e E^{-2}$ signal in percent.

background										
	$\cos\theta_{\mu,32}$	δt	δz	M	$q_{\text{fill}}^{\text{mean}}$	$q_{\text{fill}}^{\text{RMS}}$	q^{TOI}	δz^{core}	f_{scale}	$z_{\text{h.h.}}$
$\cos\theta_{\mu,32}$	100	4	-25	1	-8	2	1	4	4	14
δt	4	100	-7	-1	-13	-7	0	5	4	-8
δz	-25	-7	100	-5	4	-4	2	-5	-2	-26
M	1	-1	-5	100	9	12	-3	-2	4	5
$q_{\text{fill}}^{\text{mean}}$	-8	-13	4	9	100	10	-11	-3	9	8
$q_{\text{fill}}^{\text{RMS}}$	2	-7	-4	12	10	100	3	0	3	-3
q^{TOI}	1	0	2	-3	-11	3	100	0	-6	-8
δz^{core}	4	5	-5	-2	-3	0	0	100	2	0
f_{scale}	4	4	-2	4	9	3	-6	2	100	-14
$z_{\text{highest hit}}$	14	-8	-26	5	8	-3	-8	0	-14	100
$\log_{10}\frac{E_{\text{credo}}}{\text{GeV}}$	21	3	-16	-9	-22	9	5	10	25	14
signal										
	$\cos\theta_{\mu,32}$	δt	δz	M	$q_{\text{fill}}^{\text{mean}}$	$q_{\text{fill}}^{\text{RMS}}$	q^{TOI}	δz^{core}	f_{scale}	$z_{\text{h.h.}}$
$\cos\theta_{\mu,32}$	100	2	-12	-6	1	2	-2	-24	-5	31
δt	2	100	26	13	-11	-13	-22	6	13	-10
δz	-12	26	100	10	0	-6	-7	13	2	-13
M	-6	13	10	100	19	-12	-34	3	31	-18
$q_{\text{fill}}^{\text{mean}}$	1	-11	0	19	100	21	5	-7	14	5
$q_{\text{fill}}^{\text{RMS}}$	2	-13	-6	-12	21	100	21	4	0	0
q^{TOI}	-2	-22	-7	-34	5	21	100	-4	-35	-3
δz^{core}	-24	6	13	3	-7	4	-4	100	12	-30
f_{scale}	-5	13	2	31	14	0	-35	12	100	-19
$z_{\text{highest hit}}$	31	-10	-13	-18	5	0	-3	-30	-19	100
$\log_{10}\frac{E_{\text{credo}}}{\text{GeV}}$	11	-17	-19	-12	27	31	25	0	14	15

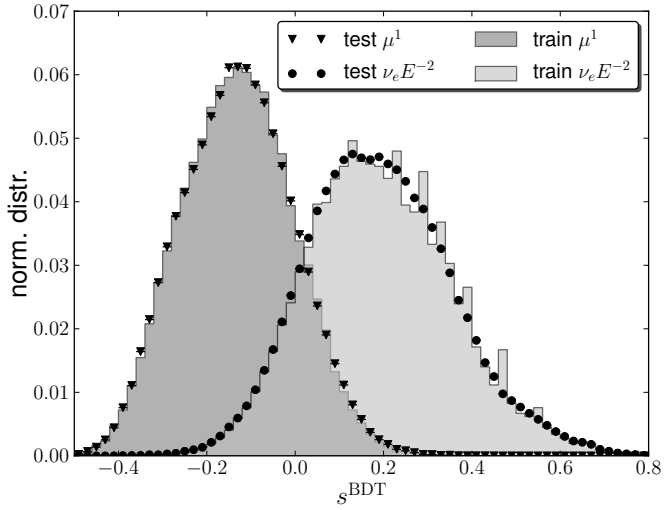

Figure 5.19: BDT distributions for single muon background μ^1 and electron neutrino signal $\nu_e E^{-2}$ for both training and test sample, that was used for the signal and background estimation. Training and test samples are in good agreement, so there is no indication for strong over-training. Peaks in the signal training sample are caused by single events with high weights, but present no problem. Compare Fig. 5.20 to see the distribution with all types of background included and for experimental data.

the training sample is more pronounced than the test sample. This is an indication of over-training. However, it is small enough to not seriously effect the discrimination power of the BDT. Another problem with over-training could be, that a bias is introduced. This is avoided by removing the training sample from the analysis. As Fig. 5.20 shows the BDT alone has not enough power to separate signal events from the background well enough for a sensitive analysis. The BDT was trained such, that it has a low energy dependency. This allows, to use the reconstructed energy from the credo reconstruction (see Sec. 4.4.6, Fig. 5.21) as a second cut variable. It alone is not enough power to distinguish signal from background: While the atmospheric neutrinos have a much steeper spectrum than the E^{-2} signal, the distribution for atmospheric background is much flatter. This is caused by extended events, that are influenced from hits along a muon track. These events can be removed by a BDT cut, that ensures the quality of event.

There are two possibilities to optimize the final cut, either to make it optimal for detecting a weak signal or to set a lower signal limit in the absence of signal. For this we define the least detectable flux ${\Phi_{\mathrm{det}}}^{\mathrm{HHH^+06}}$ and the average upper limit ${\langle\Phi\rangle_{\mathrm{lim}}}^{\mathrm{HR03}}$. We assume, we can describe the experiment with Poisson statistics and have background estimation of μ_{BG} events and a signal prediction of $\mu_{\mathrm{sig,\,test}}$ for an assumed test flux Φ_{test}. We determine the smallest number of measured events n_{crit} that is not consistent to a background only

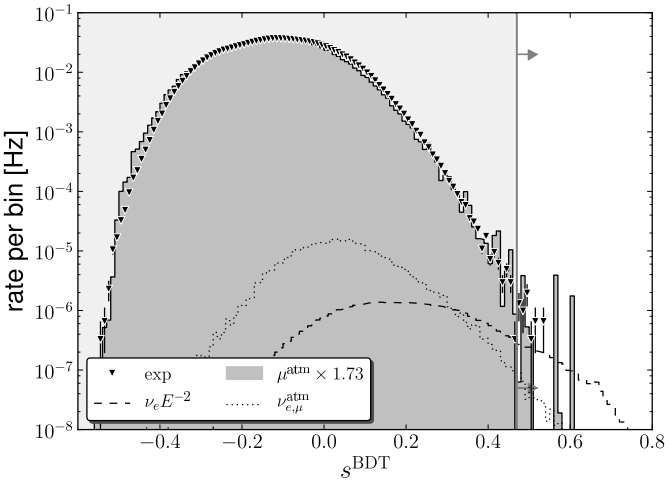

Figure 5.20: BDT distribution: Background results in lower values, while values for signal are higher. The experimental data shows reasonable agreement with the simulation prediction. For high BDT scores still a reasonable amount of simulation statistic is available. However, the discrimination power of the BDT alone is not sufficient for the desired sensitivity.

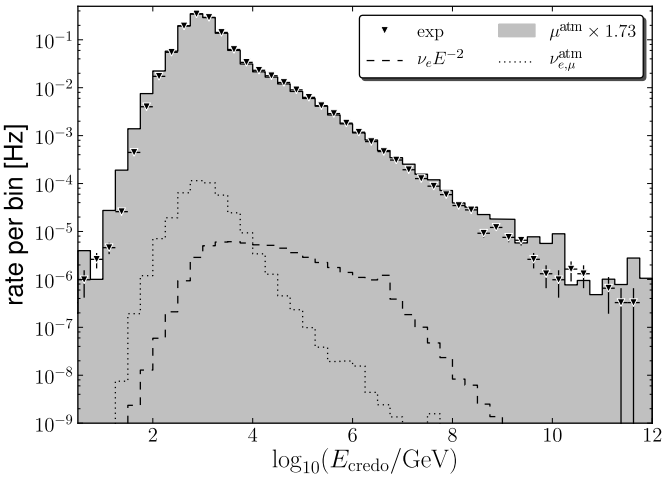

Figure 5.21: Credo energy reconstruction before the final level: Neutrino simulation (E^{-2} and $\nu_{e,\mu}^{\mathrm{atm}}$) follows the expected spectrum, atmospheric muons (data and simulated) show a comparatively flat spectrum due extended, track-like events.

expectation as

$$p(\geq n_{\text{crit}}|\mu_{\text{BG}}) < \alpha, \tag{5.5}$$

with $\alpha = 5.73 \cdot 10^{-7}$ in order to claim a "$5\,\sigma$ discovery". Now we can determine the necessary number of expected signal $\mu_{\text{sig,det}}$ that would in $1-\beta = 90\,\%$ cases yield at least the necessary number of events: $1-\beta = p(\geq n_{\text{crit}}|\mu_{\text{BG}} + \mu_{\text{sig,det}})$. This gives the model discovery factor for the given test flux

$$\text{MDF} = \frac{\mu_{\text{sig,det}}}{\mu_{\text{sig,test}}} \tag{5.6}$$

and finally the least detectable flux

$$\Phi_{\text{det}} = \text{MDF} \cdot \Phi_{\text{test}} = \frac{\Phi_{\text{test}}\mu_{\text{sig,det}}}{\mu_{\text{sig,test}}}. \tag{5.7}$$

The Feldman-Cousins approach[FC98] gives us the 90 % confidence belt $I^{90}(n_{\text{obs}}, \mu_{\text{BG}}) = (\mu^{90}_{\text{lower}}, \mu^{90})$ for expecting signal events leading to the measured number of n_{obs} events. An estimate for the upper limit before the measurement is the the average given as

$$\left\langle \mu^{90} \right\rangle = \sum_{n_{\text{obs}}=0}^{\infty} \mu^{90}(n_{\text{obs}}, \mu_{\text{BG}}) \frac{\mu_{\text{BG}}^{n_{\text{obs}}}}{n_{\text{obs}}!} \mathrm{e}^{-\mu_{\text{BG}}}. \tag{5.8}$$

This leads to the model rejection factor

$$\text{MRF} = \frac{\left\langle \mu^{90} \right\rangle}{\mu_{\text{sig, test}}} \tag{5.9}$$

and further to the average upper limit

$$\langle \Phi_{\text{lim}} \rangle = \text{MRF} \cdot \Phi_{\text{test}} = \frac{\Phi_{\text{test}} \left\langle \mu^{90} \right\rangle}{\mu_{\text{sig,test}}}. \tag{5.10}$$

For both methods the optimal BDT and energy cut combination was determined. This was done by scanning the BDT values between 0 and 0.6 in 0.01 steps and finding the best energy cut using steps of 0.1 energy decades (in G*e*V-scale). It was found, that the optimization prefers cuts, that just removes the last muon background event. As this is highly dependent on the available amount of simulation data, it was decided to fit the energy spectrum for every BDT cut.[5] In the case, that an BDT/energy cut combination removes all muon MC, the muon background prediction is based on the fit. This stabilized the optimization procedure, so that the final result is in a region, where atmospheric muon MC is still available. The cut values and corresponding average limits and least detectable flux values are listed in Tab. 5.5. The optimization for discovery reduces the background down to a single muon simulation event and has a background prediction (including atmospheric neutrinos)

[5] In Fig. 5.23 the fit for the final BDT is show.

Table 5.5: Optimization results: The cuts on BDT and energy are found by optimizing the background (BG) and the E^{-2} electron neutrino signal for discovery potential or sensitivity. Signal from other flavors and the prompt atmospheric neutrino component are listed. The given average limit and least detectable flux were only used for the optimization and include no systematic errors.

	Optimization on			
	Discovery		Sensitivity	
$s_{\mathrm{BDT}} >$	0.48		0.47	
$\log_{10}\left(\frac{E^{\mathrm{credo}}}{\mathrm{GeV}}\right) >$	5.2		4.8	
BG ($\mu^{\mathrm{atm}} + \nu_{e,\mu}^{\mathrm{atm}}$)	0.05	±0.01	0.72	±0.28
Signal ($\nu_e E^{-2}$)	37.59	±0.46	57.54	±0.49
$\nu_\mu E^{-2}$	9.35	±0.22	17.07	±0.36
$\nu_\tau E^{-2}$	23.60	±1.05	43.90	±1.79
$\nu_{e,\mu}^{\mathrm{prompt}} \times 100$	15.48	±0.08	45.06	±0.34
$E^2 \langle\Phi_{\mathrm{lim}}\rangle$ [GeVs^{-1} sr^{-1} cm^{-2}]	$3.31 \cdot 10^{-8}$		$2.76 \cdot 10^{-8}$	
$E^2\Phi_{\mathrm{det}}$[GeVs^{-1} sr^{-1} cm^{-2}]	$8.83 \cdot 10^{-8}$		$1.24 \cdot 10^{-7}$	

of 0.05 ± 0.01 events in 332 d. As this result highly depends on the last MC event it was decided to use the optimization for sensitivity. Here six simulation events survive the cuts and the background prediction is 0.72 ± 0.28 background events in 332 d with a signal prediction of 57.54 ± 0.49 for an electron neutrino flux of $\Phi E^2 = 5 \cdot 10^{-7}\, E^{-2}\,\mathrm{GeVs^{-1}\,sr^{-1}\,cm^{-2}}$. This results into an average upper limit of

$$\langle\Phi_{\mathrm{lim}}\rangle = 2.76 \cdot 10^{-8}\, E^{-2}\,\mathrm{GeVs^{-1}\,sr^{-1}\,cm^{-2}}. \tag{5.11}$$

The least detectable flux is $\Phi_{\mathrm{det}} = 1.24 \cdot 10^{-7}\, E^{-2}\,\mathrm{GeVs^{-1}\,sr^{-1}\,cm^{-2}}$ which is only 40 % higher than the least detectable flux with the cut optimized for detection.

So the chosen cuts are

$$s_{\mathrm{BDT}} > 0.47 \quad \wedge \quad \log_{10}\frac{E_{\mathrm{credo}}}{\mathrm{GeV}} > 4.8. \tag{5.12}$$

In Fig. 5.23 the energy distribution after the BDT cut is shown. The atmospheric muons and neutrinos follow a steep power law. A fit to the muon background in the energy region between $4 < \log_{10}\frac{E_{\mathrm{credo}}}{\mathrm{GeV}} < 6$ was performed and resulted in the parameterization of

$$F(E_{\mathrm{credo}}) = A\left(\frac{E_{\mathrm{credo}}}{10\,\mathrm{TeV}}\right)^{-\gamma}, \tag{5.13}$$

$$A = 8.0 \cdot 10^{-8}\,\frac{\mathrm{Hz}}{\mathrm{bin}}, \tag{5.14}$$

$$\gamma = 5.3. \tag{5.15}$$

$$\tag{5.16}$$

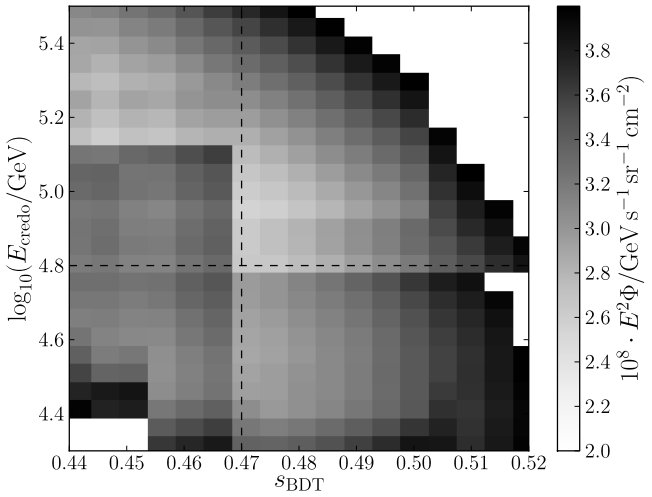

Figure 5.22: Sensitivity as function of BDT and credo energy: The dashed lines indicate the chosen cuts. The edge is caused by a single high weight event removed by the cuts. Otherwise the cut region is comparatively smooth and flat compared to borders, where the limit values fast grow outside the shown scale.

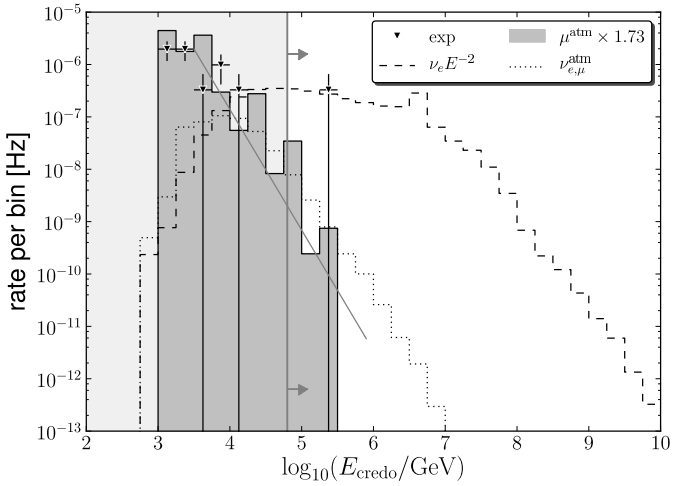

Figure 5.23: Distribution of reconstructed energy after BDT cut: The remaining muonic background as well as the atmospheric neutrinos follow a fast decaying power law. The spectral index for a fit to the muon data (gray line, details in the text) is $\gamma = 5.3$. The background is reduced by a cut on energy (vertical line). The remaining data follows the spectrum, but a single event survives the energy cut.

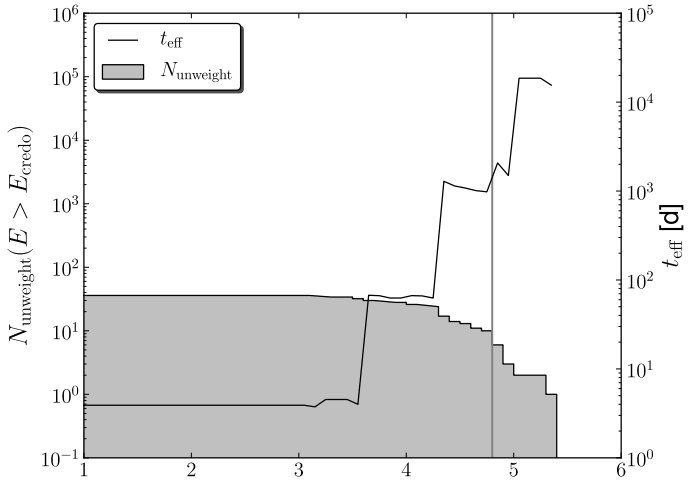

Figure 5.24: CORSIKA Life Time: The effective life time after the BDT cut is shown as a function of the energy cut. The area gives the remaining unweighted number of events. At the final cut six simulated events make a life time of 2070 d.

The background is then strongly suppressed by the energy cut. In the following section, the surviving events are discussed and the description of the analysis is closed by a discussion of the effective areas.

5.3 Analysis Summary

After the final BDT and energy cuts survive six events from the simulated atmospheric muons. They correspond according to the used weighting scheme to 0.47 ± 0.27 events, together with the atmospheric muon background this is 0.72 ± 0.28 events in 332 d. Note that the statistic error is mainly caused by the muon prediction. However, the life time of the remaining muon events (see Sec. 4.2.2) is with 2 070 d six times larger than the life time of the experimental data. In Fig. 5.24 it is shown, how the life time increases after the BDT cut as a function of the energy cut. This follows the expectation, that a harder energy cut will restrict the sample to events with higher primary energy and thus smaller weights. It should be noted, that all surviving events have not only high MC primary energies but are induced from relatively heavy particles as the list in Tab. 5.6 shows. This may indicate a problem of the simulation: The Hörandel polygonato model[Hör03] has an exponential cut-off for the energy spectrum so that for higher energy the simulated amount of protons is low. This expresses in the fact that the last proton event has only a life time of 50 d. A full discussion of this situation will be presented in Sec. 6.2.3.

The distribution of the surviving events over the detector is shown in Fig. 5.25. The muon simulation events are located outside the detector. All these events are at the edges of the detector. Fig. 5.26 shows an example of an event display. The reconstruction places the

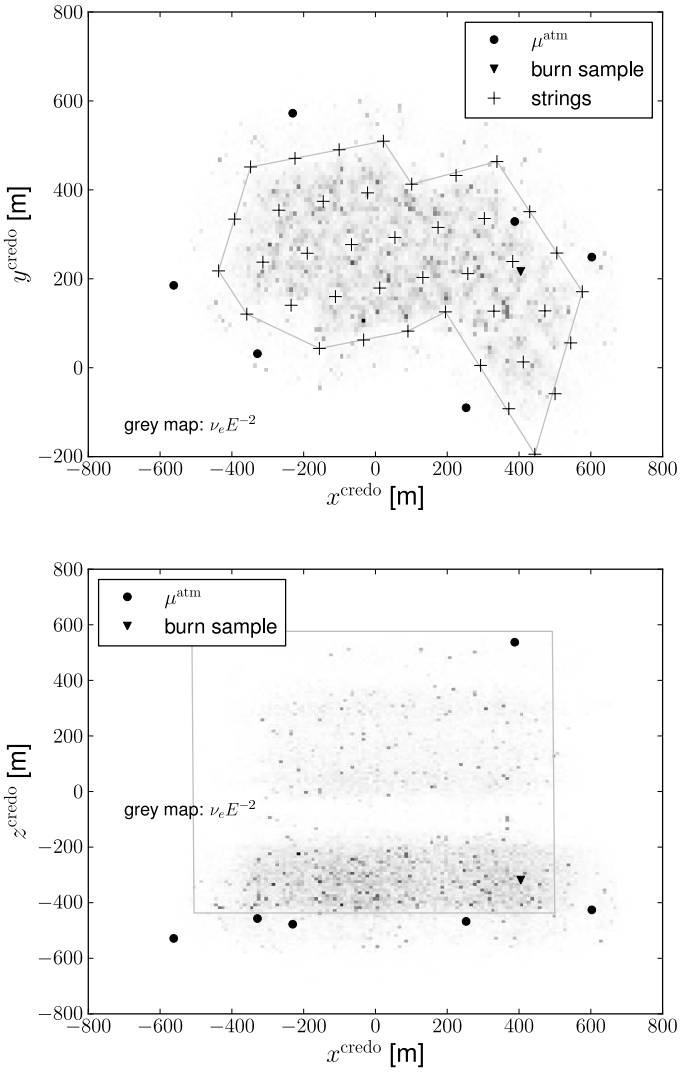

Figure 5.25: Position of surviving events: The *x*-*y* (top) and the *x*-*z*-projection (bottom) shows the position of the remaining events. The six (unweighted) single muon events (dots) are all outside the detector. The signal covers the detector area and is shown in gray shades. The remaining experimental event is contained and in the clear ice region (downward triangle).

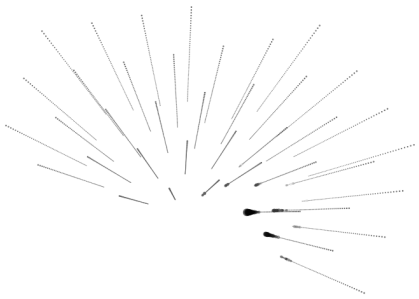

(a) Event 315 from run 2907:22003, *x*-*y* projection

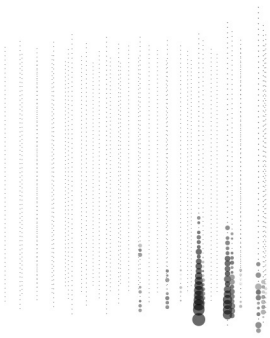

(b) Event 315 from run 2907:22003, *x*-*z* projection

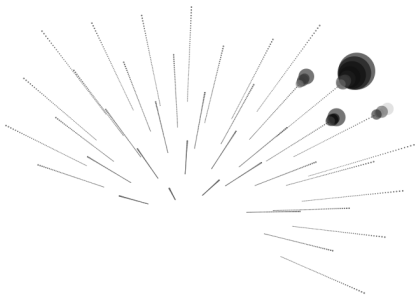

(c) Event 3890 from run 2907:29529, *x*-*y* projection

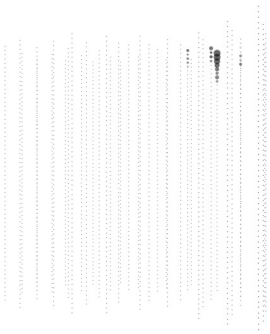

(d) Event 3890 from run 2907:29529, *x*-*z* projection

Figure 5.26: Remaining simulated atmospheric muons: From the six simulated events surviving the final cuts two examples are shown. Both are at corners of the detector and appear spherical for this reason.

Table 5.6: Surviving simulated muons: The table list there primary energy and the particle type.

$\log_{10} \frac{E_{\text{prim}}}{\text{GeV}}$	Primary Type
8.76	^{32}S
7.73	^{27}Al
8.09	^{56}Fe
7.21	^{16}O
8.27	^{56}Fe
7.63	^{56}Fe

event far outside the detector and calculates a relatively high energy. The surviving signal is mainly contained in the detector, mostly at the bottom of the detector, where the ice is very clear (compare Sec. 3.2). The x-y distribution it can be observed, that most events are reconstructed at some distance away from the deployed strings. Also the region around string 21 – the corner at (440 m, −200 m) contains only a small amount of signal.

This raise the question of the vertex and energy resolution at the final level. As shown in Fig. 5.27 the vertex resolution is 8 m for z and about 16 m for x and y, where the y-resolution is a bit worse. This can be explained by the denser DOM-spacing along z and the detector geometry, where more strings are deployed along the x-axis than along the y-axis. To take into account, that a hadronic cascade generates on average less light than an electromagnetic cascade, which are indistinguishable for this detector, the energy of hadronic cascades was scaled down by the same factor as in the simulation (compare Sec. 4.1.2). This leads to an energy resolution of 0.25 energy decades.

The neutrino energy spectrum for the surviving signal events is shown in Fig. 5.28. For the electron neutrino signal 90 % of the events are in an energy interval between 89.1 TeV and 28.2 PeV. One can observe, that the energy spectrum for muon neutrinos starts at higher values compared to the electron neutrino. This can be explained by the fact that for muon neutrinos the analysis is only sensitive to the neutral current interaction. The generated cascade do not necessary contain the full neutrino energy and may generate less light compared to charged current cascade from an electron neutrino that has a large electromagnetic fraction.

From the burn sample a single event survives the cuts. It is contained in the detector volumes and in the region of clear ice. The event display in Fig. 5.29 shows it as a spherical event with no early or distant hits indicating that this could be the bremsstrahlung-cascade on a muon track. Also a closer look at the waveforms as in Fig. 5.30 revealed no such indications: So an expectation for a muon event would be small pulses before the main light front – the muon passes a DOM and a single photon can hit it, before the muon generates the bremsstrahlung-cascade and the light from this point is back scattered and reaches the same DOM. Such things could not be found here. The probability of finding such an event in the burn sample is discussed in the result section 6.3.

Another interesting number for the analysis is the effective area A_{eff}: For a neutrino of energy E_ν, direction θ_ν and flux Φ the number of events observed in an detector with 100 %

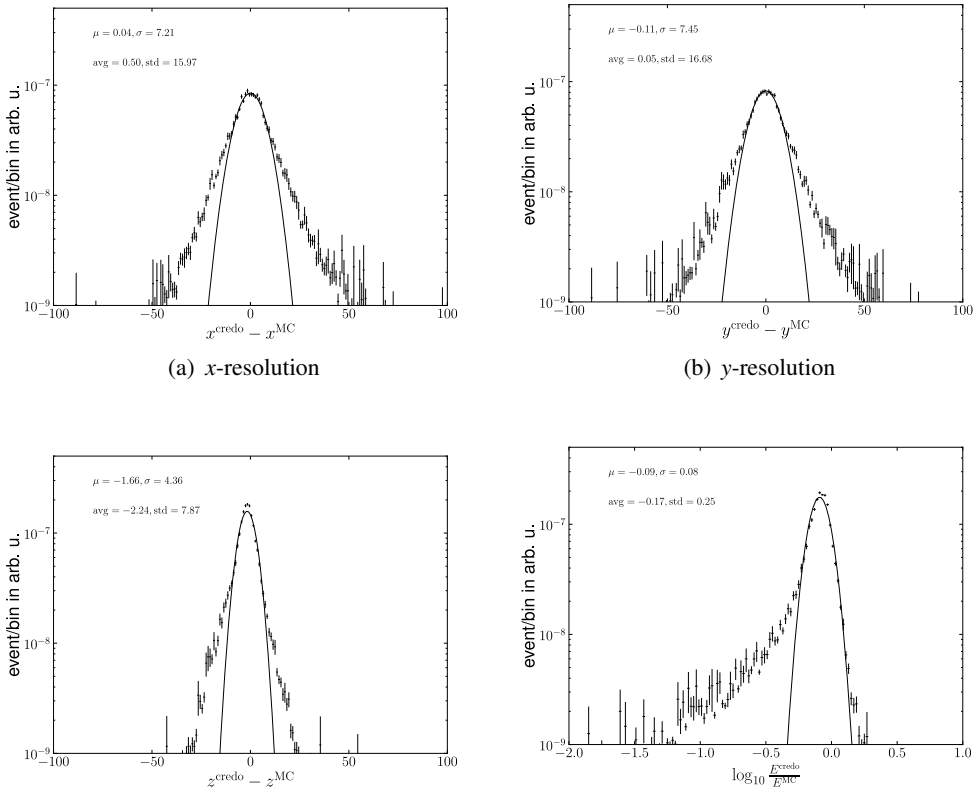

(a) x-resolution

(b) y-resolution

(c) z-resolution

(d) energy resolution (as $\log_{10} \frac{E}{\text{GeV}}$)

Figure 5.27: Energy and vertex resolution of the credo reconstruction at the final level. The resolution is given as reconstructed value minus the MC value. All distributions follow a Gauss distribution with some non-Gaussian tails. A Gauss fit on the central part is performed and medium μ and standard derivation σ of the fit are given along with the average and standard distribution in the figures. For the vertex resolutions z performs best as the DOM spacing is smallest, y is worst, because of the larger spacing compared to z and the smaller width of the detector along this direction, compared to x. For the energy resolution the reconstruction was compared to a corresponding electromagnetic cascade (see text). Still the energy was underestimated in more events than overestimated. This can happen for events outside the detector, where not all light is recorded.

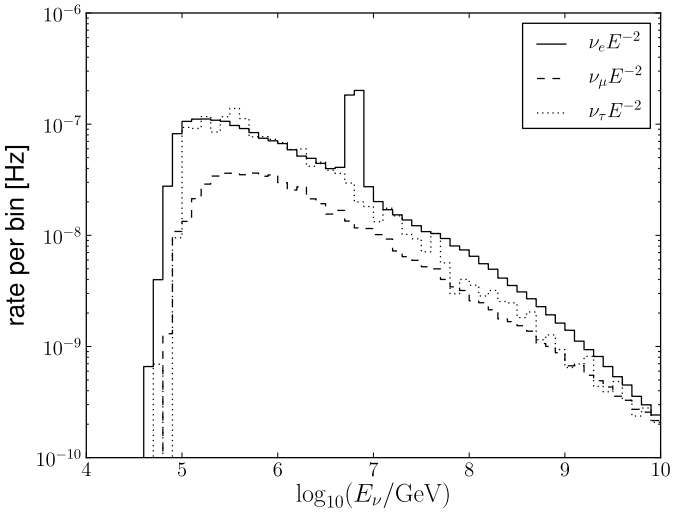

Figure 5.28: The energy spectra of the surviving signal events. Shown is the simulated neutrino energy. The spectra follow the E^{-2} flux. For the electron neutrino the Glashow resonance is clearly visible.

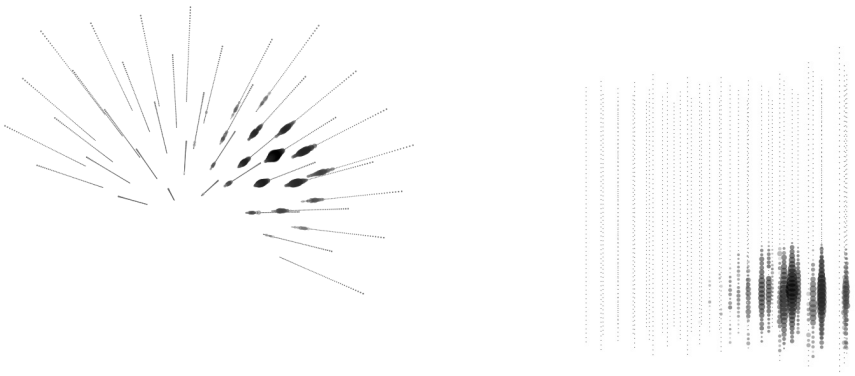

Figure 5.29: The *x*-*y* (left) and the *x*-*z*-projection of the surviving experimental event. Hit DOM are filled, dark for early, lighter for late hits, the size is proportional to the logarithm of the amplitude and anti-proportional to the distance of the projection plane. The event shows the round and static light pattern as expected for a cascade. No indications of a muon as distant or early hits are observed. The first hits are inside the detector.

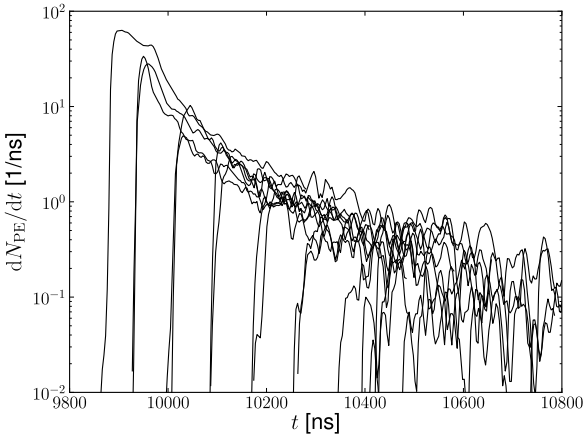

Figure 5.30: Waveform of the surviving data event. All waveforms agree well to each other, no early peaks in single waveforms indicate a weak muon track. Waveform starting later than 10 400 ns after the event begin are not shown for readability.

efficiency and the area A_{ideal} during an observation time of t is given by

$$\frac{\mathrm{d}^2 N}{\mathrm{d}E_\nu \mathrm{d}\Omega}(E_\nu, \theta_\nu) = \Phi(E, \theta_\nu) A_{\mathrm{ideal}} t. \tag{5.17}$$

If a detector with not 100 % efficiency measures the same number of events in the given direction and energy, it has the effective area $A_{\mathrm{eff}} := A_{\mathrm{ideal}}$. As this analysis is not sensitive to the direction the integral over the solid angle is taken. The effective areas for electron neutrinos at different analysis levels is shown in Fig. 5.32. It shows nicely that the analysis is quite efficient recording low energies until the final energy cut is applied. Most of the reduction in effective area is due to the final BDT cut. This is in agreement with the event numbers predicted in Tab. 5.2. In Fig. 5.31 the effective areas at the final cut level for the different neutrino flavors are shown. The analysis is most sensitive for electron neutrinos, for which it was optimized, especially in the region of the Glashow resonance (see Sec. 2.3.1). Tau neutrinos have about the same effective area, as the charged current interaction results in a cascade-like event. With higher energies the signature of tau neutrino interactions is expected to change, due to the extended length the tau lepton can propagate before decaying. This is observed as lower effective areas compared to electron neutrinos for energies above 10 P*e*V. Finally the effective area for the IC40 diffuse search for extra high energies from H. Johansson[Joh11] was compared to this work, see Fig. 5.33. This work has a higher effective area in a small energy region between $4.8 < \log_{10} \frac{E_{\mathrm{MC}}}{\mathrm{G}e\mathrm{V}} < 5.5$, while the area from H. Johansson is higher for higher energies, especially above 1 E*e*V, where the effective area of this work does not improve any further. So the work of H. Johansson is expected to perform better, but also be more restricted to the higher energies, which directly

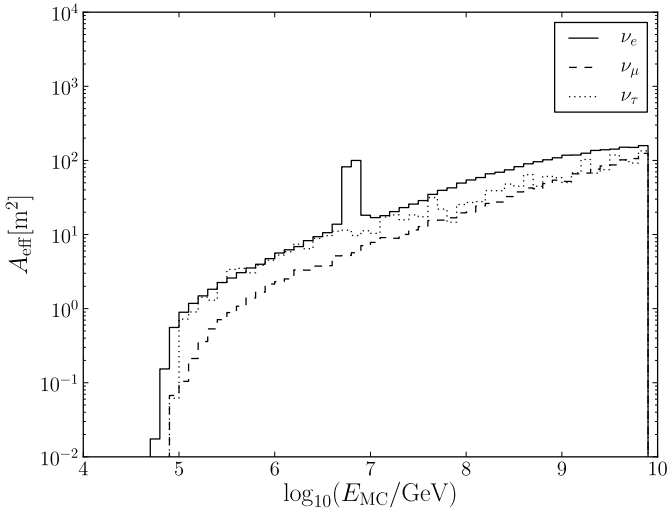

Figure 5.31: Effective areas of different neutrino flavors. The electron neutrino flux, for which the analysis was optimized, shows the highest effective areas. Tau behaves similarly, while muon neutrinos have lower areas, after their charged current events may be rejected as background. The peak in the electron neutrino area is due to the Glashow resonance.

reflects in the energy region from which 90 % of the signal originates:

$$E^{90\,\%}_{\mathrm{Johansson}} = \left\{ E_\nu \left| 6.3 < \log_{10} \frac{E_\nu}{\mathrm{GeV}} < 9.8 \right. \right\} \tag{5.18}$$

The analysis described here was applied to the measured data. The results and discussion of systematic uncertainties is given in the next chapter.

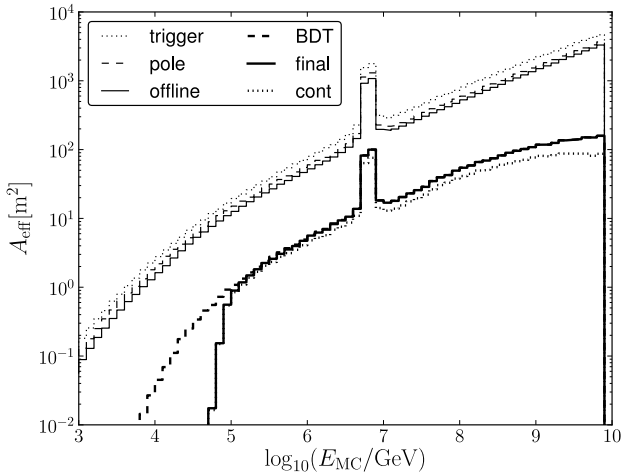

Figure 5.32: Effective areas at different cut levels for the $\nu_e E^{-2}$ signal: From trigger level over pole filter to the offline filter level the changes of effective area are in the order of 10 %, while from the offline level the area is decreased about one order of magnitude by the BDT cut. The energy cut is responsible for a hard cut-off below 60 TeV. A containment cut would reduce the area by about 10 % for the high energy region and was not applied.

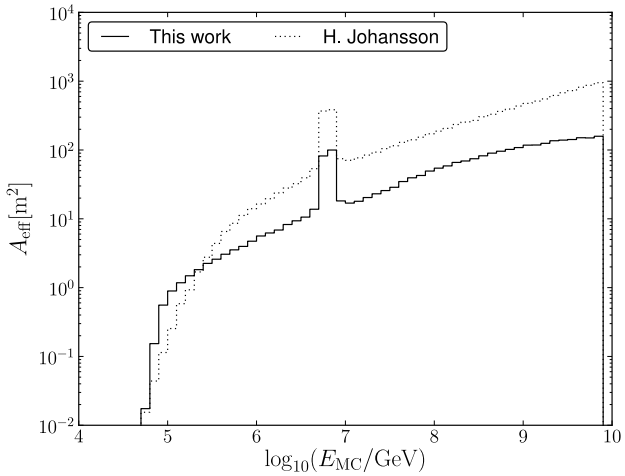

Figure 5.33: Effective areas of this analysis at the final level for $\nu_e E^{-2}$ compared to corresponding effective area of H. Johansson [Joh11]. This analysis performs better in a region between $4.8 < \log_{10} \frac{E_{\mathrm{MC}}}{\mathrm{GeV}} < 5.5$, But the work from H. Johansson has higher effective areas for higher energy, even for energies above 1 EeV, where this work begins to saturate. This behavior seems natural as the work from H. Johansson was designed for higher energies.

6 Results

In the previous chapter the analysis was introduced. It follows a blindness policy in order to avoid biases. Therefore the final cut optimization was based completely on MC data. Only a burn sample of 10 % of the data was used to verify the simulation data. This chapter focuses on the results of unblinding, i. e. the application of the analysis to the remaining 90 % of the measured data. The chapter begins with application of the analysis to flasher data in order to show its ability to detect signal-like events. Then the systematic uncertainties, caused by uncertain assumptions in the simulations, were estimated. Finally the unblinding results are presented.

6.1 Systematic Check with Flashers

In absence of a natural, known source of cascade-like signal, artificial light sources are needed, in order to compare the simulated signal with measured data. Therefore, the analysis was applied to flasher data. In some distance from the flashing DOM light scattering in the ice will cause a spherical light pattern, very similar to that of a cascade.[1] The flasher runs 111739 and 111741, described and previously studied in McCartin[McC09], were used here. From the runs only the events with full flasher intensity and with all six horizontal LEDs activated were taken. The active flashers are at different DOMs on string 63, that is located in the middle of the 2008 detector (see Sec. 3.1.1, Fig. 3.1).

Several events include coincident muons. This manifest itself in very shallow highest hits far above the position of the active flasher as shown in Fig. 6.1. To exclude this events from the analysis it was required, that the first DOM launch was recorded on string 63. Additional a position (z^{flasher}) dependent cut on the highest hit position $z_{\text{highest hit}}$ was defined, that follows the main peak in Fig. 6.1:

$$z_{\text{highest hit}} - z^{\text{flasher}} < \begin{cases} 40\,\text{m} - 0.7z & \text{if } z < -75\,\text{m}, \\ 330\,\text{m} - 0.37z & \text{otherwise.} \end{cases} \tag{6.1}$$

The charge distribution for the remaining flasher events is given in Fig. 6.2: There are large variations between different DOMs as expected due to the ice properties, but the variation for the events for a fixed DOM are small, i. e. in agreement with the assumption that differences are within the uncertainty of the measurement process. Though all these events pass the cut up to the online level and also the final energy cut, only few pass the final BDT cut. The efficiency as a function of depth is shown in Fig. 6.3(a). Only in a small region in the clear ice the efficiency is close to one. As already indicated by the position of the

[1] In principle standard candle data should be even more cascade-like. But only data for two positions is available: at $z \approx 200\,\text{m}$ at string 40 and at $z \approx -200\,\text{m}$ at string 55.

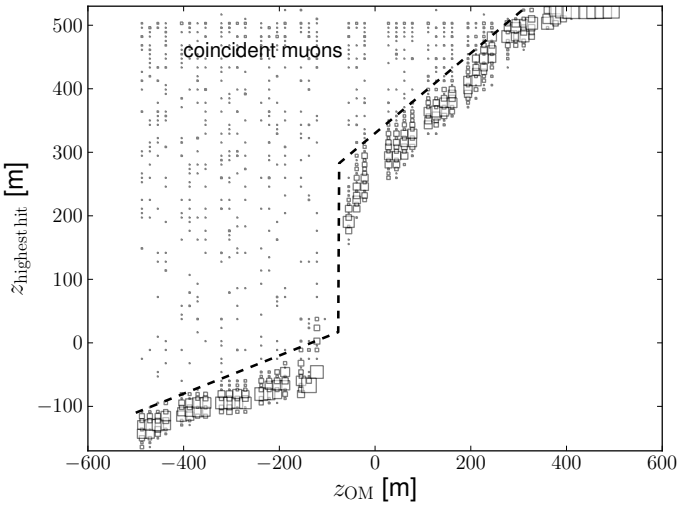

Figure 6.1: Distribution of the highest hit z-position as function of the z-position of the flashing DOM. For all flasher positions some events have very high hits, likely caused by coincident muons. These events were removed by a cut along the dashed line.

surviving signal events, compare Sec. 5.3, Fig. 5.25, the analysis shows a bad performance for events close to strings. This is likely caused by problems of the reconstruction for events close to strings.[Stöß11] Comparing the efficiency of electron neutrino MC for events close to string 63, also shows low values, see Fig. 6.3(b). As mentioned above, the events from one flasher are very similar to each other. Therefore the efficiency values for flasher events are more extreme, i. e. either close to one or very low, compared to MC.

The tests performed with Flasher events is only partially conclusive, while there are regions where the analysis performs well, others indicate a very small efficiency for flasher events. These can be partially explained by the special location of the flashers, however, without a dedicated MC data set for flasher events, a definite conclusion can not be drawn at the moment.

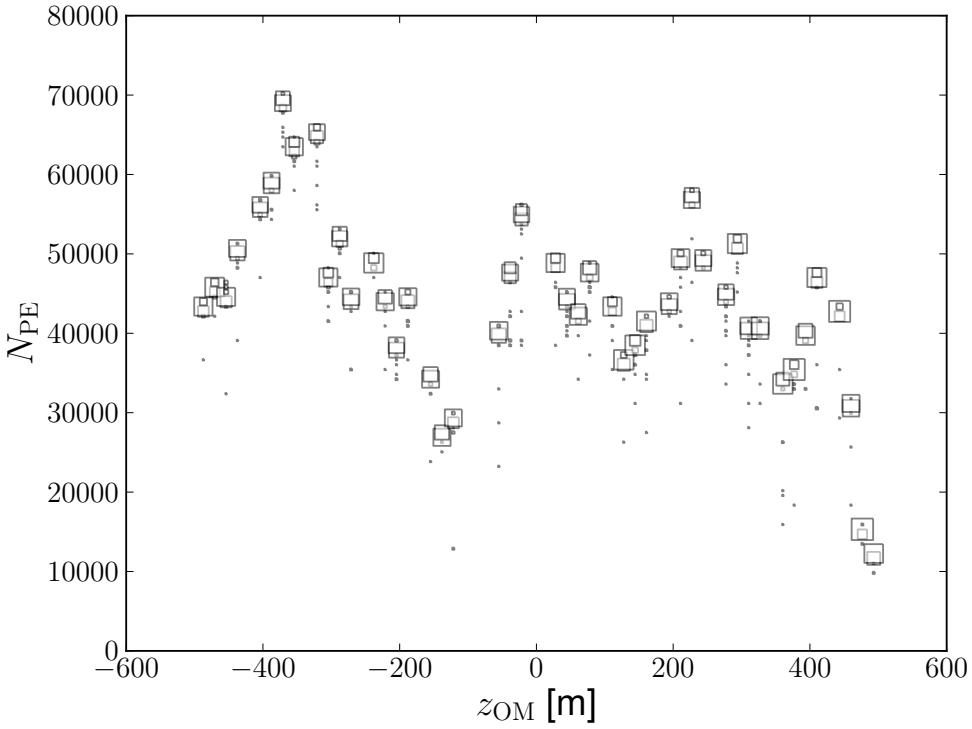

Figure 6.2: Charge distribution over the z-position of the flashers. The box size is proportional to the logarithm of the number of events. The charges vary strongly between different positions corresponding to the optical properties of the ice. However, the distribution for every single flasher is rather sharp, as expected for almost identical events.

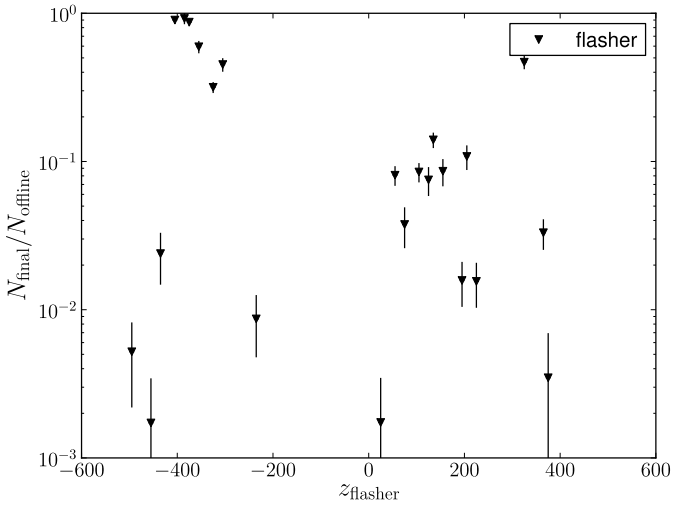

(a) Efficiency for flasher data.

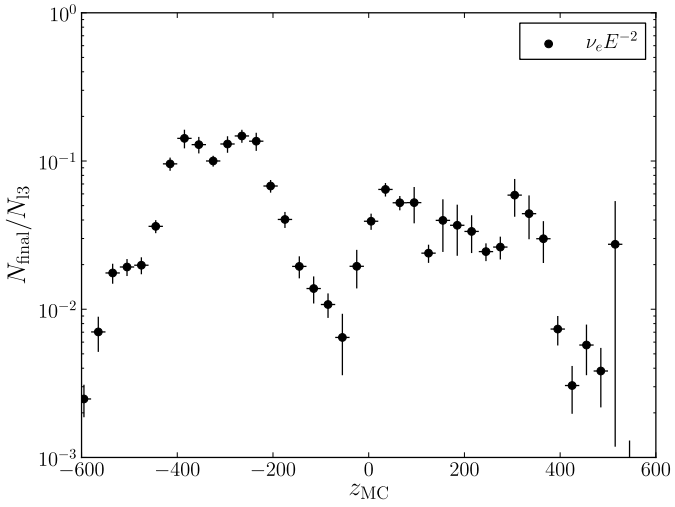

(b) Efficiency for MC data.

Figure 6.3: Efficiency of the analysis for flasher data and $\nu_e E^{-2}$ simulation: For the simulation data only events in a distance of 30 m from string 63 were used. Shown is the ratio of events at the final level compared to the events after the offline filter as a function of the simulated z-position of the cascade or the flashing DOM. The general shape is consistent. As flasher events are very similar, the efficiency is either close to one or very low, while for MC only most efficiencies are between one tenth and one hundreds.

Table 6.1: Summary of systematic uncertainties: For the different fluxes the different systematic uncertainties are listed. Note, that for atmospheric muons contributions from other sources are already included in the estimation of the uncertainty raising from the scaling factor and are only listed to give an estimate.

Type	μ^{atm}	$\nu_{e,\mu}^{\text{atm}}$	$\nu_{e,\mu}^{\text{prompt}}$	$\nu_e E^{-2}$
Data/MC comparison	$\pm^{322}_{100}$ %	–	–	–
Ice model	($\pm$32.0 %)	$\pm$40.4 %	$\pm$21.6 %	$\pm$3.4 %
DOM efficiency $^{110}_{90}$ %	($\pm^{66.7}_{23.8}$ %)	$\pm^{66.7}_{23.8}$ %	$\pm^{28.5}_{26.7}$ %	$\pm$14.2 %
Flux model	($\pm$20 %)	$\pm$15 %	$\pm^{28.6}_{41.0}$ %	–
Seasonal variations	($\pm^{24.0}_{8.9}$ %)	$\pm$5 %	$\pm$5 %	–
E_{reco}	–	$\pm^{37.5}_{23.8}$ %	$\pm^{23.1}_{20.1}$ %	$\pm$7.5 %
ν cross sections	–	$\pm$18.3 %	$\pm$9.4 %	$\pm$8.8 %
Total uncertainty	$\pm^{322}_{100}$ %	$\pm^{89.8}_{57.9}$ %	$\pm^{52.4}_{58.1}$ %	$\pm$18.6 %

6.2 Systematic Uncertainties

All the assumptions used in the MC simulation are sources of systematic uncertainties. To estimate the effects of different assumptions on the event prediction special simulation data sets were used (compare Sec. 5.1). A summary of the estimated uncertainties is given in Tab. 6.1. For the atmospheric muon prediction the systematic uncertainties were directly estimated with a comparison to the measured burn sample data. The procedure is described in detail in Sec. 6.2.1. This yields an uncertainty of $\pm^{322}_{100}$ %, which is rather large. The estimate includes the other uncertainties listed in Tab. 6.1 and are given there only for completeness. In the following sections the error estimation method based on the data/MC comparison and for the uncertainties of detector properties, on the flux normalization and the interaction cross sections will be briefly described.

6.2.1 Uncertainties Estimation from MC/Data Comparison

At trigger level the rate predicted from the MC is in reasonable agreement with the measured rate. However, several of the variables used in this analysis show discrepancies between data and MC (see Fig. 5.9 to Fig. 5.18). Cuts on such a variable influence data and MC differently, the MC rate may not agree with the measured rate anymore. The ratio of experimental rate to MC rate prediction is shown in Fig. 6.4 for the different cut levels. Ideally one would use MC, that is in better agreement to the measured data. For this properties, e. g. the optical properties of the ice, DOM efficiencies, cosmic ray composition, needed to be known more precisely and simulated more accurately. Also large amounts of simulation are required, which is a collaboration-wide effort. So it was only possible to use the available simulation, which was the best MC description known at the time of the analysis. One could now try to avoid, variables with bad agreement. But this is only possible to some degree, as many variables are subject to some disagreement. The remaining variable would drastically decrease the separation power of the analysis. These thesis chose to work with

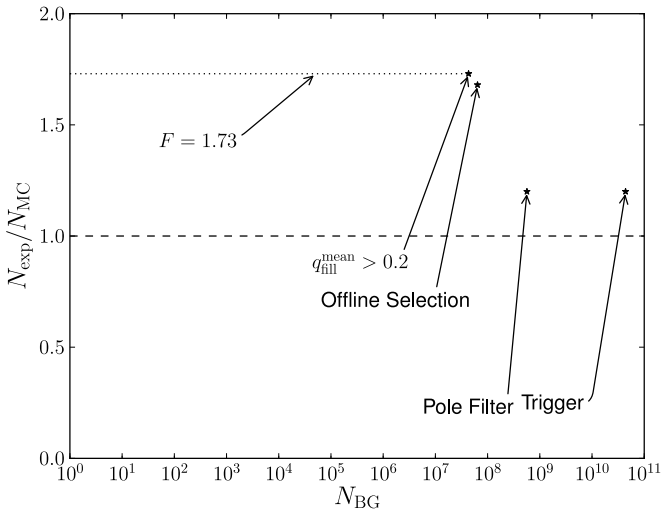

Figure 6.4: Ratio of experimental to MC rate at different experimental background rates corresponding to the different cut levels. The ratio after the fill ratio cut is taken as scaling factor to scale the MC prediction for the final level.

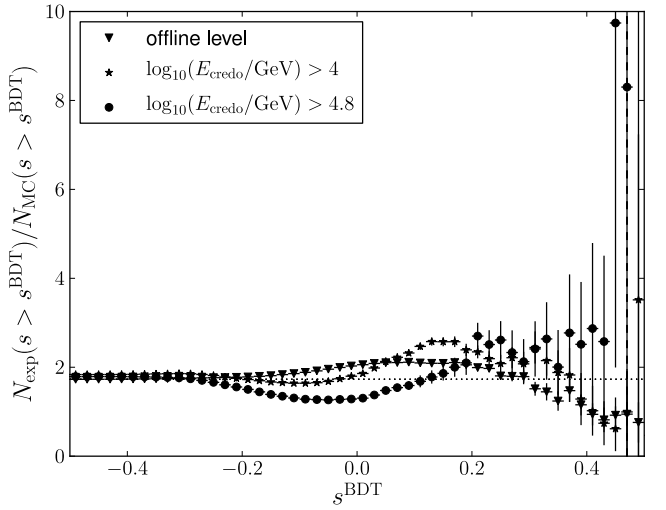

Figure 6.5: Variation of the data/MC rate over the BDT after different energy cuts: The scaling factor was set to the value of 1.73 that is the ratio of data over MC rate immediately before the cut optimization. Shown is the data/MC ratio as function of different BDT and without (triangle), with a soft energy cut (stars) and with the final energy cut (circles). In the parameter space of the optimization the ratio of data rate to MC rate varies in a broad range.

the available simulation data and variables and absorbs the mismatch in normalization constant[2] F. It was chosen as the ratio of experimental rate to the MC rate after offline filtering and cut on fill ratio (see Sec. 5.2.3):

$$F := \left.\frac{N_{\text{exp}}}{N_{\text{MC}}}\right|_{\text{after fill ratio cut}} = 1.73 \tag{6.2}$$

The scaling factor had to be fixed before the final cut optimization. It cannot be redefined at the final level as the experimental statistics is too low. Also it is not desired, as at this level the background is no longer dominated by atmospheric muons and even may be "contaminated" with signal. To fix the scaling factor at the last cut before the BDT energy cut combination is a arbitrary choice. However, it is stable over a long region of soft BDT cut up to a value of $s_{\text{BDT}} > -0.3$ (compare Fig. 6.5). To estimate the systematic uncertainty resulting from this choice the experimental to MC rate ratio for different BDT and energy cut values was plotted, see Fig. 6.5. The ratio seems to vary roughly between 0.8 and 2.6 leading to a systematic uncertainty of $((N_{\text{exp}}/N_{\text{MC}})^{\text{max,min}} - F)/F = \pm 52.0\,\%$. This uncertainty is due to the choice of the scaling factor. But the mismatch between data and MC contains most information about all systematic uncertainties. To extract an estimation a new BDT score s'_{BDT} for MC is defined as a linearly transformation of old BDT s. The modified BDT shall answers the question, to which value a cut on MC has to be tuned, in order to get about the same rate as in the measurement. Therefore the transformation is chosen such, that the ratio of (old) BDT on data over new BDT on MC is almost constant for all BDT values:

$$N_{MC}(s'_{\text{BDT}} > s) \approx F N_{MC}(s_{\text{BDT}} > s) \quad \forall s. \tag{6.3}$$

This is approximately given with the following transformation:

$$s'_{\text{BDT}} = a \cdot s_{\text{BDT}} + b \quad \text{with } a = 0.92 \quad \text{and } b = 0.02. \tag{6.4}$$

Especially for the upward fluctuation between BDT values of -0.1 and 0.2 the new distribution agrees better to a constant scaling factor as shown in Fig. 6.6. So the final BDT cut of 0.47 corresponds to a cut of 0.445 on data. That yields 322 % more atmospheric muon events. A a symmetric error would be nonphysically, the downside error was estimated to 100 %. This values are taken as the systematic uncertainty for the atmospheric muon background. The following sections also discuss systematic uncertainties on the muon prediction, to illustrate, how the high uncertainty builds up.

6.2.2 Uncertainties of the Detector Properties

Two main uncertainties of the detector properties affect the analysis: the DOM efficiency and the optical properties of the ice, i. e. the ice model. To test the systematic effects of the detector properties data sets with different DOM efficiencies and data sets with a different ice model were studied (see Tab. 5.1).

[2] The scaling factor F is a fixed value, while the ratio of event numbers from data over MC varies with the applied cut. The text strictly distinguish these two.

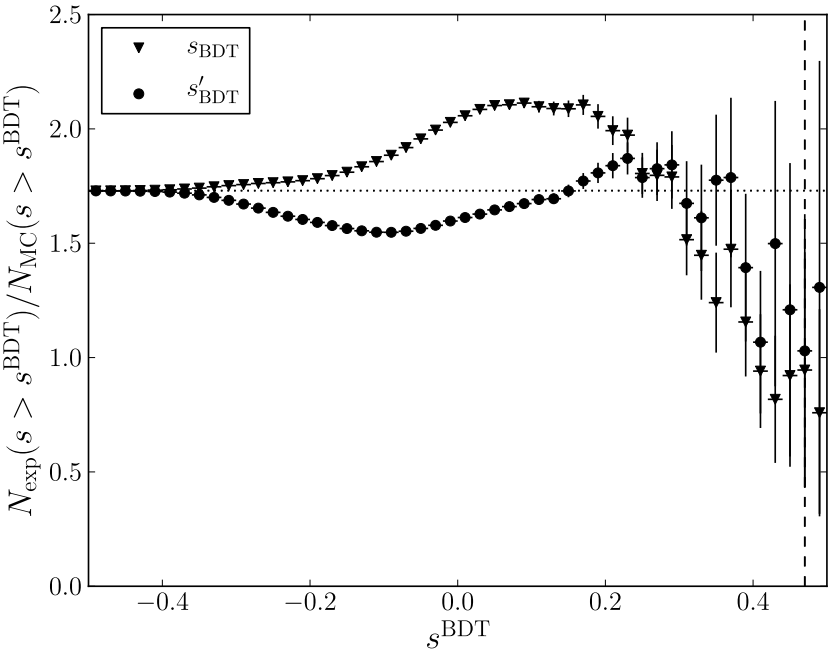

Figure 6.6: Ratio of experimental rate over MC rate as a function of the BDT cut. Using the BDT score s_{BDT} for data and MC results in variations due to the disagreement in several variables (triangles). If one uses a modified BDT score s'_{BDT} for the MC one reaches a more flat behavior. This modified BDT was used to estimate the effect of the scaling factor and the data MC disagreement.

Table 6.2: Effect of the DOM efficiencies: The table shows the predicted event numbers after final cuts for 332 d based on muon neutrino simulation with different DOM efficiencies.

DOM efficiency	μ^{atm}	ν_μ^{atm}	$\nu_\mu^{\mathrm{prompt}}$	$\nu_\mu E^{-2}$
90 %	–	0.14	0.072	11.9
100 %	–	0.19	0.090	14.0
110 %	–	0.32	0.117	15.5
uncertainty	$\pm^{66.7}_{23.8}$ %	$\pm^{66.7}_{23.8}$ %	$\pm^{28.48}_{26.71}$ %	±14.2 %

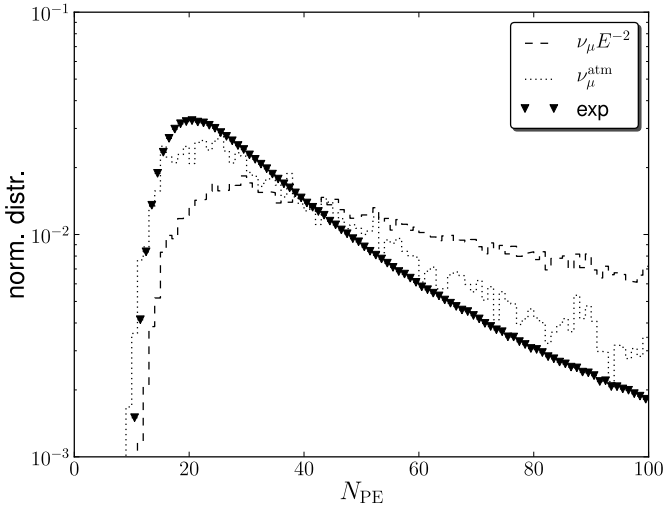

Figure 6.7: Total charge distribution for measured data and atmospheric and E^{-2} muon neutrino flux. The data distribution compares best to the atmospheric flux. So the atmospheric neutrino simulation can be used to estimate the influence of the DOM efficiency for the atmospheric muon background.

For the DOM efficiencies muon neutrino simulation data set with 90 % and 110 % DOM efficiency were used. They were weighted to atmospheric and E^{-2} flux. The predicted event numbers are listed in Tab. 6.2. No data sets for electron neutrinos were available. However, at the final cut level mainly cascades from neutral current interactions are selected. So a transfer of the result from muon neutrinos to electron neutrinos is reasonable. Also no atmospheric muon data were simulated. In order to make a rough estimation, it was assumed, that the effect of the DOM efficiencies is proportional to the total charge measured for the event (and the event topology can be neglected). In order to find the weighting schema, that agrees best to atmospheric muons, the total charge distribution of measured data and the two muon neutrino fluxes are compared, see Fig. 6.7. The shape of the data distribution is best described by the atmospheric flux. Therefore the systematic uncertainties due to the unknown DOM efficiencies for the atmospheric neutrinos can be taken as a rough estimate for the uncertainties for the atmospheric muons. This gives an estimate of the systematic uncertainty for atmospheric muons and neutrinos of each $\pm^{66.7}_{23.8}$ %, for the prompt component of $\pm^{28.48}_{26.71}$ % and ± 14.2 % for the E^{-2} signal flux.

For the comparison of the ice models data set simulated with the SPICE1 ice model (see Sec. 3.2) were used. Available was an electron neutrino data set, which was used to estimate the effect on the neutrino fluxes, as well as an atmospheric muon data set. But the latter held not enough statistics to apply the final cuts. Therefore the event numbers for the muon background from the simulations with different ice models were compared

Table 6.3: Effect of the ice model: Given are the predicted event numbers for 332 d after final cuts. For the atmospheric muon background only the energy but not the BDT cut was applied, as it would remove the full SPICE1 data set. The default ice model (see Sec. 3.2) for this work is AHA, SPICE1 was only used for the systematic study.

Ice Model	μ^{atm}	ν_e^{atm}	ν_e^{prompt}	$\nu_e E^{-2}$
AHA %	$632 \cdot 10^3$	0.065	0.38	47.1
SPICE1 %	$835 \cdot 10^3$	0.090	0.46	48.8
uncertainty	±32.0 %	±40.4 %	±21.6 %	±3.4 %

after applying the offline filter cuts and the final energy cut.[3] Predicted numbers of events are listed in Tab. 6.3. For atmospheric muons the SPICE data set predicted 32 % more events than AHA. In order to extrapolate this result to the final cut level the ratio of rates between the experiment and the simulation, as shown in Fig. 6.8, as a function of the BDT is compared. The ratio is smaller for the SPICE data and keeps constant up to a BDT score of $s_{\text{BDT}} < 0.2$. However, in the region close to the final cuts, the curves for SPICE and AHA both drop with the same sloop. This justifies to transfer the systematic uncertainty for the atmospheric muon background from the mediate level to the final cuts.

6.2.3 Uncertainties from the Flux Prediction, Interaction and Measurement

The uncertainties of the atmospheric neutrino flux were taken from Barr et al. [BRGS06] for the conventional component (±15 %) and from Enberg et al. [ERS08] for the prompt component ($\pm^{28.6}_{41.0}$ %). The cosmic ray flux uncertainty in the Hörandel model[Hör03] is given as 20 %. At energies above 1 E*e*V the simulation deviates from measurements, as primary particles heavier than iron are not included in the simulation. This is for the technical reason that the used CORSIKA version is not capable of simulating such nuclei. However, the impact for this work is small: the surviving simulated muons have primary energies around 100 P*e*V. The contribution from energies at 1 E*e*V would be about hundred times smaller, as the cosmic ray spectrum follows a steep power law. A more serious observation is, that all muon events surviving the final cut are from heavy elements. It seems that the MC simulation data used does not have enough statistic for protons, since no proton event survive all cuts. After the BDT cut only 20 % of the simulated raw events are protons, but they make up 95 % of the weighted particles. The proton event with the highest energy surviving the BDT cut has an effective lifetime of 46 d. This lack of proton statistics is likely to have a large impact, because the analysis selects mainly protons (compare Fig. 6.9). This is expected behavior as showers from protons have highly energetic muons, that generate very energetic bremsstrahlung-cascades, that are difficult to distinguish from a neutrino induced cascade. Muon bundles, typical for the interaction of heavier cosmic ray primaries, have a more even light distribution, that is easier to identify as background.

[3] The BDT cut would remove all events for the SPICE1 data set.

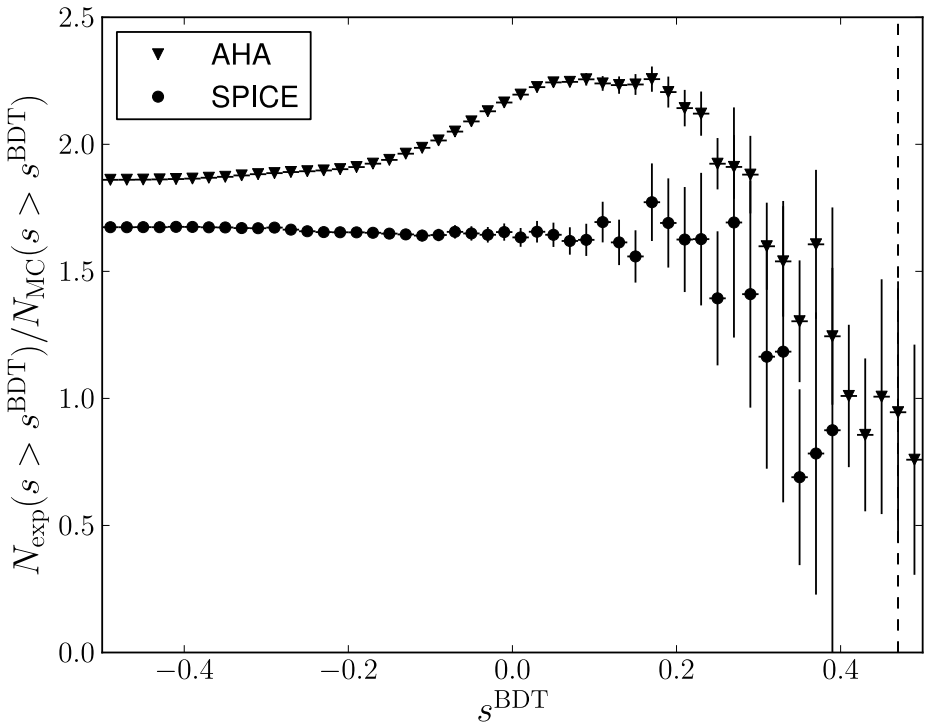

Figure 6.8: Ratio of experimental rate over MC rate as function of the BDT cut for AHA and SPICE ice model. No coincident events were included, so the ratio is higher than in Fig. 6.6. The upward turn is not visible in SPICE data, but the behavior toward the final cut is very similar, so that a extrapolation from rate after applying only an energy cut to the final level seems reasonable.

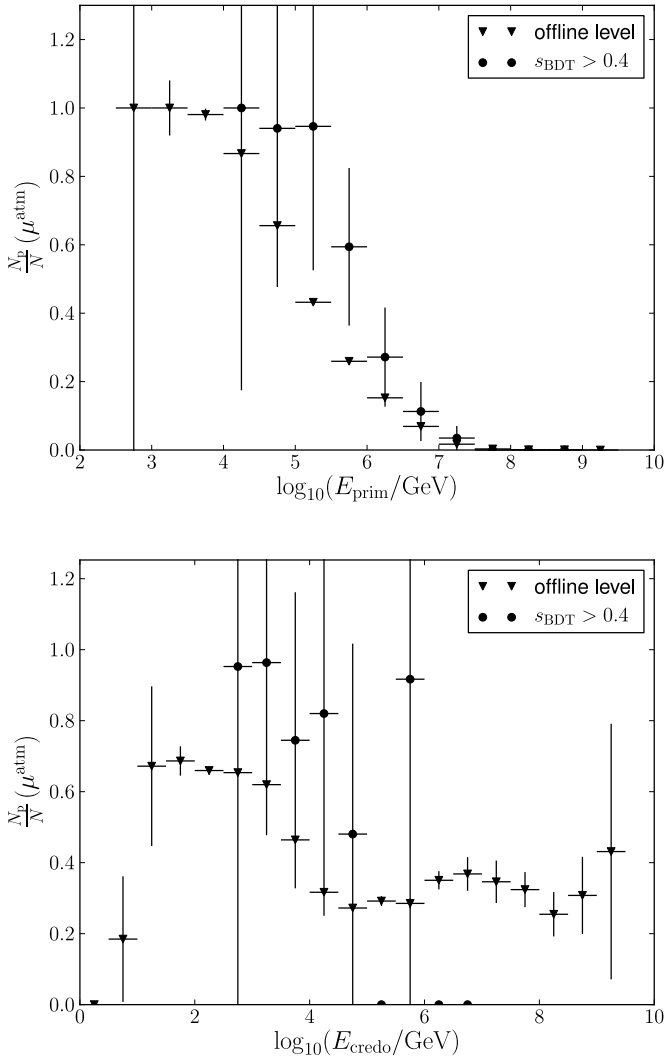

Figure 6.9: Composition of the cosmic ray simulation: The fraction of events generated by protons relative to all nuclei over the primary energy (top) and the reconstructed energy (bottom) at the offline filter level (triangles) and after a (lose) BDT cut (circles). For the primary energy the distributions follows the the exponential cut off for protons given in the Hörandel model[Hör03]. The increase of the proton fraction after the BDT cut indicates, that events from protons are harder to distinct from cascades compared to other primaries. The available statistics for protons that would survive the energy cut, appears to be under-sampled.

Table 6.4: Effect of neutrino cross sections: Predicted event numbers for the different neutrino fluxes after the final cuts. The CSS$^{\text{CS08}}$ cross sections are compared to the CTEQ5$^{\text{L}^+00}$ cross sections that were used as the default in this analysis.

model	ν_e^{atm}	ν_e^{prompt}	$\nu_e E^{-2}$
CTEQ5	0.065	0.38	47.1
CSS	0.051	0.34	43.0
uncertainty	±18.3 %	±9.4 %	±8.8 %

The average shower height and thus the number and energy of atmospheric muons change with air pressure over the season. The simulation is based on atmosphere data, as they are expected during October, well between the extreme conditions of summer or winter. For the estimate of the seasonal variation of atmospheric muons the maximal and minimal rate from Fig. 5.1 were compared to the October rate. From this comparison the systematic uncertainty of the muon flux due to seasonal variation is estimated to be $\pm^{24.0}_{8.9}$ %. The uncertainty of the atmospheric neutrino flux is expected to be less than 5 %.[Gai11]

Flasher studies[Stöß10] suggest a systematic shift of the reconstructed energy. The effect on the atmospheric and signal neutrino events was predicted by changing the energy cut by ±20 % and result in an uncertainty of $\pm^{37.5}_{23.8}$ % respectively ±7.5 %.

Finally the used[4] CTEQ5$^{\text{L}^+00}$ cross sections were compared to CSS$^{\text{CS08}}$ cross sections (see Tab. 5.1). For this an electron neutrino data set simulated with CSS cross sections was weighted to the different neutrino fluxes and the cuts were applied. The predicted event numbers are listed in Tab. 6.4. This results in an uncertainty of 8.8 % for the E^{-2} signal and 18.3 % for the atmospheric neutrino flux.

6.3 Final Sensitivity and Unblinding Results

The sensitivity used for the optimization process in Sec. 5.2.3 has not included the systematical error, because an estimation of the uncertainty in every optimization step would be needed. Now the systematic uncertainties could be evaluated after the final cut selection. To include the systematic and statistic uncertainty the method from Rolke et al. [RLC05] is used. If folds the Poisson distribution used to model the measurement process of signal and background with a Gaussian of the size of the uncertainty, in order to calculate a limit or the sensitivity, i. e. the average upper limit. Using the expected number of signal and background events (see Tab. 6.5, scenario a)) leads to a sensitivity on a pure electron neutrino flux of

$$\left\langle \Phi^e_{\text{lim}} \right\rangle = 3.1 \cdot 10^{-8}\, E^{-2}\, \frac{\text{GeV}}{\text{s sr cm}^2}. \tag{6.5}$$

[4] Note that ν_τ was only available with CSS cross sections

Table 6.5: Limits for different scenarios: While it was decided before unblinding to exclude the burn sample (332 d data), use no containment cut (Cont.) and not to consider prompt (Pr.) signal $\nu_{e,\mu}^{\text{prompt}}$ as background (a), other combinations are possible. Including the burn sample results in 367 d life time, the burn sample alone (i) has 35 d. Presented are the expected number of signal N_{sig} for a hypothetical E^{-2} all flavor flux of $\Phi E^2 = 3 \times 5 \cdot 10^{-7} \frac{\text{GeV}}{\text{s sr cm}^2}$ flux and background events N_{BG} with statistical and systematical error, the observed events N_{obs} and the all flavor limit $\Phi_{\text{lim}} E^{-2}$.

No.	Data	Cont.	Pr.	$N_{\text{sig}} \pm \text{stat}$ $\pm \text{sys}$	$N_{\text{BG}} \pm \text{stat}$ $\pm \text{sys}$	N_{Obs}	$\Phi_{\text{lim}} E^{-2}\, 10^8$ $[\frac{\text{GeV}}{\text{s sr cm}^2}]$
a)	332 d	no	no	$119 \pm 2 \pm 22$	$0.72 \pm 0.28 \pm^{1.54}_{0.49}$	4	9.5
b)	367 d	no	no	$131 \pm 2 \pm 24$	$0.80 \pm 0.31 \pm^{1.70}_{0.55}$	5	10.1
c)	332 d	no	yes	$119 \pm 2 \pm 22$	$1.20 \pm 0.28 \pm^{1.56}_{0.57}$	4	8.9
d)	367 d	no	yes	$131 \pm 2 \pm 24$	$1.32 \pm 0.31 \pm^{1.72}_{0.63}$	5	9.5
e)	332 d	yes	no	$103 \pm 2 \pm 19$	$0.24 \pm 0.02 \pm^{0.21}_{0.14}$	0	2.6
f)	367 d	yes	no	$114 \pm 2 \pm 21$	$0.26 \pm 0.02 \pm^{0.23}_{0.15}$	1	4.5
g)	332 d	yes	yes	$103 \pm 2 \pm 19$	$0.67 \pm 0.02 \pm^{0.31}_{0.29}$	0	1.9
h)	367 d	yes	yes	$114 \pm 2 \pm 21$	$0.74 \pm 0.02 \pm^{0.34}_{0.32}$	1	3.8

Table 6.6: The events surviving the final level. Given are the run number, event number, BDT score and reconstructed energy followed by the reference to the event displays. Note, that due to correlation of reconstructed energy and position the energies are high, as the events are reconstructed outside the detector (see Fig. 6.10).

No.	Run No.	Event No.	s_{BDT}	$\log_{10} \frac{E_{\text{credo}}}{\text{GeV}}$	Fig.
BS	111780	29420816	0.485	5.34	5.29
(i)	110889	20739688	0.482	5.21	6.11(a), 6.11(b)
(ii)	111003	7133036	0.474	5.60	6.11(c), 6.11(d)
(iii)	111432	12259089	0.474	5.33	6.12(a), 6.12(b)
(iv)	112416	23470164	0.470	6.46	6.12(c), 6.12(d)

The sensitivity for an all flavor flux with a flavor ratio of 1 : 1 : 1 is worse, as the effective area for muon neutrinos is lower (see Sec. 5.3, Fig. 5.31):

$$\left\langle \Phi^{e,\mu,\tau}_{\text{lim}} \right\rangle = 4.4 \cdot 10^{-8}\, E^{-2}\, \frac{\text{GeV}}{\text{s sr cm}^2}. \tag{6.6}$$

After unblinding four events in the 332 d sample survived the cuts. The BDT and energy values are given in Tab. 6.6, event displays are shown in Fig. 6.11 and 6.12. All these events have their first hits in DOMs at the border of the detector and are thus similar to the events predicted from the atmospheric muon simulation (see Fig. 5.26). The reconstruction algorithm assigns vertices relatively far out of the detector, as shown in Fig. 6.10. As reconstructed distance to the detector and energy are correlated[Mid08], the reconstructed energy is higher, than one would expect for a contained cascade with the same number of measured photons. Therefore the event from the burn sample (BS) has a lower reconstructed energy than event number (IV), although more DOMs are hit as visible in Fig. 5.29 and Fig. 6.12(d). In order to estimate, if the measurement is in agreement with a background-only hypothesis, one calculates the p-value $p(\geq n|\mu)$, i. e. the Poisson expectation of measuring n or more events for an expectation value of μ. The four observed events yield a p-value of $p(\geq 4|0.72) = 6.34 \cdot 10^{-3}$. However, systematic uncertainties are rather large: the p-value for background plus systematic error is $p(\geq 4|2.26) = 0.193$, so that this occurrence is not incompatible with the background-only hypothesis.

While after unblinding, obviously background from atmospheric muons is remaining, it was decided before to base the calculation of the results on

- 332 d experimental without the burn sample,
- the conventional flux for the atmospheric neutrino prediction,
- no containment cuts.

To calculate the limit including the statistical and systematical uncertainties the same approach as for the sensitivity calculation, the method from Rolke et al. [RLC05] is used. The limit for a pure electron neutrino flux is

$$\Phi^{e}_{\text{lim}} = 6.6 \cdot 10^{-8}\, E^{-2}\, \frac{\text{GeV}}{\text{s sr cm}^2}. \tag{6.7}$$

For an assumed 1 : 1 : 1 neutrino ratio the all flavor limit is

$$\Phi^{e,\mu,\tau}_{\text{lim}} = 9.5 \cdot 10^{-8}\, E^{-2}\, \frac{\text{GeV}}{\text{s sr cm}^2}. \tag{6.8}$$

Analog to the sensitivities (see Eq. (6.5) and (6.6)) the all flavor limit is a bit worse than the limit for a pure electron neutrino flux, caused by the worse performance of the analysis for muon neutrinos. The all flavor limits for different scenarios are listed in Tab. 6.5. The scenarios b), d), f) and h) include the burn sample, as it is simply a larger amount of measured data, though it was already used for the development of the analysis. A containment

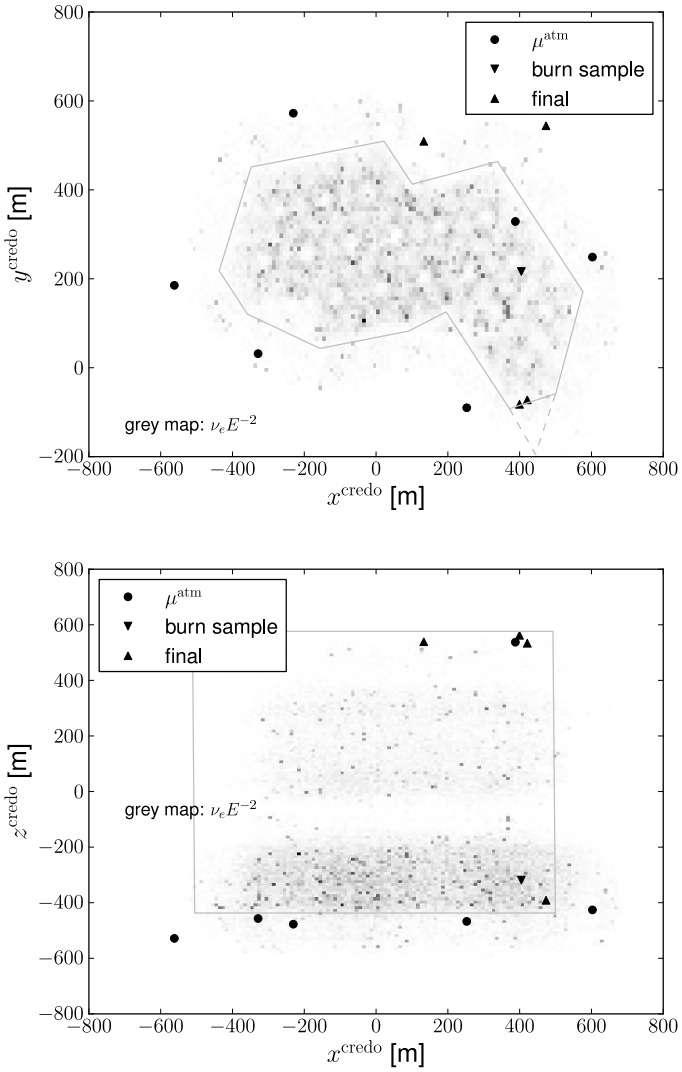

Figure 6.10: The *x*-*y* (top) and the *x*-*z*-projection (bottom) shows the position of the remaining events as in Fig. 5.25. Additionally the four final events are shown (upward triangle). Two of them are reconstructed far outside the detector, the other two are on the same corner close to string 21 (see Fig. 3.1). The solid gray line shows the containment area.

cut[5] would remove events outside the detector, for which the reconstruction has a worse resolution and that are also more uncertain in the simulation[6](scenarios e) to h)). While uncertain in itself one could consider the prompt component of atmospheric neutrino flux as background, as the search actually aims for astrophysical neutrinos (scenarios c), d), g) and h)). Here the scenario g) – 332 d of data, applying the containment cut and including prompt atmospheric neutrino flux predictions into the background estimation gives the lowest limit, $1.9 \cdot 10^{-8}\, E^{-2}\,\mathrm{GeV\,s^{-1}\,sr^{-1}\,cm^{-2}}$. Also of interest are the scenarios f) and h), where the containment cut is applied and the burn sample data included. In this case one cascade-like event from the burn sample survives the cuts (see Sec. 5.3). The observation of one event is compatible to both a background hypothesis with the prompt component not included f) and one including the prompt component. The p-values are $p_{\mathrm{f)}} = p(\geq 1|0.26) = 0.23$ and $p_{\mathrm{h)}} = p(\geq 1|0.74) = 0.52$. This shows, that this analysis is not sufficient to decide between a pure conventional neutrino flux and one including a prompt component. This may be achieved by other analyses such as from E. Middell[Mid11].

To compare the analysis with the models described in Sec. 2.2 and other existing limits the all flavor limit is drawn in Fig. 6.14. The width in energy is given by the central interval in which 90 % of the passing signal are located (see Sec. 5.3):

$$E^{90\,\%} = \left\{ E_\nu \left| 4.95 < \log_{10} \frac{E_\nu}{\mathrm{GeV}} < 7.45 \right. \right\} \tag{6.9}$$

The energy region, for which the experiment is sensitive is also visible in the differential limit[Hul11], i.e. the limits for fluxes

$$\Phi_{E_0,2\Delta}(E) = \Phi_0 E^{-2} \chi_{[\log_{10} E_0 - \Delta, \log_{10} E_0 + \Delta]}(\log_{10} E) \tag{6.10}$$

$$\text{with } \chi_I(x) = \begin{cases} 1 & \text{if} \quad x \in I \\ 0 & \text{otherwise,} \end{cases} \tag{6.11}$$

were the flux width $2\Delta = 0.1$ is chosen here. The differential limit is shown in Fig. 6.13. The differential limit steeply falls until the full width of the fluxes is above the energy cut and the minimal limit is reached at about 300 TeV. Then the differential limit grows again with another local minimum from the Glashow resonance strongly smeared out by the finite flux width.

[5]Containment: the reconstructed vertex is inside a volume spanned by the strings, with string 21 removed as it would result in a sharp corner. The volume is indicated in Fig. 6.10.

[6]The light propagation over a longer distance makes these events more sensitive to the optical properties of the ice.

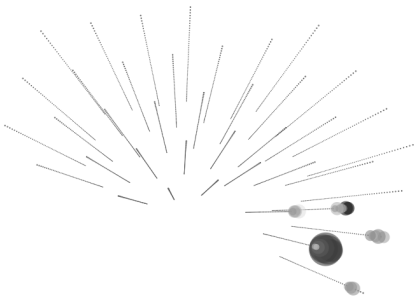

(a) Event (i), *x*-*y* projection

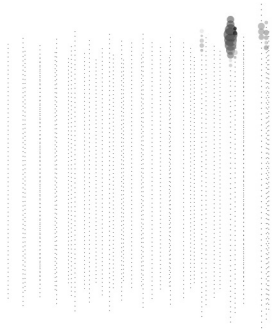

(b) Event (i), *x*-*z* projection

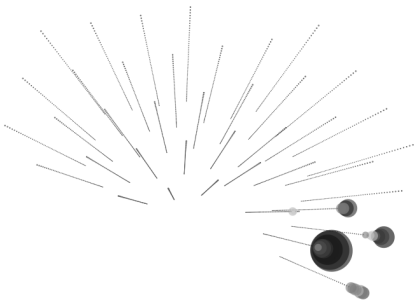

(c) Event (ii), *x*-*y* projection

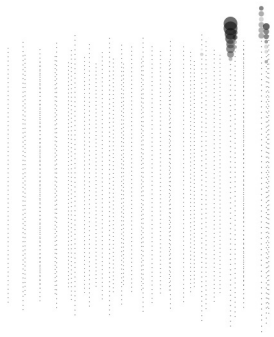

(d) Event (ii), *x*-*z* projection

Figure 6.11: Final events (i) and (ii): Hit DOM are filled, dark for early, lighter for late hits, the size is proportional to the logarithm of the amplitude and anti-proportional to the distance of the projection plane. Both events are at the top and in the same corner of the detector.

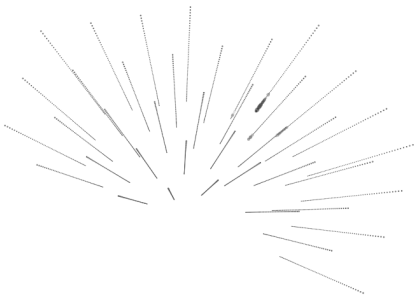

(a) Event (iii), *x*-*y* projection

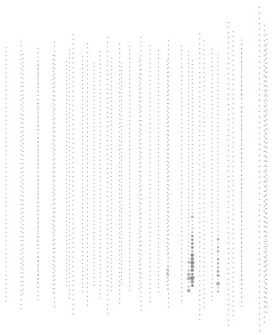

(b) Event (iii), *x*-*z* projection

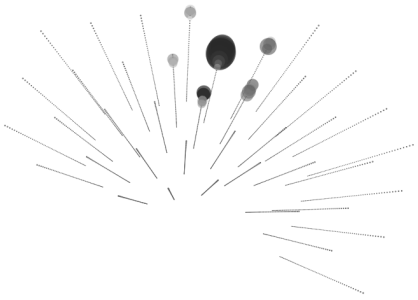

(c) Event (iv), *x*-*y* projection

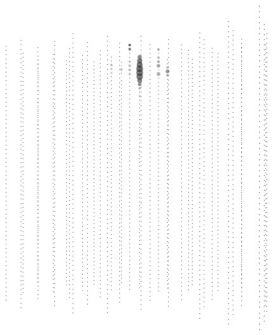

(d) Event (iv), *x*-*z* projection

Figure 6.12: Final events (iii) and (iv): Hit DOM are filled, dark for early, lighter for late hits, the size is proportional to the logarithm of the amplitude and anti-proportional to the distance of the projection plane. Both events are outside the detector. Event (iii) is the only final event not at the top of the detector.

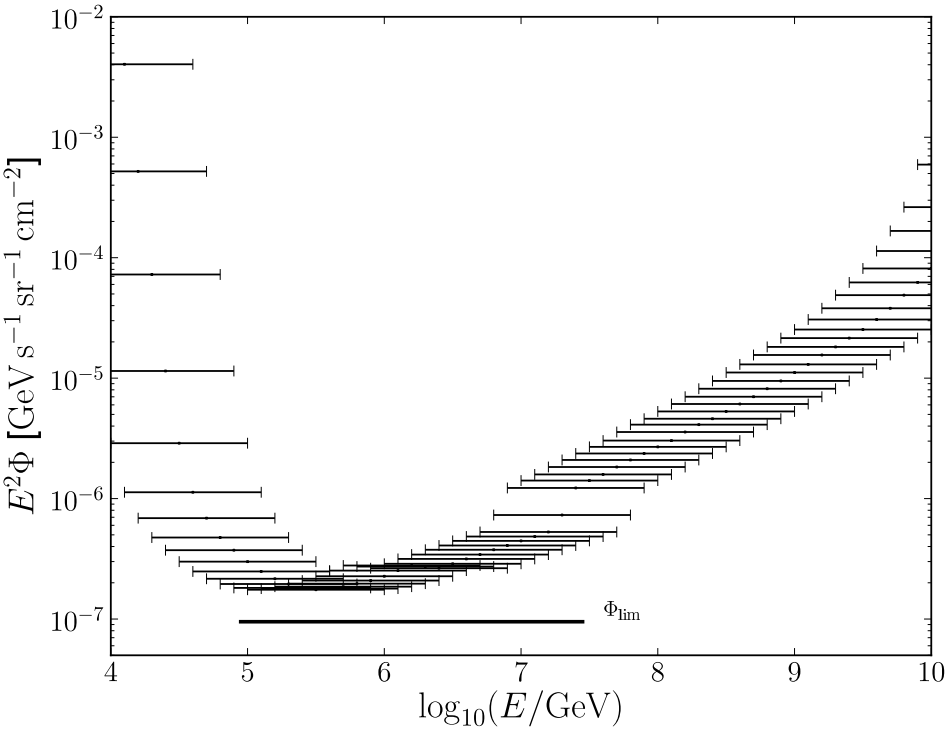

Figure 6.13: The differential limit calculated for a bin width of one energy decade. A dip from the Glashow resonance is visible in the P*e*V to 100 P*e*V region. The integrate limit with its 90 % energy interval is shown as solid line.

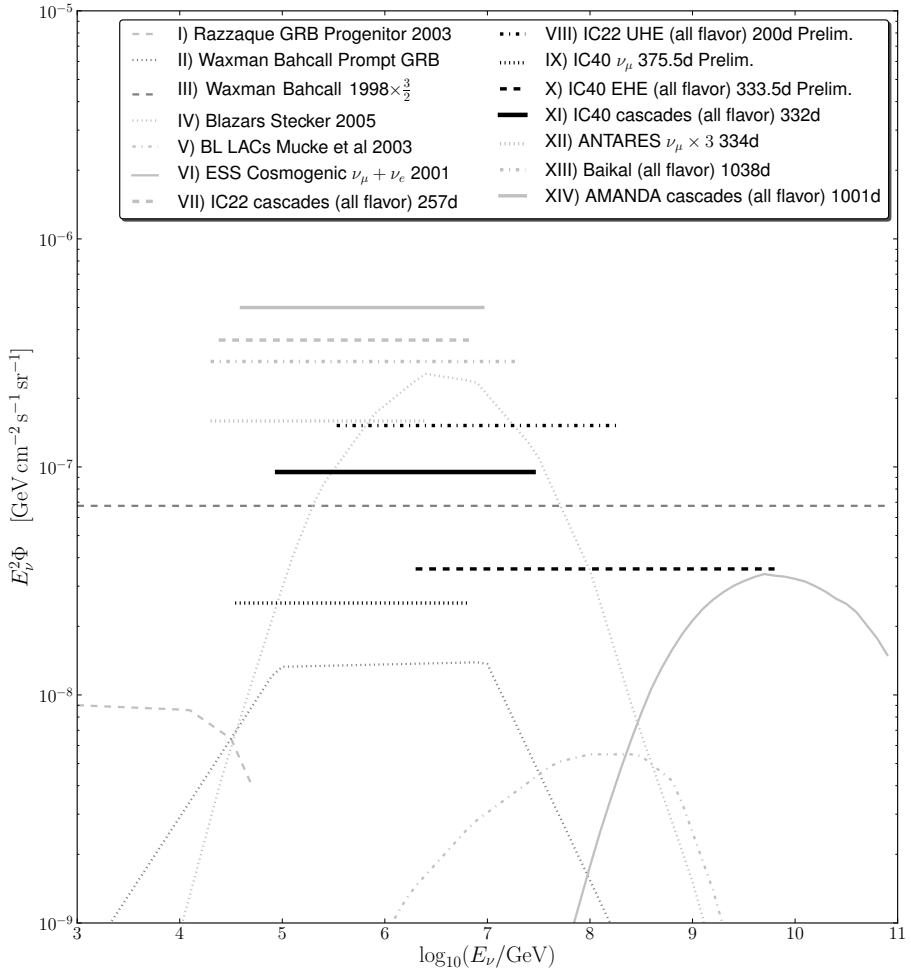

Figure 6.14: Limits and flux predictions for an all flavor diffuse flux: Thick horizontal lines indicate the limits from different neutrino telescopes (XIV Antares[A+11f], XIII Baikal[Df09], XII AMANDA[A+11e]) and for different IceCube analysis. This work is the thick solid line (XI). If no all flavor limit was available for an analysis, its limit for the muon neutrino flux was multiplied by three. Note that the distance to the corresponding IC22 cascade search (VII)[IAA+11] is about the same as between the IC40 EHE (X)[Joh11] and the IC22 UHE search (VIII)[A+11b]. The current best limit is given by the IC40 diffuse search using muon neutrinos (IX)[A+11a]. The theoretical models are represented through thin gray lines (references: I - III[RMW03], IV[Ste05], V[MPE+03], VI[ESS01], see Sec. 2.2.1).

7 Summary

The cosmic ray flux consists of charged particles with energies reaching beyond $10^{20}\,eV$. The sources are still unknown, although different candidates and models for a possible acceleration process exist. These models also predict an extra-terrestrial neutrino flux with an E^{-2} energy spectrum, which has not been observed, yet. The goal of this thesis was to search for this flux using neutrino-induced cascades in the IceCube neutrino detector. Cascades provide the possibility of a reasonable energy measurement and a signature, that can be distinguished from muonic background events. These properties allow a high background suppression, ideal for a full-sky search of a weak, diffuse flux. This is in contrast to point-source searches using the track-like signal pattern of neutrino induced muons. In the diffuse search of cascades a few hundred signal events have to be distinguished from a background of about 10^{10} events, mostly from atmospheric muons. In this thesis an analysis technique to measure the diffuse flux using neutrino induced cascades was developed.

As detector the IceCube neutrino telescope was used. IceCube consists of 86×60 digital optical modules (DOM), each housing a PMT. In total a volume of one cubic kilometer of clear ice is instrumented. The deployment was finished in 2010. During the years 2008 and 2009 about half of the detector was deployed and operational. Data from this period – in total an up-time of 367 d – was used for this work.

The optical properties, i. e. scattering and absorption length, of the ice are crucial for reconstructing event parameters from the measured signal. These properties were obtained using LEDs – so called flashers, which are part of the DOMs. It was shown that the scattering length is small in shallower ice due to bubbles and at greater depth dust layers decrease both scattering and absorption length. These dust layers are connected to geological events as ice ages and volcanic activity. However, below 2 100 m the ice is very clear.

Simple event properties to distinguish spherical, local light pattern from a light pattern originating from an extended track were used to separate signal from background. As a final reconstruction a sophisticated likelihood reconstruction was used, including the optical properties of the ice. In order to avoid biases introduced in the event selection by the experimenter a blindness policy was followed. All cuts were developed using Monte Carlo simulation data and only 10 % of the measured data were used to verify the simulations.

For the simulation cascades were parameterized, therefore it was not necessary to simulate the full shower development. The parameterization includes the extension of the cascade as well as the production of muons in hadronic cascades. For the latter a simple analytic model showed, that the energy spectrum of muons produced in hadronic cascades can be described by a power law. The amplitude and spectral index were obtained from CORSIKA simulations.

The analysis consisted of several cut and reconstruction levels, which successively increased the expected signal fraction in the surviving data: In a first step filter algorithms

with low CPU requirements, based on simple geometrical principles were used in order to reduce the data volume such that the data could be transferred from the South Pole to the north via satellite. A further reduction of the data volume was achieved with additional cuts based on a simple likelihood reconstruction, that assumes for all depth the same optical properties. This reduction allowed to perform a CPU intensive likelihood algorithm incorporating a detailed, depth dependent model of the optical properties of the ice. At the final level ten variables are combined to a single quality criterion using a boosted decision tree (BDT). Cuts on the BDT value and the reconstructed energy were optimized for sensitivity on the signal flux. These cuts are sufficient to reduce the expected background to $0.72 \pm 0.28 \pm^{1.54}_{0.49}$ events in 332 d. This background includes six simulated atmospheric muon events, that survive all cuts. These events are located at the corners of the detector and reconstructed far away from the detector. A containment cut was not used as the background expectation was found reasonably low. A single event from 10 % of data, that was used for verifying the simulation, also survived the cuts. It is contained in the detector and the event shows no indication that it could be a bremsstrahlung-cascade from an atmospheric muon.

The analysis was validated using the DOM's flashers, which are an artificial light source with a similar light pattern to that of cascades. In a region below 2 100 m these flasher events passed all cuts of the analysis. In other parts of the detector the efficiency was low. It was found that the analysis has a low efficiency for events very close to string positions.

Systematic uncertainties, quoted above, were studied with different kinds of MC and a high uncertainty of $\pm^{322}_{100}$ % on the prediction of atmospheric muon flux was found. Including the systematic error an all flavor sensitivity of $4.4 \cdot 10^{-8}\, E^{-2}\, \mathrm{GeV\,s^{-1}\,sr^{-1}\,cm^{-2}}$ was calculated. After unblinding, four additional events were found. They are comparable to the corner events in the background prediction and are also reconstructed to the outside of the detector. Due to the high systematic uncertainty the observation is still in agreement with a background-only hypothesis. As a result, a limit on the all flavor neutrino flux of $9.5 \cdot 10^{-8}\, E^{-2}\, \mathrm{GeV\,s^{-1}\,sr^{-1}\,cm^{-2}}$ was derived. So far this is the best limit for en extra-terrestrial E^{-2} neutrino flux, that is only based on cascades. However, the analysis for ultra high energies[Joh11], including muons in the analysis and the muon diffuse search[A+11a] provide a significantly lower limit of $2.3 \cdot 10^{-8}\, E^{-2}\, \mathrm{GeV\,s^{-1}\,sr^{-1}\,cm^{-2}}$ respectively $2.5 \cdot 10^{-8}\, E^{-2}\, \mathrm{GeV\,s^{-1}\,sr^{-1}\,cm^{-2}}$. This is expected, as the detector has a bigger effective volume for muon neutrinos and, in the case of the high energy analysis, the background from atmospheric muons is lower at higher energies.

Future analyses using a larger detector configuration of IceCube can make use of outer strings as a veto enforcing containment. Such a containment could help to reduce the systematic uncertainties and as such make the analysis more robust. This analysis suffered from the systematic and the statistic error of the used MC simulation. Improved understanding of the optical properties of the ice and more detailed, accurate simulation software may also help reducing the systematic error.

So far, the atmospheric electron neutrino flux is not yet unambiguously detected. However, already now the IC40 analyses,[Mid11,A+11d] which are currently developed in parallel to the work presented here, may have the sensitivity to detect atmospheric electron neutrinos in a sizable number.

Bibliography

This bibliography includes some IceCube internal resources, like Internal Reports and the IceCube Wiki. These are not publicly available. In cases where work not done by the author has not been documented in any other way, it was decided to list these references since they are the most precise documentation available. If access is required, please refer to a member of the IceCube collaboration.

[A+00] Andres, E.; et al.: The AMANDA neutrino telescope: principle of operation and first results. In: *Astroparticle Physics*, volume 13:pp. 1–20, March 2000. doi:10.1016/S0927-6505(99)00092-4. arXiv:astro-ph/9906203.

[A+01] Ahrens, J.; et al.: IceCube Preliminary Design Document. http://www.icecube.wisc.edu/science/publications/pdd/pdd.pdf, October 2001. Retrieved 2011-07-12.

[A+06a] Achterberg, A.; et al.: On the selection of AGN neutrino source candidates for a source stacking analysis with neutrino telescopes. In: *Astroparticle Physics*, volume 26:pp. 282–300, November 2006. doi:10.1016/j.astropartphys.2006.06.012. arXiv:astro-ph/0609534.

[A+06b] Ackermann, M.; et al.: Optical properties of deep glacial ice at the South Pole. In: *Journal of Geophysical Research (Atmospheres)*, volume 111(D10):pp. 13203–+, July 2006. doi:10.1029/2005JD006687.

[A+08] Abraham, J.; et al.: Upper limit on the cosmic-ray photon flux above 10^{19} eV using the surface detector of the Pierre Auger Observatory. In: *Astroparticle Physics*, volume 29:pp. 243–256, May 2008. doi:10.1016/j.astropartphys.2008.01.003. 0712.1147.

[A+09] Abbasi, R.; et al.: The IceCube data acquisition system: Signal capture, digitization, and timestamping. In: *Nuclear Instruments and Methods in Physics Research A*, volume 601:pp. 294–316, April 2009. doi:10.1016/j.nima.2009.01.001. 0810.4930.

[A+10] Abbasi, R.; et al.: Calibration and characterization of the IceCube photomultiplier tube. In: *Nuclear Instruments and Methods in Physics Research A*, volume 618:pp. 139–152, June 2010. doi:10.1016/j.nima.2010.03.102. 1002.2442.

[A+11a] Abbasi, R.; et al.: A Search for a Diffuse Flux of Astrophysical Muon Neutrinos with the IceCube 40-String Detector. In: *ArXiv e-prints*, April 2011. 1104.5187.

[A+11b] Abbasi, R.; et al.: A Search for UHE Tau Neutrinos with IceCube. https://docushare.icecube.wisc.edu/dsweb/Get/Document-56847/paper-IC22-UHE-Diffuse.pdf, 2011. In preparation, retrieved 2011-07-12.

[A+11c] Abbasi, R.; et al. (IceCube Collaboration): Measurement of the atmospheric neutrino energy spectrum from 100 GeV to 400 TeV with IceCube. In: *Phys. Rev. D*, volume 83(1):p. 012001, Jan 2011. doi:10.1103/PhysRevD.83.012001.

[A+11d] Abbasi, R.; et al.: Search for astrophysical neutrino-induced cascades using IceCube-40. In: *Proceedings 32. ICRC*, 0759. 2011. In preparation.

[A+11e] Abbasi, R.; et al.: Search for neutrino-induced cascades with five years of AMANDA data. In: *Astroparticle Physics*, volume 34:pp. 420–430, January 2011. doi:10.1016/j.astropartphys.2010.10.007.

[A+11f] Aguilar, J. A.; et al.: Search for a diffuse flux of high-energy ν with the ANTARES neutrino telescope. In: *Physics Letters B*, volume 696:pp. 16–22, January 2011. doi:10.1016/j.physletb.2010.11.070. 1011.3772.

[AJY00] Athar, H.; Jeżabek, M.; Yasuda, O.: Effects of neutrino mixing on high-energy cosmic neutrino flux. In: *PRD*, volume 62(10):pp. 103007–+, November 2000. doi:10.1103/PhysRevD.62.103007. arXiv:hep-ph/0005104.

[AS09] Akhmedov, E. K.; Smirnov, A. Y.: Paradoxes of neutrino oscillations. In: *Physics of Atomic Nuclei*, volume 72:pp. 1363–1381, August 2009. doi:10.1134/S1063778809080122. 0905.1903.

[B+10] Bay, R. C.; et al.: South pole paleowind from automated synthesis of ice code records. In: *Journal of Geophysical Research (Atmospheres)*, volume 115(D14126), 2010. doi:10.1029/2009JD013741.

[BBH+03] Beacom, J. F.; Bell, N. F.; Hooper, D.; Pakvasa, S.; Weiler, T. J.: Measuring flavor ratios of high-energy astrophysical neutrinos. In: *PRD*, volume 68(9):pp. 093005–+, November 2003. doi:10.1103/PhysRevD.68.093005. arXiv:hep-ph/0307025.

[Bec08] Becker, J. K.: High-energy neutrinos in the context of multimessenger astrophysics. In: *Phys.Rep*, volume 458:pp. 173–246, March 2008. doi:10.1016/j.physrep.2007.10.006. 0710.1557.

[BEH09] Blümer, J.; Engel, R.; Hörandel, J. R.: Cosmic rays from the knee to the highest energies. In: *Progress in Particle and Nuclear Physics*, volume 63:pp. 293–338, October 2009. doi:10.1016/j.ppnp.2009.05.002. 0904.0725.

[Ber96] Berezhko, E. G.: Maximum energy of cosmic rays accelerated by supernova shocks. In: *Astroparticle Physics*, volume 5:pp. 367–378, October 1996. doi:10.1016/0927-6505(96)00037-0.

[Ber10] Berghaus, Patrick: First Look at SLC Hits as InIce Veto. talk: http://w3.iihe.ac.be/indico/materialDisplay.py?contribId=45&sessionId=47&materialId=slides&confId=123, September 2010. Retrieved 2011-07-12.

[BGL+04] Barr, G. D.; Gaisser, T. K.; Lipari, P.; Robbins, S.; Stanev, T.: Three-dimensional calculation of atmospheric neutrinos. In: *PRD*, volume 70(2):pp. 023006–+, July 2004. doi:10.1103/PhysRevD.70.023006. arXiv:astro-ph/0403630.

[BRGS06] Barr, G. D.; Robbins, S.; Gaisser, T. K.; Stanev, T.: Uncertainties in atmospheric neutrino fluxes. In: *PRD*, volume 74(9):pp. 094009–+, November 2006. doi:10.1103/PhysRevD.74.094009. arXiv:astro-ph/0611266.

[BSMM01] Bronstein, I.N.; Semendjajew, K.A.; Musiol, G.; Mühlig, H.: *Taschenbuch der Mathematik*. Harri Deutsch, Frankfurt am Main, 5th edition, 2001.

[C+10a] Chirkin, Dmitry; et al.: Study of ice transparency with IceCube flashers. http://icecube.wisc.edu/~dima/work/WISC/ppc/fit/paper/a.pdf, 2010. Retrieved 2011-07-12.

[C+10b] Chirkin, Dmitry; et al.: Study of ice transparency with IceCube flashers. http://icecube.wisc.edu/~dima/work/WISC/ppc/spice/paper/a.pdf, 2010. Retrieved 2011-07-12.

[Chi] Chirkin, Dmitry: *Feature Extraction of IceCube Waveforms*. Lawrence Berkley National Laboratory. http://www.ifh.de/~kislat/www/icerec/docs/docs_material/FE.pdf, retrieved 2011-07-12.

[Chi03] Chirkin, Dmitry Aleksandrovich: *Cosmic Ray Energy Spectrum Measurement with the Antarctic Muon and Neutrino Detector Array (AMANDA)*. Ph.D. thesis, University of California at Berkeley, 2003.

[Chi04] Chirkin, D.: Fluxes of Atmospheric Leptons at 600 GeV - 60 TeV. In: *ArXiv High Energy Physics - Phenomenology e-prints*, July 2004. arXiv:hep-ph/0407078.

[Chi10] Chirkin, Dmitry: Fitting the 6-parameter ice model to the flasher data. http://icecube.wisc.edu/~dima/work/WISC/ppc/fit/, 2010. Retrieved 2011-07-12.

[CR04] Chirkin, D.; Rhode, W.: Propagating leptons through matter with Muon Monte Carlo (MMC). In: *ArXiv High Energy Physics - Phenomenology e-prints*, July 2004. arXiv:hep-ph/0407075.

[CRH+56] Cowan, C. L., Jr.; Reines, F.; Harrison, F. B.; Kruse, H. W.; McGuire, A. D.: Detection of the Free Neutrino: A Confirmation. In: *Science*, volume 124:pp. 103–104, July 1956. doi:10.1126/science.124.3212.103.

[CS08] Cooper-Sarkar, A.; Sarkar, S.: Predictions for high energy neutrino cross-sections from the ZEUS global PDF fits. In: *Journal of High Energy Physics*, volume 1:pp. 75–+, January 2008. doi:10.1088/1126-6708/2008/01/075. 0710.5303.

[D+07] Desiati, Paolo; et al.: Weights in nugen Simulation Data. http://wiki.icecube.wisc.edu/index.php/Weights_in_nugen_Simulation_Data, July 2007. Retrieved 2011-07-12.

[D'A09a] D'Agostino, Michelangelo: Effective Livetimes in Weighted CORSIKA. https://internal.icecube.wisc.edu/reports/data/icecube/2009/02/001/icecube_200902001_v2.pdf, February 2009. Retrieved 2011-07-12.

[D'A09b] D'Agostino, Michelangelo Vincent: *First Evidence For Atmosperic Neutrino-Induced Cascades with the IceCube Detector*. Ph.D. thesis, University of California, Berkeley, October 2009.

[Df09] Dzhilkibaev, Z. .; for the Baikal Collaboration: Search for a diffuse flux of high-energy neutrinos with the Baikal neutrino telescope NT200. In: *ArXiv e-prints*, September 2009. 0909.5562.

[DV09] Desiati, Paolo; Vélez, Juan Carlos Díaz: CORSIKA weighting scheme for IceCube. https://internal.icecube.wisc.edu/reports/data/icecube/2009/01/003/icecube_200901003_v1.pdf, Jannuary 2009.

[Edw92] Edwards, A. W. F.: *Likelihood*. The Johns Hopkins University Press, expanded edition, October 1992.

[ERS08] Enberg, R.; Reno, M. H.; Sarcevic, I.: Prompt neutrino fluxes from atmospheric charm. In: *PRD*, volume 78(4):pp. 043005–+, August 2008. doi:10.1103/PhysRevD.78.043005. 0806.0418.

[ESS01] Engel, R.; Seckel, D.; Stanev, T.: Neutrinos from propagation of ultrahigh energy protons. In: *PhysRevD*, volume 64(9):pp. 093010–+, November 2001. doi:10.1103/PhysRevD.64.093010. arXiv:astro-ph/0101216.

[F+09] Feusels, T.; et al.: Reconstruction of IceCube coincident events and study of composition-sensitive observables using both the surface and deep detector. In: *ArXiv e-prints*, December 2009. 0912.4668.

[FC98] Feldman, G. J.; Cousins, R. D.: Unified approach to the classical statistical analysis of small signals. In: *PhRvD*, volume 57:pp. 3873–3889, April 1998. doi:10.1103/PhysRevD.57.3873. arXiv:physics/9711021.

[Fer49] Fermi, E.: On the Origin of the Cosmic Radiation. In: *Physical Review*, volume 75:pp. 1169–1174, April 1949. doi:10.1103/PhysRev.75.1169.

[FH12] F. Hess, V.: Über Beobachtungen der durchdringenden Strahlung bei sieben Freiballonfahrten. In: *Physikalische Zeitschrift*, volume 13:pp. 1084–1091, November 1912.

[Gai90] Gaisser, T. K.: *Cosmic Rays and Particle Physics*. Cambridge University Press, Cambridge, 1990.

[Gai11] Gaisser, Tom: private communication, January 2011.

[GBH08] Grullon, Sean; Boersma, David J.; Hill, Gary: Photonics-based Log-Likelihood Reconstruction in IceCube. http://internal.icecube.wisc.edu/reports/data/icecube/2008/07/001/icecube_200807001_v3.pdf, July 2008. Retrieved 2011-07-12.

[GK05] Gazizov, A.; Kowalski, M.: ANIS: High energy neutrino generator for neutrino telescopes. In: *Computer Physics Communications*, volume 172:pp. 203–213, November 2005. doi:10.1016/j.cpc.2005.03.113. arXiv:astro-ph/0406439.

[GK10] Gerhardt, L.; Klein, S. R.: Electron and photon interactions in the regime of strong Landau-Pomeranchuk-Migdal suppression. In: *PRD*, volume 82(7):pp. 074017–+, October 2010. doi:10.1103/PhysRevD.82.074017. 1007.0039.

[GQRS96] Gandhi, Raj; Quigg, Chris; Reno, Mary Hall; Sarcevic, Ina: Ultrahigh-energy neutrino interactions. In: *Astroparticle Physics*, volume 5(2):pp. 81 – 110, 1996. ISSN 0927-6505. doi:DOI:10.1016/0927-6505(96)00008-4. URL http://www.sciencedirect.com/science/article/B6TJ1-3VRVT8H-1/2/2b2c37e04d0320d0372846664919ad0e.

[Grea] Greene, Michael: CFirst Documentation. doxygen: http://www.ifh.de/~kislat/www/icerec/docs/V03-03-01/doxygen/cfirst/index.html. Retrieved 2011-07-12.

[Greb] Greene, Michael: CscdLlh Documentation. doxygen http://www.ifh.de/~kislat/www/icerec/docs/V03-03-01/doxygen/cscd-llh/index.html. Retrieved 2011-07-12.

[Gre66] Greisen, Kenneth: End to the Cosmic-Ray Spectrum? In: *Phys. Rev. Lett.*, volume 16(17):pp. 748–750, Apr 1966. doi:10.1103/PhysRevLett.16.748.

[Gru] Grullon, Sean: Tensor of Inertia code documentation. doxygen: http://www.ifh.de/~kislat/www/icerec/docs/V03-03-01/doxygen/tensor-of-inertia/index.html. Retrieved 2011-07-12.

[GS64] Ginzburg, V. L.; Syrovatskii, S. I.: *The Origin of Cosmic Rays*. Macmillan, 1964.

[H+07] Hanson, Kael; et al.: configuration-parameters. https://docushare.icecube.wisc.edu/dsweb/Get/Document-44936/configuration-parameters.pdf, November 2007. Retrieved 2011-07-12.

[Hei54] Heitler, W.: *The Quantum Theory of Radiation*. Oxford University Press, London, 3rd edition, 1954.

[HHH+06] Hill, G. C.; Hodges, J.; Hughey, B.; Karle, A.; Stamatikos, M.: Examining the Balance Between Optimising an Analysis for Best Limit Setting and Best Discovery Potential. In: L. Lyons & M. Karagöz Ünel, editor, *Statistical Problems in Particle Physics, Astrophysics and Cosmology*, pp. 108–+. 2006.

[Hil84] Hillas, A. M.: The Origin of Ultrahigh-Energy Cosmic Rays. In: *Ann. Rev. Astron. Astrophys.*, volume 22:pp. 425–444, 1984. doi:10.1146/annurev.aa.22.090184.002233.

[HL08] Huelsnitz, Warren; Lauer, Robert: IceCube Muon Filter for 2008 Pole Season. https://docushare.icecube.wisc.edu/dsweb/Get/Document-45305/2008_TFT_IceCube_MuonFilter.pdf, February 2008. Retrieved 2011-07-12.

[HM84] Halzen, F.; Martin, A. D.: *Quarks and Leptones: An Introductory Course in Modern Particle Physics*. J. Wiley & Sons, January 1984.

[HMWY10] Hümmer, S.; Maltoni, M.; Winter, W.; Yaguna, C.: Energy dependent neutrino flavor ratios from cosmic accelerators on the Hillas plot. In: *Astroparticle Physics*, volume 34:pp. 205–224, November 2010. doi:10.1016/j.astropartphys.2010.07.003. 1007.0006.

[Hör03] Hörandel, J. R.: On the knee in the energy spectrum of cosmic rays. In: *Astroparticle Physics*, volume 19:pp. 193–220, May 2003. doi:10.1016/S0927-6505(02)00198-6. arXiv:astro-ph/0210453.

[HP09] Heck, D.; Pierog, T.: Extensive Air Shower Simulation with CORSIKA: A User's Guide. http://www-ik.fzk.de/corsika/usersguide/usersguide.pdf, April 3 2009. Version 6.9xx.

[HR03] Hill, G. C.; Rawlins, K.: Unbiased cut selection for optimal upper limits in neutrino detectors: the model rejection potential technique. In: *Astroparticle Physics*, volume 19:pp. 393–402, June 2003. doi:10.1016/S0927-6505(02)00240-2. arXiv:astro-ph/0209350.

[HRR03] Haungs, A.; Rebel, H.; Roth, M.: Energy spectrum and mass composition of high-energy cosmic rays. In: *Reports on Progress in Physics*, volume 66:pp. 1145–1206, July 2003. doi:10.1088/0034-4885/66/7/202.

[HSS+07] Hoecker, A.; Speckmayer, P.; Stelzer, J.; Therhaag, J.; von Toerne, E.; Voss, H.; Backes, M.; Carli, T.; Cohen, O.; Christov, A.; Dannheim, D.; Danielowski, K.; Henrot-Versille, S.; Jachowski, M.; Kraszewski, K.; Krasznahorkay, A., Jr.; Kruk, M.; Mahalalel, Y.; Ospanov, R.; Prudent, X.; Robert, A.; Schouten, D.; Tegenfeldt, F.; Voigt, A.; Voss, K.; Wolter, M.; Zemla, A.: TMVA - Toolkit for Multivariate Data Analysis. In: *ArXiv Physics e-prints*, March 2007. arXiv:physics/0703039.

[Hul11] Hultqvist, Klas: Differential flux limits. https://internal.icecube.wisc.edu/reports/data/icecube/2011/02/005/icecube_201102005_v1.pdf, February 2011. Retrieved 2011-07-12.

[IA+06] Icecube Collaboration; Achterberg, A.; et al.: First year performance of the IceCube neutrino telescope. In: *Astroparticle Physics*, volume 26:pp. 155–173, October 2006. doi:10.1016/j.astropartphys.2006.06.007. arXiv:astro-ph/0604450.

[IAA+11] IceCube Collaboration; Abbasi, R.; Abdou, Y.; Abu-Zayyad, T.; Adams, J.; Aguilar, J. A.; Ahlers, M.; Andeen, K.; Auffenberg, J.; Bai, X.; et al.: First search for atmospheric and extraterrestrial neutrino-induced cascades with the IceCube detector. In: *ArXiv e-prints*, jan 2011. 1101.1692.

[Ish08] Ishihara, Aya: Filter Proposal for EHE analysis with IC40. https://docushare.icecube.wisc.edu/dsweb/Get/Document-45328/2008_TFT_ehe_filter_40_v3.pdf, February 2008. Retrieved 2011-07-12.

[IY06] Ishihara, Aya; Yoshida, Shigeru: Note on neutrino-generator and JULIeT: Effective area and event rate using the event weighting technique. http://internal.icecube.wisc.edu/reports/data/icecube/2006/08/001/icecube_200608001_v1.pdf, July 2006. Ver. 1.5, retrieved 2011-07-12.

[Jac75] Jackson, J. D.: *Classical electrodynamics*. J. Wiley & Sons, 1975.

[Joh11] Johansson, Henrik: *Searching for an Ultra High-Energy Diffuse Flux of Extraterrestrial Neutrinos with IceCube 40*. Ph.D. thesis, Stockholm University, 2011.

[K+08] Klepser, S.; et al.: First Results from the IceTop Air Shower Array. In: *ArXiv e-prints*, November 2008. 0811.1671.

[KAT01] KATRIN collaboration: KATRIN: A next generation tritium beta decay experiment with sub-eV sensitivity for the electron neutrino mass. In: *ArXiv High Energy Physics - Experiment e-prints*, September 2001. arXiv:hep-ex/0109033.

[KH07] Kelley, John; Hill, Gary: Effective Livetime and their Applications. http://www.icecube.wisc.edu/~jkelley/simulation/livetimes.pdf, August 2007. Retrieved 2011-07-12.

[Kle99] Klein, S.: Suppression of bremsstrahlung and pair production due to environmental factors. In: *Reviews of Modern Physics*, volume 71:pp. 1501–1538, October 1999. doi:10.1103/RevModPhys.71.1501. arXiv:hep-ph/9802442.

[Kow02] Kowalski, Marek: On the Čerenkov light emission of hadronic and electromagnetic cascades. http://icecube.wisc.edu/internal/reports/amanda/data/20020803-track.pdf, August 2002. Retrieved 2011-07-12.

[Kow03] Kowalski, Marek P.: *Search for Neutrino-Induced Cascades with the AMANDA-II Detector*. Ph.D. thesis, Humboldt-Universität zu Berlin, 2003.

[KR05] Klein, J. R.; Roodman, A.: Blind Analysis in Nuclear and Particle Physics. In: *Annual Review of Nuclear and Particle Science*, volume 55:pp. 141–163, December 2005. doi:10.1146/annurev.nucl.55.090704.151521.

[L+00] Lai, H. L.; et al. (CTEQ): Global QCD analysis of parton structure of the nucleon: CTEQ5 parton distributions. In: *Eur. Phys. J.*, volume C12:pp. 375–392, 2000. doi:10.1007/s100529900196. hep-ph/9903282.

[L+07] Lundberg, J.; et al.: Light tracking through ice and water – Scattering and absorption in heterogeneous media with PHOTONICS. In: *Nuclear Instruments and Methods in Physics Research A*, volume 581:pp. 619–631, November 2007. doi:10.1016/j.nima.2007.07.143. arXiv:astro-ph/0702108.

[Lan] Landsman, Hagar: linefit module. doxygen: http://www.ifh.de/~kislat/www/icerec/docs/V03-03-01/doxygen/linefit/index.html. Retrieved 2011-07-12.

[LP53] Landau, L. D.; Pomeranchuk, I.: Electron cascade process at very high energies. In: *Dokl. Akad. Nauk. Ser. Fiz.*, volume 92:pp. 735–738, 1953.

[LT] Landsman, Hagar; Turcan, Dusan: DipoleFit module. doxygen: http://www.ifh.de/~kislat/www/icerec/docs/trunk/doxygen/dipolefit/index.html. Retrieved 2011-07-12.

[Mat05] Matthews, J.: A Heitler model of extensive air showers. In: *Astroparticle Physics*, volume 22:pp. 387–397, January 2005. doi:10.1016/j.astropartphys.2004.09.003.

[McC09] McCartin, Joseph: *Cascade Reconstruction Analysis with the IceCube Neutrino Detector*. Master's thesis, University of Canterbury, Jannuary 2009.

[MDV+] Montaruli, Teresa; Diaz-Velez, Juan Carlos; et al.: The NeutrinoFlux C++ class: a service for fluxes for weighting. http://www.icecube.wisc.edu/~tmontaruli/neutrinoflux/NeutrinoFlux_Teresa.html. Retrieved 2011-07-12.

[Mid08] Middell, Eike: *Reconstruction of Cascade-Like Events in IceCube*. Diplomarbeit, Humboldt-Universität zu Berlin, 2008.

[Mid11] Middell, Eike: *N. N.* Ph.D. thesis, Humboldt Universität zu Berlin, 2011. In preparation.

[MP09] Middell, Eike; Panknin, Sebastian: Request for the Cascade Online Filter. https://docushare.icecube.wisc.edu/dsweb/Get/Document-48361/2009_TFT_Proposal_Cascade_Filter.pdf, January 2009. Retrieved 2011-07-12.

[MPE+03] Mücke, A.; Protheroe, R. J.; Engel, R.; Rachen, J. P.; Stanev, T.: BL Lac objects in the synchrotron proton blazar model. In: *Astroparticle Physics*, volume 18:pp. 593–613, March 2003. doi:10.1016/S0927-6505(02)00185-8. arXiv:astro-ph/0206164.

[NN03] NN: IceTop Preliminary Design Document. https://docushare.icecube.wisc.edu/dsweb/Get/Document-20579/idd_7.pdf, July 2003. Retrieved 2011-07-12.

[Pan96] Pandel, Dirk: *Bestimmung von Wasser- und Detektorparametern und Rekonstruktion von Myonen bis 100 TeV mit dem Baikal-Neutrinoteleskop NT-72*. Diplomarbeit, Humboldt-Universit"at zu Berlin, 1996.

[Pan08] Panknin, Sebastian: Request for the Cascade Online Filter – 2008 TFT Proposal. https://docushare.icecube.wisc.edu/dsweb/Get/Document-45267/2008_TFT_Proposal_Cascade_Filter.pdf, February 2008.

[Par06] Particle Data Group: *Particle Physics Booklet*. Particle Data Group, Berkley, 2006.

[PBKZ09] Panknin, Sebastian; Bolmont, Julient; Kowalski, Marek; Zimmer, Stephan: Muon Production of Hadronic Particle Showers in Ice and Water. In: *Proceedings 31. ICRC*, 0395. 2009.

[PVCI09] Pagliaroli, G.; Vissani, F.; Costantini, M.L.; Ianni, A.: Improved analysis of SN1987A antineutrino events. In: *Astroparticle Physics*, volume 31(3):pp. 163 – 176, 2009. ISSN 0927-6505. doi:DOI:10.1016/j.astropartphys.2008.12.010. URL http://www.sciencedirect.com/science/article/pii/S0927650508001965.

[R+07] Rott, Carsten; et al.: GoodRun Decision. http://wiki.icecube.wisc.edu/index.php/GoodRun_Decision, September 2007. Retrieved 2011-07-12.

[R+09] Resconi, E.; et al.: Status and prospects of the IceCube neutrino telescope. In: *Nuclear Instruments and Methods in Physics Research A*, volume 602:pp. 7–13, April 2009. doi:10.1016/j.nima.2008.12.013.

[R+10] Rott, Carsten; et al.: Good Run List IC40 V6.4. http://www.icecube.wisc.edu/~carott/good_run_list_IC40/IC40_v6.4/good_run_list_IC40_prelim_v6.4.txt, 2010. Retrieved 2011-07-12.

[Raw] Rawlins, Katherine: More details on ContainmentSize variables. http://www.ifh.de/~kislat/www/icerec/docs/V03-03-01/doxygen/flat-ntuple/containmentdetails.html. Retrieved 2011-07-12.

[RF] Rawlins, Katherine; Federova, Olga: ContainmentSize: useful new cut parameters. http://salt.uaa.alaska.edu/kath/ContainmentSize/ContainmentSize.pdf. Retrieved 2011-07-12.

[RLC05] Rolke, W. A.; López, A. M.; Conrad, J.: Limits and confidence intervals in the presence of nuisance parameters. In: *Nuclear Instruments and Methods in Physics Research A*, volume 551:pp. 493–503, October 2005. doi:10.1016/j.nima.2005.05.068. arXiv:physics/0403059.

[RMW03] Razzaque, S.; Mészáros, P.; Waxman, E.: Neutrino tomography of gamma ray bursts and massive stellar collapses. In: *PhysRevD*, volume 68(8):pp. 083001–+, October 2003. doi:10.1103/PhysRevD.68.083001. arXiv:astro-ph/0303505.

[Rou07] Roucelle, Cécil: Documentation for the DOMcalibrator module. http://internal.icecube.wisc.edu/reports/data/icecube/2007/09/001/icecube_200709001_v1.pdf, September 2007. Retrieved 2011-07-12.

[Ruta] Rutledge, Doug: Core-Removal. http://www.ifh.de/~kislat/www/icerec/docs/V03-03-01/doxygen/core-removal/index.html. Retrieved 2011-07-12.

[Rutb] Rutledge, Doug: Project docs for fill-ratio. doxygen: http://www.ifh.de/~kislat/www/icerec/docs/trunk/doxygen/fill-ratio/index.html. Retrieved 2011-07-12.

[Rut09] Rutlege, Doug: Optimization of the Fill Ratio. http://www.phys.psu.edu/~rutledge/FillRatioStudy/main.html, 2009. Retrieved 2011-07-12.

[Rut10] Rutledge, Doug: *NN*. Ph.D. thesis, Penn State University, 2010. In preparation.

[Sed58] Sedov, L. I.: Examples of Gas Motion and Certain Hypotheses on the Mechanism of Stellar Outbursts. In: *Rev. Mod. Phys.*, volume 30(3):pp. 1077–1079, Jul 1958. doi:10.1103/RevModPhys.30.1077.

[Ste05] Stecker, F. W.: Note on high-energy neutrinos from active galactic nuclei cores. In: *PhysRevD*, volume 72(10):pp. 107301–+, November 2005. doi:10.1103/PhysRevD.72.107301. arXiv:astro-ph/0510537.

[Stöß10] Stößl, Achim: *Estimating the Performance of Cascade Reconstruction algorithms with artificial light sources in IceCube*. Diplomarbeit, Eberhard-Karls Universiät Tübingen, 2010.

[Stöß11] Stößl, Achim: private communication, Jannuary 2011.

[TDP+07] The Acorne Collaboration; Danaher, S.; Perkin, J.; Ralph, S.; Rhodes, C.; Thompson, L.; Sloan, T.; Waters, D.: Simulation of ultra high energy neutrino induced showers in ice and water. In: *Astroparticle Physics*, volume 28:pp. 366–379, November 2007. doi:10.1016/j.astropartphys.2007.08.001. 0704.1025.

[Tep09] Tepe, Andreas: *Hardware Integration of the AMANDA into the IceCube Neutrino Teleskope and Search for Supersymmetric Particles with the IceCube Neutrino Telescope*. Ph.D. thesis, Bergische Universität Wuppertal, July 2009.

[Tsa74] Tsai, Y.-S.: Pair production and bremsstrahlung of charged leptons. In: *Reviews of Modern Physics*, volume 46:pp. 815–851, October 1974. doi:10.1103/RevModPhys.46.815.

[V+07] Voigt, Bernhard; et al.: Cascade Simulation. http://wiki.icecube.wisc.edu/index.php/Cascade_Simulation, March 2007. Retrieved 2011-07-12.

[V+09a] Voge, Markus; et al.: Hard Local Coincidence. http://wiki.icecube.wisc.edu/index.php/HLC, October 2009. Retrieved 2011-07-12.

[V+09b] Voge, Markus; et al.: PPC. http://wiki.icecube.wisc.edu/index.php/PPC, October 2009. Retrieved 2011-07-12.

[Voi08] Voigt, Bernhard: *Sensitivity of the IceCube detector for ultra-high energy electron-neutrino events*. Ph.D. thesis, Humboldt-Universität, 2008.

[vS10] van Santen, Jakob: *Markov-Chain Monte-Carlo Reconstruction for cascade-like events in IceCube*. Diplomarbeit, Humboldt-Universität zu Berlin, January 2010.

[vSW10] van Santen, Jakob; Whitehorn, Nathan: Photospline: smooth, semi-analytic interpolation for Photonics tables. https://internal.icecube.wisc.edu/reports/details.php?type=report&id=icecube%2F201011001, November 2010.

[W+07a] Woschnagg, Kurt; et al.: Deployment order. http://wiki.icecube.wisc.edu/index.php/Deployment_order, February 2007. Retrieved 2011-07-12.

[W+07b] Woschnagg, Kurt; et al.: Dust logger. http://wiki.icecube.wisc.edu/index.php/Dust_logger, Jannuary 2007. Retrieved 2011-07-12.

[W+08] Woschnagg, Kurt; et al.: New ice model. http://wiki.icecube.wisc.edu/index.php/New_ice_model, May 2008. Retrieved 2011-07-12.

[W+10a] Waldenmaier, Tilo; et al.: Cosmic Ray Detection with IceTop/IceCube. In: *Proceedings of the ICATPP 2010*. Como, Italy, October 2010. In preparation.

[W+10b] Woschnagg, Kurt; et al.: Coordinate system. http://wiki.icecube.wisc.edu/index.php/Coordinate_system, January 2010. Retrieved 2011-07-12.

[WB99] Waxman, E.; Bahcall, J.: High energy neutrinos from astrophysical sources: An upper bound. In: *PRD*, volume 59(2):pp. 023002–+, January 1999. doi: 10.1103/PhysRevD.59.023002. arXiv:hep-ph/9807282.

[Wie95] Wiebusch, Christopher H. V.: *The Detection of Faint Light in Deep Underwater Neutrino Telescopes*. Ph.D. thesis, Technische Hochschule Aachen, 1995.

[Zim08] Zimmer, Stephan: *Berechnung des myonischen Beitrags hadronischer Kaskaden im Eis*. Bachelorarbeit, Humbold Universität zu Berlin, July 2008.

[ZK66] Zatsepin, G. T.; Kuz'min, V. A.: Upper Limit of the Spectrum of Cosmic Rays. In: *Soviet Journal of Experimental and Theoretical Physics Letters*, volume 4:pp. 78–+, August 1966.

List of Figures

List of Tables

Danksagung

Zunächst einmal möchte ich mich bei Herrn Prof. Dr. Marek Kowalski bedanken, der es mir ermöglicht hat, an diesem Thema zu arbeiten und mich über die ganze Zeit, zuletzt über große Distanzen hinweg, betreut hat. Auch möchte ich mich bei Herrn Prof. Dr. Hermann Kolanoski und Herrn Dr. Christian Spiering für alle erdenkliche Unterstützung, nicht zuletzt bei der Finanzierung bedanken. Bei den Gruppenleitern Frau Dr. Elisa Bernadini, Herrn Prof. Dr. Thomas Lose, Herrn Dr. Stefan Schlenstedt möchte ich mich dafür bedanken, dass ich durch Ihre Hilfe gut in die Gruppen aufgenommen worden bin und mich über die ganze Zeit hinweg sehr wohl gefühlt habe. Für zahlreiche Diskussionen und Anregungen möche ich mich bei Herrn Dr. Michael Walter und Dr. Rolf Nahnhauer bedanken.

Die Arbeit fand innerhalb der weltweiten IceCube-Kollaboration statt, von der ich immer bereitwillig Hilfe und Unterstützung bekam. Insbesondere möchte ich Frau Dr. Elisa Resconi, Herrn Dr. Spencer Klein und Herrn Dr. Kurt Woschnagg sowie Jonathan Eisch, Henrik Johansson, Joanna Kiryluk und Naoko Kurahashi für ihre Hilfe bei meiner Analyse danken. Für die viele technische Unterstützung möchte ich mich ausdrücklich bei den Mitarbeitern des Rechenzentrums des DESYs sowie bei Herrn Olf Epler und für sämtliche Hilfe bei organisatorischen Fragen bei Frau Veronika Fetting bedanken.

Dass die Arbeitsatmosphäre so gut war und dass sich schnell Lösungen für viele Probleme fanden, ist einer Vielzahl von Kollegen geschuldet, von denen ich viele inzwischen zu meinen Freunden zähle. So möchte ich den beiden Annas und den beiden Matthiasen, Andreas und Matthew für die schöne Zeit an der Humboldt-Universität und in Berlin danken. Eike und Robert F. möchte ich nicht nur für ihre teils magische Hilfe mit Computerproblemen sondern auch für manch leckeres Essen und viel Unterstützung danken. Ja, das ganze Kaskadenbüro mit Achim und Arne ist für mich zu einem engen Freundeskreis geworden. Dazu sind auch Jakob und Nathan zu zählen, auch wenn uns ein Ozean trennt. Auch bei Fabian möchte ich mich für manche technische Hilfe und gute Zeit bedanken. Durch ihn sah ich auch die Stadt aus einen völlig anderen Blickwinkel. Für manch nettes Gespräch, schönen Abend und leckeres Essen möchte ich mich noch bei Bernhard, Heike, Jens, Pepe, Robert L. und allen anderen bedanken. Noch ein zweites Mal Danke an Achim, Arne, Eike, Fabian, Gareth, Jakob, Jens, Nathan und Robert F. dafür, dass sie meine Arbeit Korrektur gelesen haben.

Schließlich möchte ich all meinen Freunden auch außerhalb der Arbeit dafür danken, dass sie nicht nur eine sehr schöne Zeit mit mir geteilt haben, sondern auch in mancher schweren Lage zu mir gehalten haben. Insbesondere meinen Eltern und Felix möchte ich für all ihre Unterstützung und Vertrauen danken.

Selbständigkeitserklärung

Ich erkläre, dass ich die vorliegende Arbeit selbständig und nur unter Verwendung der angegebenen Literatur und Hilfsmittel angefertigt habe.

Berlin, den 2011-07-15 Sebastian Panknin